Deanship of Graduate Studies
Al – Quds University

Ordering Phenomena in Magnetic Nanoparticle Assemblies

Asmaa Ismael Alhroob

M.Sc. Thesis

Jerusalem – Palestine

1437/2016

Ordering Phenomena in Magnetic Nanoparticle Assemblies

:Prepared By

Asmaa Ismael Alhroob

B.SC. physics science Al-Quds University- Palestine

Supervisors

Prof. Salman M. Salman
Physics Department, Al-Quds University, Palestine

Prof. Thomas Brückel
Director, Peter Grünberg Institute PGI-4 and Jülich Center for Neutron Science (JCNS-2), FZ Jülich Germany

A thesis submitted in partial fulfillment of requirement for the degree of Master of Science in Physics/Al-Quds University

1437/2016

Al – Quds University
Deanship of Graduate Studies
Department of Physics

Thesis Approval

Ordering Phenomena in Magnetic Nanoparticle Assemblies.

Asmaa I. Alhroob.

Registration No: 21280005.

Supervisors:
Prof. Salman M Salman, Physics Al-Quds University, Palestine.

Prof. Thomas Brückel , Peter Grünberg Institute PGI-4, and FZ Jülich Center for Neutron Science (JCNS), Germany.

Master thesis submitted and accepted: 3/1/2016, the name and signature of examining committee member are as follows:

1. Head of the committee: Prof. Salman M Salman Signature:

2. Internal Examiner: Prof. Musa Abu Teir Signature:

3. External Examiner: Prof. Mustafa Abu Safa Signature:

Jerusalem- Palestine

2016/1437

Dedication

I would like dedicate this thesis to my lovely family for their endless love, support and encouragement me. Furthermore, I lovingly dedicate this thesis to the closest person to my heart "my beloved fiancé ".

Declaration

I, Asmaa I. Alhroob, declare that this thesis **"Ordering phenomena in magnetic Nanoparticle assemblies"** and the present work - with the exception of guidance from the supervisor - have prepared independently without assistance and has been generated by me as the result of my own original research and that it has not been submitted earlier elsewhere and that I have all relevant information to the best knowledge and belief have made that they are true and that I have nothing concealed.

I confirm that this work was done under the supervision of Professor Salman M. Salman from the Physics Department, Alquds University, Palestine, and Prof Thomas Brückel Director, Peter Grünberg Institute PGI-4 and Jülich Center for Neutron Science(JCNS), Germany*

Sign

Asmaa I. Alhroob

Date: 3/1/2016

*****This project is the part of a collaborative effort under the SCP-1 of the framework collaboration between Jülich research Center, Germany, and Alquds University, Palestine, and coordinated by Professors Thomas Brückel Director , Peter Grünberg Institute PGI-4 and Jülich Center for Neutron Science (JCNS), and Salman M Salman from Physics and Director of Alquds Jülich Cooperation Program at Alquds University.

Acknowledgements

Primarily, I would like to thank **Allah**, for his blessings to finish my thesis.

I would like to thank my beloved **parents, my fiancé and my family** for their encouragement me and they supported me throughout my life. Special thanks and gratitude to the wise and kind Mr. **Muhammad Abd Qawi** for supporting me during studying year. In addition special thanks to Jessie Qumsiyeh and her husband Dr. Mazin Qumsiyeh for supporting me.

I would like to thank my advisor **Prof. Salman M. Salman** for his guidance during my university studies and providing the chance to conduct this experiment within the framework of Alquds Jülich Cooperation.

Thanks to **Prof. Thomas Brückel** for providing support and hospitality to conduct my thesis at the wonderful JCNS-2 institute in this interesting field. I have benefited profoundly from the knowledge of the group. Special gratitude to **Dr. Emmanuel Kentzinger** for his best mentoring. I deeply appreciate his patience, guidance, enthusiastic encouragement and useful critiques of this work throughout the whole development process.

Thanks to **Dr. Yinguo Xiao** for allowing me to work with him in the sapphire part, and **Alice Klapper** for familiarizing me with the subject of magnetic nanoparticles assemblies. I really appreciate her assistance concerning any arising problem. To **Jochen Friedrich** for training me to use the SEM. To **René Borowski** from PGI-7 for the cooperation that gave me access to the clean room.

In addition, I acknowledge the contributions the **DANSE** project under **NSF** award **DMR-0520547** that developed SasView software.

Special thanks go to my colleagues at JCNS-2 for their warm welcome and the comfortable working environment as well as their support throughout the whole period of my stay and for the informative scientific discussions.

Finally, thanks to **my friends** and **teachers** for providing support.

Asmaa I. Alhroob

Abstract

In the present work, we studied the assemblies and ordered phenomena of magnetic nanoparticle in two and three-dimensional structure. In particular, we have studied 20nm diameter spherical iron oxide nanoparticles (**Fe_3O_4**) in toluene. The particles were supplied by Ocean Nano Tech LLC.

Magnetic nanoparticles were transferred to the silicon wafers (patterned and non-patterned) using two different deposition methods: the first was using spin coating with variable spinning speeds; making monolayer multilayer coating. The second was drop-casting, by dropping the magnetic nanoparticles on the silicon wafers.

The nanoparticles ordering on silicon wafers was studied using the Scanning Electron Microscope (SEM) and Gallium Anode Low Angle X-ray Instrument (GALAXI), to determine the size and distribution of magnetic nanoparticles by using GIMP and SasView software.

Grazing-incidence small angle X-ray scattering using GALAXI measurement was used to study the ordered arrays of magnetic nanoparticles. There was no evidence of strong correlation between the order of magnetic nanoparticles and the silicon itched stripes.

In addition, we have built our own patterned sapphire substrate by the heating treatment. The ordering of iron nanoparticles assemblies on patterned sapphire substrate was studied by using the same technique that used in patterned silicon part. The results were not conclusive.

Contents **Page**

LIST OF SYMBOLS

Symbol	meaning	symbol	meaning
$<\mathbf{ri^2}>$	Mean square distance	K_i	wave vector of the incident beam
μ	Magnetic moment	$\mathcal{L}$	Angular quantum number/ the azimuthal radius
$\boldsymbol{\mu}_l$	Orbital magnetic moment	L	Angular momentum/sample length
$\boldsymbol{\mu}_B$	Bohr magneton	m	meter/mass
μ_s	Spin magnetic moment	m^3	meter cube
$\boldsymbol{\mu}_r$	Magnetic permeability	m_s	spin projection number
μ_0	Vacuum permeability	m_l	Magnetic quantum number
$\boldsymbol{\mu}_1, \boldsymbol{\mu}_2$	The dipole moments	m_e	Electron mass
$\boldsymbol{\mu}_{if}$	matrix element for the transition	M	Magnetization
$\boldsymbol{\mu}_{eff}$	effective mass	M_s	Saturation magnetization
A	Area / Unit area/ Ampere	n	Principle quantum number / Degeneracy number of magnetic ions or molecules
$\mathbf{A}^\circ$	Angstroms	N	Number of atoms per unit volume / Degree of polymerization or the number of "Kuhn monomers"
a	Lattice constant	P_N	Normal pressure
B	Magnetic field	P_T	Tangential pressure
b	Characteristic length of Kuhn Monomers	ΔP	Laplace pressure
C	Curie constant	$\vec{Q}$	The scattering vector
C_{vdw}	Van der Waals interaction	Q	Intensity
C_{ind}	Debye interaction	r	Radius / Distance /principle radii of curvature
C_{orient}	Keesom interaction	$\vec{r}_{1,2}$	Position
C_{disp}	London dispersion interaction	S	Spin
cm^3	Centimeter cube	T	Temperature/Tesla
D	Diameter	t	Time
D(E)	Density of state	T_B	Blocking temperature
$D(E_F)$	Density of state at the Fermi level	T_C	Curie temperature
D_{spm}	Critical diameter of super-Paramagnetism	T_f	Freezing temperature
D_{sd}	Critical diameter of a single domain	$T\mu$	Morin temperature
D_{ij}	Dzyaloshinskii-Moriya vector	T_N	Neel temperature
e	Electron charge	T_v	Verway temperature
emu	electromagnetic unit	U_{vdw}	Van der Waals potential
E	Free energy	v	Speed / Orbiting frequency of an electron
E_d	dipolar interaction energy	V	Particle volume

E_s	Single state energy	v_1,v_2	The ionization frequencies
E_T	Triplet state energy	α	Angle between the dipole moment μ_1, μ_2
F	Capillary force	α_1, α_2	Electronic polarizabilites of the molecules
f(Q)	The form factor	β	Angle between μ_1 and distance r
f(h)	free energy of Steric repulsion interaction	γ	Angle between μ_2 and distance r
g	Landé g-factor	Γ	Surface density
H	Magnetic field strength	γ_L	Surface tension of the liquid-vapor interface
h	Planck's constant/ The length of the chain	σ	Surface tension
$\hat{H}$	Hamiltonian	λ_F	Fermi wavelength
$\hbar$	Reduced Planck's constant	ε_0	Vacuum permittivity
H_z	Hertz	χ	Magnetic susceptibility / Spin part of wave function
H_c	Coercivity	χ_P	Pauli susceptibility
hv_1,hv_2	The first ionization potential of the molecules	χ_{AF}	Antiferromagnetic susceptibility
$\hat{H}_{SE}$	Super exchange interaction	χ_{Fi}	Ferrimagnetic susceptibility
$\hat{H}_{DM}$	Dzyaloshinsky-Moriya-exchange interaction	χ_{FM}	Ferromagnetic susceptibility
$\hat{H}_t$	Kinetic energy	χ_{para}	Paramagnetic susceptibility
$\hat{H}_u$	Coulomb-energy	ψ_a, ψ_b	wave function of the state a, b
h_0	equilibrium length	ψ_s	Singlet state
i	Current	ψ_T	Triplet state
J	Exchange integral/total moment/Joule unit/ Exchange coupling constant	Ψ	Overall wave function
J_{ij}	Exchange constant between the i_{th} and j_{th} spins	ω	Excluded volume parameter/frequencies
J_{SE}	Total exchange energy	$\|i>$	initial state
J_{RKKY}	Coupling of Dzyaloshinskii-Moriya exchange	$\|f>$	final state
K	Kelvin/ Uniaxial anisotropy constant	$\rho(E_F)$	Density of state at final energy
k_B	Boltzmann constant	φ_0	Angle
K_F	The radius of the Fermi sphere	$\Delta\Omega$	The solid angle subtended by the scatterrer at the detector positioned at a distance r
K_t	wave vector of the transmitted beam		

List of Acronyms

A.D	Anno Domini
AF	Antiferromagnetic
AFM	Atomic force microscope
Amps	Amperes'
B.C.	Before Christ
CCP	Cubic closest packed
DC	Drop Casting
DE	Double exchange
DE	Direct exchange
DM	Dzyaloshinsky-Moriya exchange
DSA	Directed Self-Assembly
DBC	Di-Block Copolymers
FC	Field cooled
Fi	Ferromagnetic
FM	Ferromagnetic
FRM II	Forschungs-Neutronenquelle Heinz Maier-Leibnitz
GMR	Giant magneto resistance
GISAS	Grazing-Incidence Small-Angle Scattering
GISAXS	Grazing-Incidence Small-Angle X-ray Scattering
GISANS	Grazing-Incidence Small-Angle Neutron Scattering
GALAXI	Gallium Anode Low-Angle X-ray diffractometer
HCP	Hexagonal close packed
IE	Indirect exchange
ICS	Institute of Complex System
ILL	Institute Laue-Langevin
JCNS	Jülich Center For Neutron Science
nm	nanometer
NP	Nanoparticle
PGI	Peter Grünberg Institute
PGI-TA	Peter Grünberg Institute-Technical services and Administration
RKKY	Rudermann-Kittle-Kasuya-Yoshida exchange
SE	Secondary electron/ Super exchange
SC	Spin coating
SCF	Self-Consistent Field
STM	Scanning Tunneling Microscope
SEM	Scanning Electron Microscope
SNS	Spallation Neutron Source
SAS	Small Angle Scattering
SAXS	Small Angle X-ray scattering
SANS	Small Angle Neutron Scattering
TEM	Transmission Electron Microscope
VdW	Van der Waals interaction
WF	Weak Ferromagnetic

List of Figures

sample. a-b) Close up Well-ordered sub monolayer with speed 30 rpm for 8s. c-d) Close-up sub monolayer with speed 50 rpm for 8s. e-f)Monolayer with speed 20 rpm for 20s.

Figure 4.9: SEM images of iron oxide nanoparticles diluted with toluene in a proportion of 1:10 and deposited on a silicon wafer by spin coating. The pictures were taken in the middle of the sample. a-b) Without plasma treatment. C-d) 5 min oxygen plasma treatment.

Figure 4.10: SEM images of iron oxide nanoparticles diluted with toluene in a proportion of 1:10 and deposited on a silicon wafer. The pictures were taken in the middle of the sample. a) drop casting (DC), b-c) Spin coating 30 rpm (SC-30), d) Spin coating 50 rpm (SC-50).

Figure 4.11: The distribution of the measured NP diameters for the four analyzed SEM image. a) drop casting (DC), b-c) Spin coating 30 rpm (SC-30), d) Spin coating 50 rpm (SC-50).

Figure 4.12: Spherical form factor used to fitting the SAXS data to calculate the size and size distribution of the nanoparticles.

Figure 4.13: Small-Angle X-ray scattering by iron oxide nanoparticles dispersions in toluene of different concentration. Intensities have been scaled for display refinements of spherical form factor are presented by black solid lines. The curves range is $0.04 \leq q \leq 0.2$.

Figure 4.14: Detector image measured on samples of different concentration. a) 1:3, b) 1:10, c) 1:30.

Figure 4.15:GISAXS patterns measured at different incident angles αi and constant ξ angle, which define the plane rotation of the sample for a pre-structured Si wafer without nanoparticles. $\delta = 0.05$. The period of the gratings is 300nm and depth is 100nm. The ring, which crosses the specular reflection and the primary beam, corresponds to the scattering from Si gratings.

Figure 4.16: (a, b, c, d)GISAXS pattern of a pre-structured Si wafer without nanoparticles, measured at constant incident angle $\alpha i = 0.2°$and different ξ angles. $\delta = 0.01$ Time of each exposure is500s. The period of the gratings is 300nm and depth is 100nm. The ring, which crosses the specular reflection and the primary beam, corresponds to the scattering from Si gratings.

Figure 4.17: GISAXS patterns measured at different incident angles and constant ξ angle, which define the plane rotation of the sample for an 20 nm iron oxide nanoparticles deposited on a non- pre-structured Si wafer. $\delta = 0.05$. The gratings period is 300 nm. Time of each exposure is 1030s.

Figure 4.18: (a, b, c, d)GISAXS patterns for an 20 nm iron oxide nanoparticles deposited on a pre-structured Si wafer ,measured at different incident angles and constant ξ angle which define the in-plane rotation of the sample. time of each exposure is 1030s. $\delta = 0.05$. The incoming beam parallel to the stripes.

Figure 4.19 : (a, b, c, d)GISAXS patterns for an 20 nm iron oxide nanoparticles deposited on a pre-structured Si wafer ,measured at different incident angles and constant $\xi = 90^{\circ}$ angle which define the in-plane rotation of the sample. time of each exposure is 206s. $\delta = 0.05$. The incoming beam perpendicular to the stripes.

Figure 4.20: (a, b, c, d)GISAXS pattern of an 20 nm iron oxide nanoparticles deposited on a pre-structured Si wafer, measured at constant incident angles $\alpha i = 0.3°$ and different ξ angles. $\delta = 0.05$. Time of each exposure is 1030s. The period of the gratings is 300nm and depth is 100nm. The ring, which crosses the specular reflection and the primary beam, corresponds to the scattering from Si gratings. The spots correspond to the ordering of nanoparticles.

Figure 4.21: The slice from the GISAXS pattern ($\alpha i = 0.2^{\circ}$). Position of peaks give Δq = 0.33 nm -1 which correspond to the period between stripes and the distance between the nanoparticles $L = 2\pi/\Delta q$ =19 nm.

Figure 4.22: a) Crystal structures and the planes of sapphire, b) SEM image of sapphire.

Figure 4.23: Surface reconstruction of sapphire upon annealing.

Figure 4.24: SEM image for Sapphire substrate after heat-treated. a-b) on 1500°C for 24 h. c-d) on 1400°C for 24 h. e-f)on 1300°C for 24h.

Figure 4.25: a-b) TEM image of iron nanoparticles, c-d) SEM image of iron nanoparticles.

Figure 4.26: SAXS by Fe nanoparticles.

Figure 4.27: SEM image of Fe nanoparticles on patterned sapphire substrate. a) Fe nanoparticles in Hexane pull out slow. b) Fe nanoparticles in Hexane spin coating 30rps 5s. c) Fe nanoparticles in Hexane 1:2 diluted spin coating 30rps 5s. d) Iron nanoparticles in Hexane diluted 1:3 spin coating 30rpm for 5s.

LIST OF TABLES

1. Chapter 1 Introduction

1.1 Motivation

The phenomenon of magnetism dates back to earlier than 600 B.C. **[Gale Group, 2000]**. It has smitten humanity for thousands of years, but the first scientific discussions have begun at the time of Miletus (625-544 B.C.) **[Fowler, 1997]**. It was most probably first observed by the ancient Greeks and the early Chinese civilization in a form of the mineral magnetite called Lodestone **[Gale Group, 2000]**. Despite its charming properties it took up to 100 A.D until the Chinese discovered a useful application for the material as compass and in 1269, Peter Peregrinas de Maricourt wrote the Epistola de magnete, providing initial knowledge of magnetism **[Coey, 2001]**. During the following centuries natural philosophers gave little sight to the interrogation of magnetism except for William Gilbert who published his well-known book "De Magnete" in 1600 and is therefore often referred to as the father of magnetism **[Gilbert, 1600]**. Then Hans Christian Oersted discovered the relationship between electricity and magnetism in 1820, which caused a scientific revolution and intensive research **[Coey, 2001]**.

A large number of implementations that have had a primary effect to daily life such as wireless communication at the speed of light or data storage result of this revolution. In the last decades, intense research related to magnetism progressed towards objects in the nanometer range, a new approach arose called nanotechnology **[Wu et al, 2008]**. Size and surface effects have been developed and studied leading to a new kind of magnetic materials and applications, e.g. magnetic nanoparticles, Ferro fluids and magnetic nanocomposites **[Mohallem et al, 2012]**. The giant magneto resistance (GMR) which was discovered in 1988 independently by Albert Fert and Peter Grünberg, and honored with the Nobel prize in physics to both in 2007, is one of the best examples for nanomaterials **[Binasch, 1989] [Becker, 2009]**.

However, the ideas of nanotechnology started by Richard Feynman in a talk titled " There's plenty of room at the bottom". It was used in the pre-modern era when

alternate size gold and silver particles created colors in the stained glass windows of medieval churches.

Nevertheless, to make things visible at the nanoscale, different microscopes were invented only 30 years ago, leading to intense research in this area such as scanning tunneling microscope (STM), atomic force microscope(AFM), scanning electron microscope (SEM) **[NANO, 2014]**.

The mixture of nanotechnology and magnetism is called Nanomagnetism. It is a vivid and highly interesting topic and it opens new effects, which appear only on the nanoscale. That is e.g. super-Paramagnetism, new types of magnetic domain walls and spin structures. In particular magnetic nanoparticles (NP) (i.e. 'nanoclusters', 'nanocrystals 'or 'fine particles') e.g. iron oxide is still of large interest, because they can serve as building blocks for example for data storage media that provides high data density, spintronic devices, photonic or biomedical applications. Nanomagnetism is becoming more and more important for industrial applications e.g. sensors and this tendency will increase in future **[Petracic, 2010]**.

Magnetic nanoparticles and their assemblies are sought in high-density storage of data, magnetic separations, drug delivery, and hyperthermia treatment, as well as in magnetic relation switches for sensing biological interactions between proteins, DNA, and viruses. When magnetic nanoparticles self-assemble, they tend to align their magnetic moment in the direction of the local magnetic fields due to neighboring particles or applied fields. This gives rise to a specific directionality of interaction, enabling magnetic nanoparticles to form micron-sized, one-dimensional chains/wires or rings **[Bishop, 2009]**.

1.2 Concept

The range of this work presented in this thesis is the self-assembly of commercially available 20 nm and 30 nm iron oxide nanoparticles on the one hand and the fabrication of ordered arrays of these magnetic nanoparticles on the other. In Chapter two we focus on the theoretical background, general information about Nano magnetism and self-assembly. Several magnetic interactions are given. In addition, the types and the properties of iron oxide are given. Chapter three introduces instruments, experimental setups, and their principles that are used to analyze the samples. The main chapter in this thesis is chapter four, which contains the

results and explanation. Finally in chapter five, summary, outlook and recommendations for future work are presented.

1.3 Place of research (Jülich Centre for Neutron Science Institute)

The experimental work presented in this thesis was done at the Forschungszentrum Jülich GmbH in Germany, in the department Jülich Center for Neutron science (JCNS Figure1.1).

Figure 1.1: The Jülich Center for Neutron science.

The Jülich Center for Neutron science institute (JCNS) was established in 2006 as a merger of the institute for scattering methods and the institute for Neutron scattering, which became part of the newly established institute of complex system (ICS).

The institute dedicates itself to fundamental research on correlated electron systems and Nano magnetism as well as soft matter and biophysics. Major topics of the JCNS research are neutron-scattering methods in the areas of soft condensed and biological matter; Nano magnetism and highly correlated electron systems; and the development and use of scattering techniques to understand the structural and magnetic order, fluctuations and excitations in magnetic systems and in highly correlated electron systems at the atomic level.

The Neutron science institute includes the divisions: neutron scattering (ICS-1 / JCNS-1), scattering methods (PGI-4 / JCNS-2), outstations (FRM II Garching, ILL Grenoble, and SNS

Oak Ridge), technical services and administration (PGI-TA). The work was performed at the scattering methods institute JCNS-2. The Jülich center for neutron science shares a common technical and administrative infrastructure with the Peter Grünberg Institute (PGI), and serves as the organizational framework for Forschungszentrum Jülich globally recognized development program for methods and instruments, and for its own research programs in the field of Key Technologies.

Chapter 2 Theoretical background

2.1 Iron oxides

Iron oxides are compounds composed of iron (Fe) together with oxygen (O) and hydrogen including oxides (OH), which are widespread in nature. The term iron oxides summarizes sixteen different arrangements including oxides, hydroxides and oxides-hydroxides as shown in Table 2.1, where the iron is in the trivalent state in most arrangements**[Cornell, Schwertmann, 2003]**. The iron oxides, which are relevant for this thesis, are described in detail below.

Table 2.1: Arrangements of iron oxide **[Cornell, Schwertmann, 2003]**.

Oxide-hydroxides and hydroxides	Oxides
Goethite α-FeOOH	Hematite α-Fe_2O_3
Lepidocrocite γ-FeOOH	Magnetite $Fe_3(Fe^{II}Fe_2^{III}O_4)$
Akaganeite ß-FeOOH	Maghemite γ-Fe_2O_3
Schwertmannite $Fe_{16}O_{16}(OH)y(SO_4)z \cdot nH_2O$	Wustite FeO
δ-FeOOH	β-Fe_2O_3
Feroxhyte δ'-FeOOH	ε-Fe_2O_3
High pressure FeOOH	
Ferrihydrite $Fe_5HO_8.4H_2O$	
Bernalite $Fe(OH)_3$	
$Fe(OH)_2$Green Rusts $Fex^{III}Fey^{II}(OH)3x + 2y = z(A^-)z : A^- = Cl^-$: ½ $SO4^{-2}$	

2.1.1. Hematite

Hematite (α-Fe_2O_3) is one of several iron oxides compounds and the oldest known iron oxide mineral. It is the most stable one of the iron phase and it is often the end member of transformations of other iron oxides. It is the most abundant mineral found in rocks and soils **[Cornell, Schwertmann, 2003]**. It can also be obtained by converting Maghemite to the hexagonal hematite (α-Fe_2O_3) with the loss of magnetic properties at temperatures higher than 773.15K **[Teixeira et al, 2012]**. The magnetic behavior of Hematite depends on the

temperature. At room temperature it is weakly ferromagnetic. Below Morin temperature T_M ~ 260K the anisotropy forces the spins to lie along the C- axis of the hexagonal axis and the system becomes a perfect antiferromagnetism (AF). Above Morin temperature, it displays a transition to a weak ferromagnet (WF) and Fe^{3+} ions are antiparallel to each other along the C-axis. In the antiferromagnetic state, the magnetic moments are oriented along the [111] axis.

At the Morin temperature there is a sudden flop to a new direction, parallel to the basal plane (111) with the spins slightly canted that yields a small net magnetization in this plane, due to antisymmetric Dzyaloshinsky-Moriya-exchange interaction **[Goya et al, 2005] [Mishra, 2012]**. Hematite is an insulator **[Mishra, 2012]**. Above the Neel temperature T_N = 956K it is a paramagnetic material **[Lu, Meng, 2010] [Gubin, 2009]**.

Hematite can be applied as a pigment, because it is abundant in water and can be used for jewelry for its mirror-like metallic luster after polishing **[Morrish, 1994]**. Its color is blood-red if finely divided and black or sparkling grey if coarsely crystalline **[Cornell, Schwert-mann, 2003]**. Hematite nanoparticles can be utilized as catalyst, magnetic recording media, gas sensors etc. **[Gubin, 2009]**. Hematite has a hexagonal close packed (HCP) unit cell with alternating layers of $Fe^{3+}$and O^{2-} along the [001] axis as shown in figure 2.1(b), a lattice constant a = 0.5034 nm and c = 1.375 nm **[Teixeira et al, 2012]**.

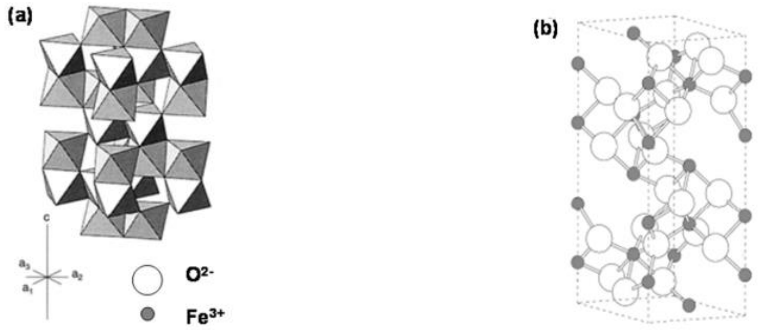

Figure 2.1: (a) HCP structure of hematite. (b) Model of the Unit cell. Images taken from [Cornell, Schwertmann, 2003].

2.1.2 Magnetite

Magnetite (Fe_3O_4) is a black, ferromagnetic mineral. Also known as loadstone **[Cornell, Schwertmann, 2003]** and the most magnetic one of all the naturally occurring minerals on earth **[Harrison, Borkowski, 2002]**. Its color is black or brownish-black with a metallic luster. It is found in rocks to control the magnetic properties of rocks and in living organism. Magnetite is a member of the spinel group and has an inverse spinel structure containing both $Fe^{2+}$and Fe^{3+} ions **[Cornell, Schwertmann, 2003]**. It has a unique important property that makes it interesting for environmental, technological and spintronics applications. Such as, it is a magnetic material, it contains Fe^{2+} in the structure, which is an important electron donor, low cost, low toxicity and relative good stability of the iron phases **[Teixeira et al, 2012]**. The unit cell as shown in figure 2.2 consists of $32O^{2-}$, $6Fe^{3+}$ and $8Fe^{2+}$ ions forming an inverse spinel structure as Maghemite structure.

A cubic closest packed CCP structure with a lattice constant (a = 0.839 nm) along the [111] direction contains the Oxygen ions while the divalent and half of the trivalent iron ions occupy octahedral sites. The other half of the trivalent iron ions are located on tetrahedral sites [Mishra, 2012]. The magnetic properties of magnetite depend on the synthesis process, particle size, and temperature [Friak et al, 2007]. The magnetic lattice of magnetite consists of two sub lattices. One, due to the Fe^{3+} ions at the tetrahedral sites. The other, the Fe^{3+} and Fe^{2+} ions at the octahedral sites. Below the Curie temperature (T_c) of 850K, the magnetic moments of the two sub lattices are oriented antiparallel to each other so the spins of Fe^{3+} ions cancel each other out. Only the spins of Fe^{2+} ions contribute to the total magnetic moments, and this leads to a ferromagnetic behavior. At Verway temperature T_v = 120K the magnetite undergoes a phase transition due to charge ordering mechanism and exhibits semimetallic properties above T_v while it becomes insulating material below T_v **[Mishra, 2012]**.

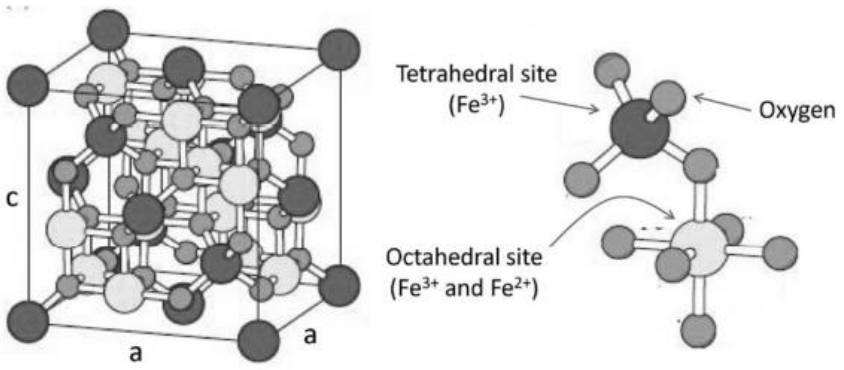

Figure 2.2: Crystalline structure of Magnetite: Grey spheres represent oxygen; black spheres tetra-hedrally coordinated iron and white spheres octa-hedrically coordinated iron-atoms. Image taken from [Teixeira et al, 2012].

2.1.3. Maghemite

Maghemite (γ-Fe_2O_3) is a ferromagnetic iron oxide and its color is reddish-brown **[Mishra, 2012]**. It can be formed by the topotactic oxidation of magnetite. It has isometric crystals **[Mindat, 2015]**. Its ferromagnetic ordering with high Neel temperature (~950K) together with its low cost and chemical stability lead to a wide application of Maghemite as a magnetic pigment in electronic recording media **[Dronskowski, 2001]**. Due to its biocompatibility and non-toxicity to humans in combination with a bandgap of around 2 eV, Maghemite nanoparticles can be used in biomedical applications **[Pankhurst et al, 2003]**.

Maghemite has an inverse spinel crystal structure consisting of 32 O^{2-} and 21 1/3 Fe^{3+} ions with a lattice constant of 0.834 nm. There are eight tetrahedral sites occupied by Fe^{3+} ions and sixteen octahedral sites only twelve sites are occupied by Fe^{3+}. The rest four sites consist of $2\frac{2}{3}$ vacancy and $1\frac{1}{3}$ Fe^{3+} ions as shown in figure 2.3. The magnetic structure consists of two sub-lattices. Due to the vacancies, they do not completely compensate each other leading to ferrimagnetic behavior. Above the Curie temperature T_c = 820K it becomes paramagnetic **[Mishra, 2012]**.

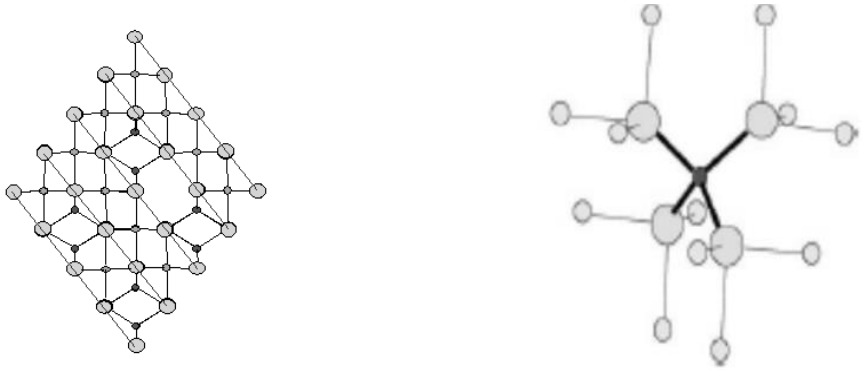

a) **b)**

Figure 2.3: Structure of Maghemite: Large spheres represent oxygen- and small spheres iron-atoms. a) Projection of the lattice in the xy-plane. b) unit cell of Maghemite. Images taken from [Cudennec, Lecerf, 2005].

2.1.4. Wustite

Wustite is a rare member of the iron oxides family and it is an iron-deficient mineral phase with the chemical formula Fe_xO **[McCammon, Liu, 1984]**, where x = 0.88-0.95 depending on temperature and pressure **[Yin et al, 2007] [Kugel et al, 1978]**. It is black antiferromagnetic material **[Mishra, 2012]**. Fe_xO is thermodynamically stable at temperature above 843K at atmospheric pressure. When cooled slowly below 843K it disproportionates to Fe_3O_4 and Fe **[Mishra, 2012]**. However, by quenching it to room temperature a metastable state of Fe_xO is obtained and the lattice parameter of the quenched phase varies linearly with x **[Yin et al, 2007]**. It consists of divalent Fe^{2+} ions and is mostly non-stoichiometric (oxygen deficient) **[Mishra, 2012]** and often found in rocks. It has a crystal structure like NaCl as shown in figure 2.4 with a lattice constant between 0.428 nm and 0.431 nm depending on the stoichiometry, magnetic structure, and composition **[Mishra, 2012]**.

Its magnetic properties depend on the temperature, and it is paramagnetic at room temperature. Below Neel temperature (T_N) of 198K the spins are arranged in the (111) plane of the lattice and the magnetic moments are parallel to [111] direction, while the magnetic moments in the adjacent layers are oriented to opposite directions giving rise to antiferromagnetic behavior**[Mishra, 2012]**. The conductivity of Fe_xO shows only a very small temperature dependence **[Tannhauser, 1961]**.

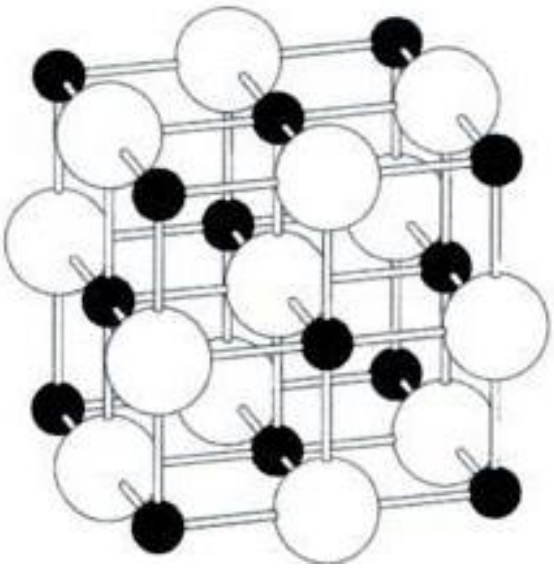

Figure 2.4: Structure of Wustite: Black spheres represent iron- and white spheres oxygen-atoms. Image taken from [Teixeira et al, 2012].

The crystalline structures and the properties of iron oxides discussed above are summarized in the following Table 2.2 together with additional information like saturation magnetization, magneto-restriction constant and anisotropy constant **[Cornell, Schwertmann, 2003] [Mishra, 2012]**. In this thesis, only Magnetite will be encountered.

Table 2.2: Summary of iron oxide properties.

Property	Hematite	Magnetite	Maghemite	Wustite
Crystal structure	HCP	Inverse spinel	Inverse spinel	NaCl
Saturation magnetization emu/cm³	2.5	480	380	-
Anisotropy constant [J/m3]	1.2×10^{6} (c-axis)	-1.35×10^{4}	-4.65×10^{3}	-
Magneto restriction constant	8×10^{-6}	35×10^{-6}	35×10^{-6}	-
Electric behavior	Insulator	$T < T_V$ insulator $T > T_V$ semi metallic T_V = 122 K	Insulator	Semiconductor
Color	Powder: Blooded Compact:Blue-black	Black	Red-brown	Black
Application	Pigment, jewelry, catalyst, gas sensor	Environmental application, Pigment	Magnetic recording, Medical application, Magnetic sensor	Precursor for iron oxide preparation
Lattice Constants[nm]	a = 0.5034 c = 1.375	0.839	0.834	0.428 to 0.431
Magnetic Behavior	$T < T_M$ (AF) $T_M < T < TN$ (WF) $T_N < T$ PARAM.	$T < T_C$ ferrimagnetic $T_C < T$ paramagnetic T_C = 858 K	$T < TC$ ferrimag. $T_C < T$ PARAM. T_C = 820 K	$T < T_N$ (AF) $T_N < T$ PARAM. T_N = 198 K

2.2 Magnetism

2.2.1 Sources of magnetism

All magnetic phenomena arise from forces between electric charges in motion. We have seen electric charges in motion as in current produce magnetic fields. This is one source of magnetism. Another source is the electron itself. Electrons behave as tiny magnets. Every electron in an atom behaves as a magnet in two ways, each having two magnetic dipole moments: Spin magnetic dipole moment, due to the rotation of an electron and orbital magnetic dipole moment, due to the revolution of an electron about the nucleus.

2.2.2 Quantum numbers and magnetization

Quantum numbers

We should start with the electrons to understand the magnetism phenomena in the solid state. Their energetic state and in which orbitals they can be found can be described using quantum numbers. The first quantum number called the principle quantum number (n) describes the size of the orbital, therefore indirectly describes the energy of an orbital:

$$n = 1, 2, 3, 4 \ldots \tag{2-1}$$

The electron energy depends principally on n. Angular quantum number is the second quantum number has the symbol ($\mathcal{L}$) to describe the shape of the orbital and it gives the absolute value of the angular moment $\mathcal{L}$.

$$\mathcal{L} = 0, 1, 2, 3, 4, 5 \ldots \quad (n-1) \tag{2-2}$$

$\mathcal{L}$ = s, p, d, f, g, h …

The magnetic quantum number (m_L) represents the spatial orientation.

$$m_{\mathcal{L}} = -\mathcal{L}, (-\mathcal{L}+1), (\mathcal{L}+2) \ldots 0 \ldots (\mathcal{L}-2), (\mathcal{L}-1), \mathcal{L} \tag{2-3}$$

Finally, each electron carries intrinsic properties in addition to its mass and charge called spin, this leads to spin angular moment S. Its projection along the quantization axis is described by the last quantum number called spin quantum number, which has the symbol m_s. It has only two possible values:

$$m_s = +1/2 \text{ or } -1/2 \tag{2-4}$$

The effect of the spin quantum number is that every orbital can hold up to two electrons with opposite spins (Pauli Exclusion Principle) **[Askeland et al, 2010]**.

Magnetization

An electron of mass m and charge -e moving with a velocity v in a circular Bohr orbit of radius r and area A, the current i,

$$i = \frac{e}{t} = \frac{e}{(\frac{2\pi r}{v})} = \frac{ev}{2\pi r} \tag{2-5}$$

from a magnetic point of view, the current loop looks like a dipole from a large distance. The magnetic dipolar moment of a loop of area $\overrightarrow{A}$ and current i is,

$$\vec{\mu} = i\vec{A} \text{ or in our case } \vec{\mu}_l = i\vec{A} \tag{2-6}$$

Where the quantity $\vec{\mu}$ specifies the strength of the magnetic dipole. The angular momentum of this electron is given by:

$$\vec{L} = mvr \tag{2-7}$$

$$\vec{\mu}_l = i\vec{A} = \frac{ev\pi r^2}{2\pi r} = \frac{evr}{2} = \frac{eL}{2m} = \frac{-\vec{g_l}\,\vec{\mu_B}\,\vec{L}}{\hbar} \tag{2-8}$$

Where,

$$\mu_B = \frac{e\hbar}{2me} = 0.927 \times 10^{-23} A.m^2 \quad \text{(Bohr magneton)} \tag{2-9}$$

and the g-factor for or electrons $g_e = 1$, for spins it has a value of $g_s \approx 2$. The eigenvalues for L^2 and L_z are $l\ (l+1)\hbar^2$ and $m_l\hbar$, respectively. The orbital magnetic dipole moment and the z-component are given by:

$$\vec{\mu}_l = \frac{-gl\mu_B\vec{L}}{\hbar} = \frac{-gl\mu_B\sqrt{l(l+1)}\hbar}{\hbar} = -gl\mu_B\sqrt{l(l+1)} \tag{2-10}$$

$$\vec{\mu}_l z = \frac{-gl\mu B\,\overrightarrow{Lz}}{\hbar} = \frac{-gl\mu_B\, ml\hbar}{\hbar} = -gl\mu_B ml \tag{2-11}$$

The electron has a spin magnetic moment μs due to spin angular momentum S. The eigen-values for S and S_{ze} are given by:

$$S = \sqrt{s(s+1)}\,\hbar \tag{2-12}$$

$$S_z = m_z\hbar \tag{2-13}$$

So,

$$\vec{\mu}s = \frac{-gs\mu_B S}{\hbar} \tag{2-14}$$

$$\vec{\mu}_{sz} = -gs\mu Bmz \tag{2-15}$$

Where gs is called the spin factor.

The total magnetic moment of an atom $\vec{J}$ arises from the LS-coupling or jj-coupling, depending on the atomic number.

$\vec{J}= \vec{L}+\vec{S}$ where $\vec{L} = \sum_i^N \vec{L}\iota$ $\vec{S} = \sum_i^N \vec{S}\iota$ (L - S coupling) (2-16)

$\vec{J} = \sum_i^N J\iota$ where $J = L\iota + S\iota$ (j-j coupling) (2-17)

If we apply an external field, the energy of a magnetic moment is:

$E = -\vec{\mu} . \vec{H}$ (2-18)

The magnetization of a solid material consisting of N atoms with a magnetic moment μ is defined as the magnetic moment per unit volume.

$$\vec{M} = \lim_{\Delta V \to 0} \frac{\sum \vec{\mu i}}{\Delta V} \quad (2\text{-}19)$$

With an applied external field $\vec{H}$ the magnetic induction $\vec{B}$ induced inside a material is:

$\vec{B} = \mu_0(\vec{H} + \vec{M})$ (2-20)

In free space $\vec{B} = \mu_0\vec{H}$ (2-21)

In a linear media $\vec{M} = \chi \vec{H}$ (2-22)

Where χ is the magnetic susceptibility. **[Mishra, 2012]**.

2.2.3. Types of magnetism

Depending on the degree to which a material can be magnetized in external magnetic fields, different types of magnetic solids materials can be distinguished by their magnetic susceptibility χ.

$\chi = \frac{M}{H}$ (2-22)

2.2.3.1. Diamagnetism

Diamagnetism is a very weak form of magnetism and may be masked by other, stronger forms like paramagnetic or ferromagnetic. In a diamagnetic material, the atoms have no net magnetic moment when there is no applied field. Under the influence of an applied field (H) the spinning electron precess and this motion, produces a magnetization (M) in the opposite direction to that of the applied field. Lenz' law is the analogous classical explanation of this property while diamagnetism is a purely quantum mechanical effect. All materials have a diamagnetic contribution, although it is so weak that it can only be observed in materials that do not exhibit other forms of magnetism. The diamagnetic susceptibility is small and negative ($\chi_{dia} < 0$) and the relative magnetic permeability μ_r is less than one ($\mu_r = (1+\chi_{dia}) < 1$).

Using perturbation theory the diamagnetic susceptibility is given by **[Blundell, 2007]**:

$$\chi_{dia} = \frac{-Ne^2\mu_0}{6Vm_e} \sum_{i=1}^{z} < r_i^2 > \qquad (2\text{-}23)$$

Where, N is the number of atoms or molecules per unit volume, e the electron charge, μ_0 the vacuum permeability, $< r_i^2 >$ the mean square distance, and m_e the electron mass.

The diamagnetic susceptibility does not depend on temperature. It is important for determining the size of atoms and molecules in chemistry **[Mishra, 2012]**.

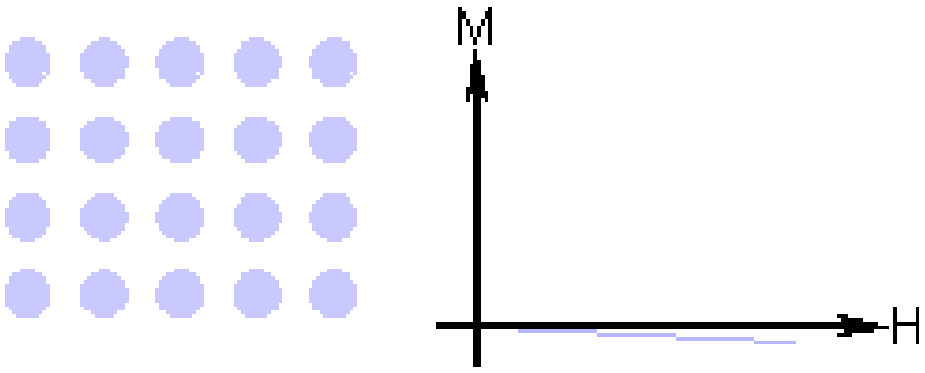

Figure 2.5: Magnetic behavior of Diamagnetism : Atoms have no magnetic moment.

2.2.3.2 Paramagnetism

In Paramagnetism atoms and molecules, the magnetic moments are randomly oriented in the absence of external magnetic field. If an field is applied, the magnetic moments align parallel to the field and the magnetization increases. This effect is opposed by thermal fluctuations

that increase the disorder. The susceptibility is positive but small (χ_{para}= 10^{-3}-10^{-6} > 0) and the relative magnetic permeability μ_r is greater than unity (μ_r = (1+χ_{para})> 1). Paramagnetism occurs in all materials with unpaired electrons and in metals because of the magnetic moments associated with the spins of the conducting electrons. Paramagnetic materials exhibit magnetization according to Curie's law:

$$M = \frac{C.B}{T} \qquad \textbf{[Dunlop, Özdemir, 1997]} \qquad (2\text{-}24)$$

Where, M is the resulting magnetization (magnetic dipole moment/unit volume), measured in A/m. B is the magnetic flux density of the applied field, measured in Tesla; T absolute temperature in Kelvins. C is Curie constant. $\left(C = \frac{\mu 0.\mu_B^2}{3K_B} Ng^2J(J+1)\right)$ **[Kittel, 1991]**. The susceptibility is given by:

$$\chi_{Para} = \frac{M}{H} \approx \frac{\mu 0\, M}{B} = \frac{n\mu 0 \mu_{eff}^{\ 2}}{3K_BT} \qquad (2\text{-}25)$$

$$\mu_{eff}^{\ 2} = gj\, \mu_B \sqrt{J\,(J+1)}$$

where n is the number of magnetic atoms (or molecules), g is the Landé factor, μ_B ($9.27400915\, e^{-24}$ J/T or A·m²) is the Bohr magneton, J is the angular momentum quantum number and K_B is Boltzmann's constant **[Mishra, 2012]**.

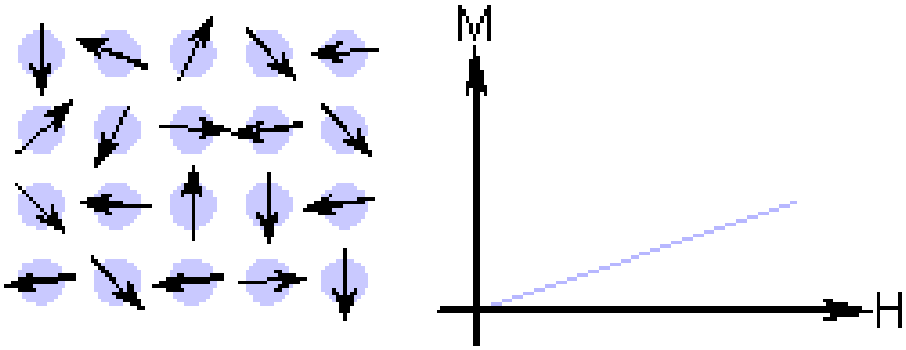

Figure 2.6: Paramagnetism: Atoms have randomly oriented magnetic moments.

2.2.3.3 Ferromagnetism

Ferromagnetic materials show a spontaneous magnetization in the absence of a magnetic field, and it is one of the strongest forms of magnetism. It is responsible for most of the mag-

netic behavior encountered in everyday life and is the basis for all permanent magnets. Ferromagnetism is only possible when atoms are arranged in a lattice and the magnetic moments can interact to align themselves parallel to each other. The magnetic moments for ferromagnetic materials have a tendency to orient parallel to each other to maintain a lowered-energy state even in the absence of an applied field. Ferromagnetic susceptibility is large and positive and described by Curie-Weiss law.

$$\chi_{FM} \propto \frac{C}{T-Tc} \qquad \text{(Curie- Weiß' law)} \qquad (2\text{-}26)$$

Above the curie temperature, T_c the material becomes paramagnetic due to thermal fluctuations. For $T>T_c$ the ferromagnetic susceptibility is described by Curie- Weiß' law:

$$\chi_{FM} = \frac{C}{T-Tc} >> 0 \qquad (2\text{-}27)$$

Where C is the material specific Curie constant.

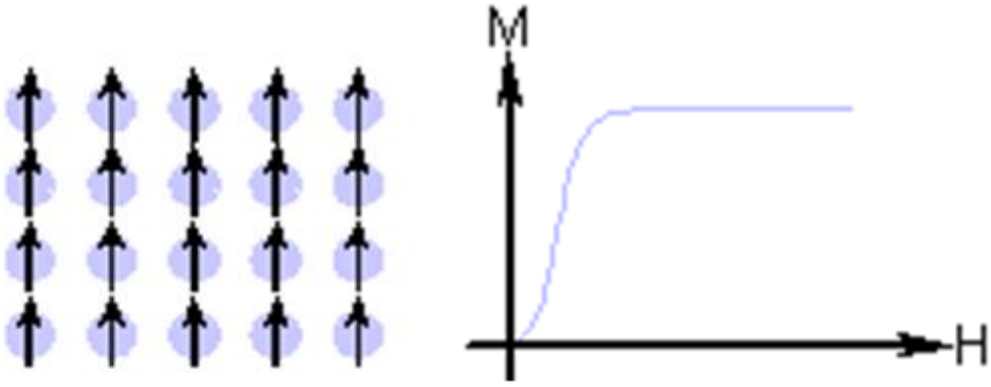

Figure 2.7: Ferromagnetism : Atoms have parallel aligned magnetic moments. [Mishra, 2012] [Askeland et al, 2010] [Blundell, 2007].

2.2.3.4 Antiferromagnetism

The system is called anti-ferromagnetic, if there is anti-parallel alignment of the atomic magnetic moments to the next nearest neighbor due to the exchange interaction between neighboring atoms, which is negative. Antiferromagnetic materials are uncommon, and the only element exhibiting antiferromagnetism at room temperature is Chromium. The magnetic susceptibility, χ_{AF} of an antiferromagnetic material goes through a maximum as the temperature decreases and it is generally small and positive. It can be written as:

$$\chi_{AF} \propto \frac{1}{T+T_N} \qquad \textbf{[Mishra, 2012]} \qquad (2\text{-}28)$$

Antiferromagnetism phenomenon is considered as two interpenetrating sub-lattices as shown in figure 2.8, where the magnetic moments in one sub-lattice point up and in the other point down. The magnetizations of the two sub-lattices are equal and have opposite directions **[Mishra, 2012]**. Antiferromagnetic order may exist at sufficiently low temperature, and become disordered above a certain or transition temperature known as Neel temperature (T_N=310K). Above the Neel temperature, the material is typically paramagnetic and the susceptibility is described as follows :

$$\chi_{AF} = \frac{C}{T+T_N} \qquad (2\text{-}29)$$

Where C is the material specific Curie constant.

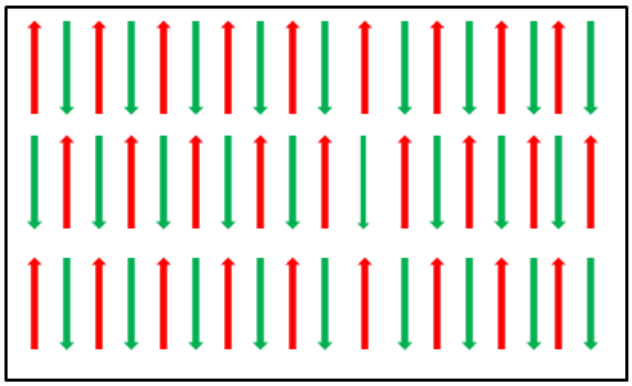

Figure 2.8: Antiferromagnetic order atoms have mixed parallel and anti-parallel aligned magnetic moments.: The red arrows represent spin up orientation and the green ones spin down.

When a magnetic field is applied below T_N it is important to know the direction of the applied field with respect to the sub lattice magnetization direction. If the field is applied parallel to the magnetization then the susceptibility is zero ($\chi \parallel$) at T=0. If it is applied perpendicular to the magnetization direction then the susceptibility is none zeros ($\chi \perp$). The variation of these two susceptibility with temperature is shown in figure 2.9 **[Mishra, 2012]**.

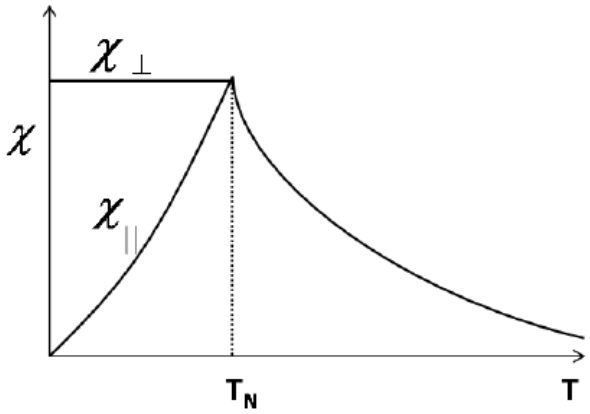

Figure 2.9: The temperature dependence of susceptibility for an antiferromagnetic . T_N the Neel temperature. $\chi \perp$ is the susceptibility normal to the external field, $\chi \parallel$ lies parallel to it. Image taken from [Mishra, 2012].

2.2.3.5 Ferrimagnetism

Ferrimagnetism is only observed in compounds, which have more complex crystal structures than pure elements. Ferrimagnetism materials have two sub-lattices of antiparallel magnetic moments that do not cancel each other out, and a net magnetization can be expected in this case **[Mishra, 2012]**.

a) b)

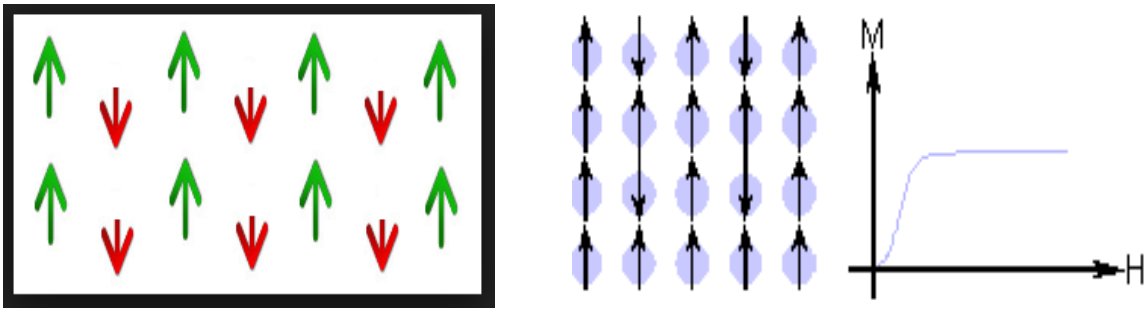

Figure 2.10: a) Ferrimagnetic order . b) magnetic behavior of Ferrimagnetic : Atoms have anti-parallel aligned magnetic moments.

Ferrimagnetism has a large and positive magnetic susceptibility. A famous example is magnetite which has a spinel structure, It contains negative oxygen ions O^{2-} and positive iron ions in two states occupying different lattice sites, iron (II) ions, Fe^{2+}, occupies octahedral sites only and iron (III) ions, Fe^{3+} occupies octahedral and tetrahedral sites. The oxygen ions are not magnetic, but both iron ions are. In magnetite crystals, for every oxygen ions, there are two iron(III) ions and one iron (II) ion. In addition, the spins of octahedral sites are anti-

parallel to those of tetrahedral sites and spins of the same coordination are parallel. The results are Fe^{3+} spins that cancel each other out and Fe^{2+} spins leading to a net moment.

2.2.3.6 Spin glass

By substituting a few magnetic atoms in a nonmagnetic material a collective freezing of the spins is found below certain temperatures known as freezing temperature T_f. This produces a spin glass system . Below T_f the magnetic moments are random but exhibit a collective spin state which is different from the high temperature state **[Blundell, 2007]**.

2.3 Nano-Magnetism

2.3.1 Origin of nanomagnetic behavior

Nano-magnetism has its origin in the fact that the magnetism of samples with nanoscopic sizes (~1 nm to 100 nm) or mesoscopic sizes (~100 nm to 1000 nm) present important differences compared to the magnetism of macroscopic samples. These differences could be described, in a simplified way, as arising from the fact that the magnetic systems of nanoscopic or mesoscopic scales present: (1) dimensions comparable to characteristic lengths, such as the size of magnetic domains, (2) broken translation symmetry, which results in sites with reduced coordination number, with broken exchange bonds and frustration. In addition, nanoscopic or mesoscopic objects exhibit a higher proportion of surface (or interface) atoms**[Guimarães, 2009]**.

The dynamic behaviors of magnetic objects of Nano-scale differ from the behavior of macroscopic samples of the same constituents, due to the enhanced importance of thermal fluctuations under the usual experimental conditions **[Guimarães, 2009].**

2.3.1.1 Sample dimensions and characteristic lengths

The simplest example of the effect of the characteristic lengths on the magnetic properties is the case of magnetic particles, as nanoparticles, that have dimensions smaller than the critical magnetic single-domain diameter. These particles therefore have the single domain as their lowest energy configuration **[Guimarães, 2009]**. Table 2.3 shows some characteristic lengths together with their typical values. Several parameters defining the magnetic properties such

as the spin diffusion length, the domain wall-width parameter and the exchange interaction length are also in the same order of magnitude as the particle size **[Guimarães, 2009]**.

Table 2.3: Some characteristic lengths in magnetism and their typical magnitudes **[Guimarães, 2009].**

Length	Typical magnitudes (nm)
Interatomic distance (Fe)	2.5×10^{-1}
Range of exchange interaction	$\sim10^{-1}$ ... ~1
Range of RKKY interaction	$\sim10^{-1}$ ... ~10
Domain size	10 ... 10^{4}
Superparamagnetic critical diameter	~1 ... $\sim10^{2}$
Critical single-domain size	~10 ... $\sim10^{3}$
Domain wall width	~1 ... $\sim10^{2}$
Exchange length	~1 ... $\sim10^{2}$
Spin diffusion length	~10 ... 10^{2}
Electron mean free path	~1 ... 10^{2}
Superconducting coherence length	~1 ... 10^{3}
Fermi wavelength/metal	$\sim10^{-1}$
Fermi wavelength/semiconductor	$\sim10^{2}$

2.3.1.2 Broken translation symmetry

The second aspect concerns the broken translation symmetry at interfaces. Three aspects of the problem of translational symmetry breaking are: (1) The relation of physical properties of the samples to their dimensionality, (2) The change in coordination of the atoms at the interface, (3) The effect of the increase in the proportion of surface atoms in a nanoscopic samples**[Ce et al, 2014]**.

The effects of the difference in dimensionality may be shown through the difference in density of state D(E).

There will be a quantum confinement for objects with dimensions comparable to the Fermi wavelength of the electron λ_F, so the wave character of the electrons will be dominant and their energies E will be quantized :

$$\mathbf{E}\ \text{object confined in 3D (quantum dot)} = \frac{\hbar^2\pi^2}{2m}\left(\frac{nx^2}{Lx^2}+\frac{ny^2}{Ly^2}+\frac{nz^2}{Lz^2}\right). \quad (2\text{-}30)$$

$$\mathbf{E}\ \text{object confined in 2D (quantum wire)} = \frac{\hbar^2\pi^2}{2m}\left(\frac{nx^2}{Lx^2}+\frac{ny^2}{Ly^2}+\frac{n^2}{L^2}\right) \quad (2\text{-}31)$$

$$\mathbf{E}\ \text{object confined in 1D (quantum film)} = \frac{\hbar^2\pi^2}{2m}\left(\frac{nx^2}{Lx^2} + 2\frac{n^2}{L^2}\right). \quad (2\text{-}32)$$

$$\mathbf{E}\ \text{object free electrons (macroscopic object} = \frac{\hbar^2\pi^2}{2m}\left(3\frac{n^2}{L^2}\right). \quad (2\text{-}33)$$

Where L is the length of the sample in x, y and z direction. Without index, L describes a macroscopic length. For the reason that many physical properties are closely related to the density of states D(E) that is dependent on the energy-like the Pauli susceptibility χ_p they change for nanomaterials.

$$\chi_p = \mu_\circ \mu B^2 D(EF) \quad (2\text{-}34)$$

Where $D(E_F)$ is the density of state at the Fermi level. In addition, the magnetic moments of the transition elements depend on the dimensionality of the sample. Another effect is the reduction of the number of nearest neighbors that result in narrower electronic bands and an increasing anisotropy energy as well as a higher orbital contribution to the magnetic moment.

The magnetic properties of atoms in interfaces are also affected by the presence of defects and impurities **[Guimarães, 2009].**

2.3.1.3 Nanoscopic samples and magnetization reversal

The last aspect concerns that the dynamic behavior of the magnetization of Nano magnets may also be very different from that of macroscopic objects. This arises due to thermal fluctuations that play a more important role in this case. For example, in nanoscopic magnetic particles as nanoparticles in the smaller range of diameters do not behave as stable magnets, exhibiting the phenomenon of super-Paramagnetism: in such particles the magnetization inverts spontaneously, since the thermal energy k_BT is comparable to their anisotropy energy.

A single-domain magnetic particle may spontaneously invert its magnetization, i.e., its direction may change from +z to −z, if its temperature T is above a certain blocking temperature T_B. This effect has important implications, since if the magnetization of such particle were to be used for information storage, at $T = T_B$ the information would be lost. Therefore, in magnetic storage, with the reduction in physical size of the recorded bit, its thermal stability becomes more and more an important issue.

The magnetic behavior of nanoparticles is, in general, strongly dependent on their dimensions and on the spin configuration. Magnetic nanoparticles present different spin arrangements according to their dimensions. For example, the smaller magnetically ordered particles will tend to be single-domain, and the larger ones, above the critical diameter c_{cr}, will be multi-domain, or else exhibit a vortex configuration **[Guimarães, 2009].**

2.3.2 Nanomagnetic effects

2.3.2.1 Single domain and super-para-magnetism

The subdivision of a material into distinct magnetic domains is the origin of many unique behaviors of magnetic materials. For example, differing magnetic directions of domains may give rise to the dissolution of the total magnetic moment, or an average magnetization approximating zero. Based on the theory of magnetism, taking an ellipsoid for example, the total energy is contributed by three types of energies, exchange, anisotropy, and magnetostatic energy. With the increase in the size of a magnet, the number of domains will also increase. As a result, there will be a decrease in the magnetostatic energy, while the more numerous domain walls will also raise the exchange and the anisotropy energies. Therefore, the size of the magnet has a great influence on its magnetic behavior, as can be illustrated by considering the coercivity of the magnet **[Guimarães, 2009] [Ce et al, 2014]**.

The size-dependent coercivity of magnetic is shown in the following figure 2.11. Firstly, for the particles whose diameters are smaller than the critical diameter of super-Paramagnetism (D_{spm}), the magnetic moment is not stable, and therefore Hc = 0. Secondly, the moment is stable, in the range between (D_{spm}) and the critical diameter of a single domain (D_{sd}), and the coercivity grows as diameter is increasing. Finally, for larger diameters, the multi-domain region appears, and the coercivity decreases with increasing particle diameter. Therefore, the sample has its maximum coercivity when its diameter is equal to single domain diameter **[Ce et al, 2014]**.

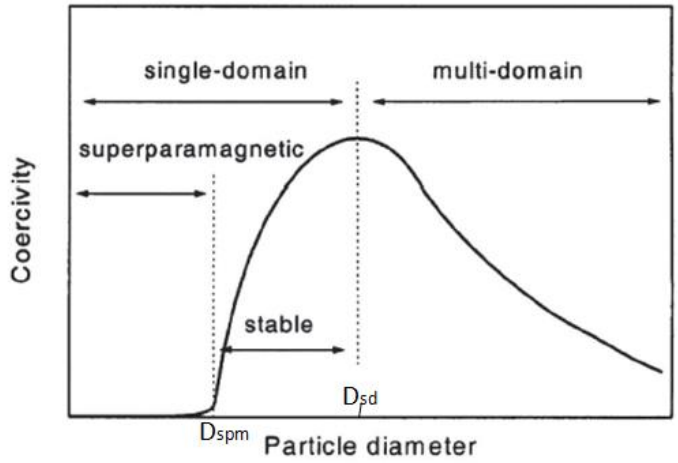

Figure 2.11: Size dependence of coercivity of magnets. Image taken from [Ce et al, 2014].

In the case for the single domain magnet, all the magnetic moments are along the anisotropy axis, and the free energy contribution from anisotropy and exchange is zero, so the magnetostatic energy is the only relevant energy term. Moreover, the single domain diameter of magnetic materials is proportional to the anisotropy constant K, saturation magnetization (M_S), and to the domain wall energy. In addition, the single domain diameter increases as the domain wall energy increases **[Goll, 2004]**.

The single domain diameter is proportional to the domain wall energy. In addition to that, with the increase of the domain wall energy, the critical single domain diameter (D_{sd}) will also increase. When the size of the particles is sufficiently small, the thermal energy will be able to overcome the anisotropy energy. Thus, the magnetization is no longer in a stable configuration. The temperature at which the thermal energy can overcome the anisotropy barrier of nanoparticles (NPs) is referred to as the blocking temperature (T_B) **[Yang et al, 2011]**. Below the maximum size called the critical diameter, at given temperature, the superparamagnetic behavior takes place **[Knobel, 2008] [Dormann, 1997]**.

2.3.2.2. Exchange-coupling effect

Kneller and Co-Workers have introduced the first model of the exchange- coupling effect, it takes place at the inter phase boundary between hard and soft magnets at the nanoscale **[Kneller, Hawig, 1991]**. In an exchange-coupled magnet, nanoscale hard and soft magnetic phases are coupled via the interfacial exchange interaction such that the soft phase becomes "hardened" and it's high magnetization enhances the energy product $(BH)_{max}$ of the compo-

site figure 2.12 **[Balamurugan et al, 2012]**. The energy arising from the exchange-coupled effect is given by :

$$E = -J \cdot \mu 1 \cdot \mu 2 \cos\theta \qquad (2\text{-}35)$$

where $\mu 1$ and $\mu 2$ are the magnetic moments of the two phases and $\cos\theta$ denotes the angle between them. Moreover, J represents the exchange-coupling constant, which describes the intensity of the magnetic coupling and is closely related to the arrangements of the magnetic moments.

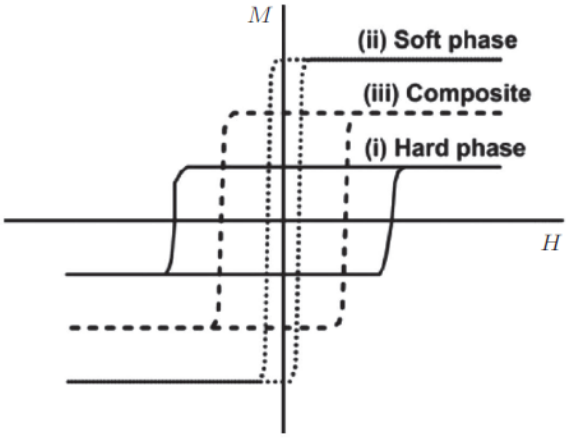

Figure 2.12: Typical hysteresis loops: (i) a hard phase, (ii) a soft phase,(iii) the exchange-coupled nanocomposites made of the soft and hard phases. Image taken from[Balamurugan et al, 2012].

The energy generated from exchange-coupling depends on the exchange coupling constant J, and the thickness of the phase **[Kim et al, 2000]**.

2.3.2.3 Exchange bias effect

The exchange bias phenomenon originates in the interaction between any two different domains of ferromagnetic (FM), antiferromagnetic (AFM), and ferromagnetic (FI) at the interfaces. This interaction acts as an effective field that changes the behavior of the ferromagnet under an applied magnetic field, and this interaction leads to the displacement of the hysteresis loop, this displacement of the hysteresis curve is proportional to the effectiveness of the coupling between the two layers **[Guimarães, 2009]**.

Also the shift in the hysteresis curve decreases with every measurement due to change in the antiferromagnetic domains with every rotation (so called trainings effect) i.e. the exchange bias field is found to depend on the number of measurements performed, decreasing as this number increases **[Nogues et al, 2000]**. The exchange bias effect was first discovered in the studies of field cooled (FC) oxidized Co particles **[Meiklejohn, Bean, 1956]**. The hysteresis loop of exchange bias magnets is shown schematically in Fig. 2.13 **[Nogues, Schuller, 1999]** Starting from magnetic saturation(a), as the field reverses, the FM moments begin to flip (b), but the AFM atoms exert a local restoring force due to the magnetic field from the interface.

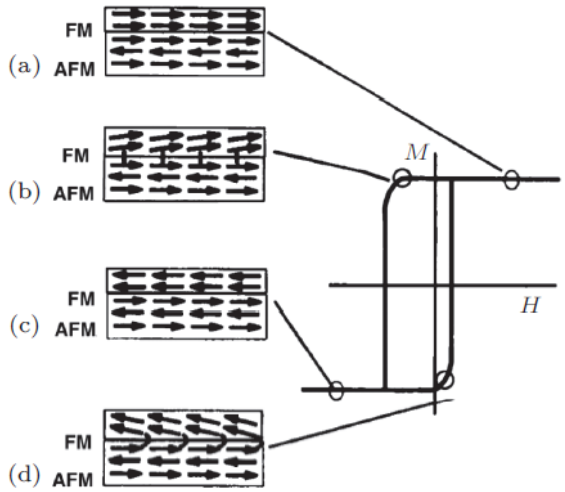

Figure 2.13: Schematic diagram of the spin configurations of an FM–AFM bilayer. a) The spins of the FM layer point in the energetically favored direction. b) Beginning of FM switching. c) In the saturation regime the spins of the FM layer are turned by 180°. d) a small positive field compared to b is necessary for reversal.. Image taken from [Nogues, Schuller, 1999].

An important characteristic of exchange bias magnets is known as coercivity-increase effect, which is the coercivity of the composite magnet increase, due to the requirement to overcome the antiferromagnetic anisotropy during the magnetization reversal in the ferromagnetic phase. The exchange bias field decreases with field cycling due to the reduction of effective pinning energy when the number of frozen spins along the cooling field direction decreases **[Zheng et al, 2004]**. When the Neel temperature is reached, the antiferromagnetic atoms at the interface align ferromagnetically to the ferromagnetic moments. The exchange bias blocking temperature is often at the Neel temperature or below **[Ce et al, 2014]**.

2.4 Magnetic Interactions

The interaction between magnetic moments leads to different long range ordering. These interaction energies will be discussed below.

2.4.1 Magnetic dipolar interaction

Magnetic dipolar interaction is also called magnetic dipole-dipole interaction. It refers to the direct interaction between two magnetic dipoles.

The strength of the dipolar interaction energy is proportional to several factors: (1) The magnitudes of the individual interacting dipoles, (2) The distance separating the interacting dipoles, (3) The degree of orientation of the magnetic moments, and (4) The "spectral overlap" of resonances that satisfy the conservation of angular momentum and energy.

The dipolar interaction energy between two magnetic dipoles, $\vec{\mu}_1$, $\vec{\mu}_2$ arbitrary oriented in space at a distance $\vec{r}$ between them (in Cgs system) is given by:

$$E_d = \frac{\vec{\mu}1.\vec{\mu}2}{r^3} - 3\frac{(\vec{\mu}1.\vec{r})(\vec{\mu}2.\vec{r})}{r^5} \quad (2\text{-}36)$$

Equation (2-36) can be re-written as:

$$E_d = \frac{\mu_1\mu_2}{r^3}(\cos\alpha - 3\cos\beta\cos\gamma) \quad (2\text{-}37)$$

Where μ_1 and μ_2 are absolute values of $\vec{\mu}1$ and $\vec{\mu}2$, α is the angle between $\vec{\mu}1$ and $\vec{\mu}2$, β is the angle between $\vec{\mu}1$ and $\vec{r}$, γ is the angle between $\vec{\mu}2$ and $\vec{r}$. To demonstrate the dependence of E_d on α, β, γ let us consider the interaction energy in several special cases, illustrated in figure 2.14. The interaction energy E_d for each case is given at the bottom of the figure.

The most stable orientation is reached when dipoles are parallel if they are "on top of each other" and when they are anti-parallel, if they are "side by side". In the case of parallel alignment, the interaction energy is repulsive, whereas it is attractive interaction in the case of anti-parallel alignment **[Mishra, 2012]**.

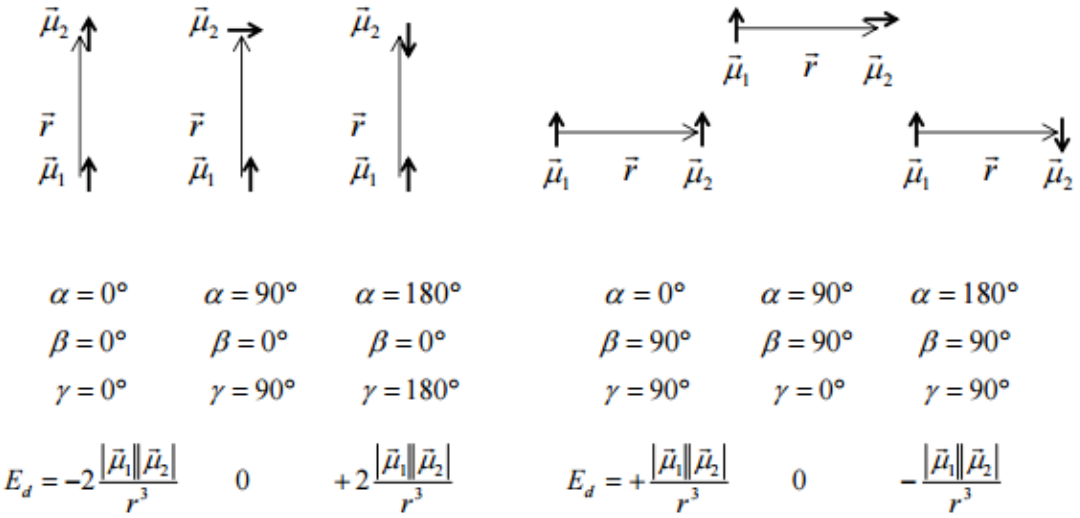

Figure 2.14: Energy E_d of dipole-dipole interaction of magnetic dipoles μ_1 and μ_2 at distance r for selected mutual orientations. Image taken from [Dipolar interaction, 2015].

Magnetic dipolar interaction can produce self-assembled structures, due to a directional orientation that it gives. It is also expected that the long range structural order will be affected by the dipolar coupling **[Mishra, 2012]**.

2.4.2 Exchange interaction

The exchange interaction is a purely quantum mechanical effect between identical particles that is based on the Coulomb interaction and Pauli exclusion Principle. It has no classical analogue. It is responsible for ferromagnetism and for the volume of matter. The two types of exchange interaction that are currently believed to exist are, a) direct exchange, b) indirect exchange, will be discussed below.

2.4.2.1 Origin

Consider two electron systems a, and b, the exchange integral can be derived. The total spin of those electrons is represented by

$$\hat{S} = \hat{S}^a + \hat{S}^b \qquad (2\text{-}38)$$

The combined wave function of the states can be written as $\psi a(\vec{r}_1)\ \psi b(\vec{r}_2)$, where $\psi a(\vec{r}_1)$and $\psi b(\vec{r}_2)$ are the wave function of individual electrons at position $\vec{r}_1$ and $\vec{r}_2$ respectively. The total wave function Ψ consisting of a spatial part Ψ and a spin part χ has to be antisymmetric (Pauli principle). Whatever, the exchange symmetry of the spin wave function, the spatial part must have the opposite symmetry.(i.e. if the spin part is antisymmetric singlet state χ_s,

then the spatial state would be symmetric. If the spin state symmetric triplet state χ_T, then the spatial state would be antisymmetric) **[Mishra, 2012]**.

Due to the electron can be characterized by Fermi-Dirac-statistics and follow the Pauli Exclusion principle, they are counted as Fermions **[Wilbs, 2013]**. The two electron wave function in singlet and triplet state can be written as **[Blundell, 2007]**.

$$\Psi_s = \frac{1}{\sqrt{2}}[\psi a(\vec{r}_1)\psi b(\vec{r}_2) + \psi a(\vec{r}_2)\psi b(\vec{r}_1)]\chi_s \quad (2\text{-}39)$$

$$\Psi_T = \frac{1}{\sqrt{2}}[\psi a(\vec{r}_1)\psi b(\vec{r}_2) - \psi a(\vec{r}_2)\psi b(\vec{r}_1)]\chi_T \quad (2\text{-}40)$$

[Blundell, 2007].

Where the index 'S' refers to the antisymmetric singlet state and the index 'T' refers to the symmetric triplet state. The eigenvalues of the singlet and triplet state are:

$$E_s = \int \psi_s^* \hat{H} \psi_s \, dr_1 dr_2 \quad (2\text{-}41)$$

$$E_T = \int \psi_T^* \hat{H} \psi_T \, dr_1 dr_2 \quad (2\text{-}42)$$

$$\text{Where, } \hat{H} = \frac{1}{4}(E_s + 3E_T) - (E_s - E_T)\vec{S}_1\vec{S}_2 \quad (2\text{-}43)$$

The spin part of the Hamiltonian is given by :

$$\hat{H}_{spin} = -2J\vec{S}1\vec{S}2 \quad (2\text{-}44)$$

The difference between the energies of the singlet and triplet state gives the exchange integral J. $E_S - E_T = 2\int \psi a^*(r1)\, \psi b^*(r2)\, \hat{H}\, \psi a(r2)\psi b(r1) dr1.\, dr2$

Thus, the exchange integral is defined as:

$$J = \frac{Es - ET}{2} = \int \psi a^*(r1)\, \psi b^*(r2)\, \hat{H}\, \psi a(r2)\psi b(r1) dr1.\, dr2 \quad (2\text{-}45)$$

If $J > 0$, $E_s > E_T$ and the triplet state is favored. If $J < 0$, $E_s < E_T$ and the singlet state is favored. The Hamiltonian for many electrons can be written as:

$$\hat{H} = \sum_{ij} Jij\, \vec{Si}\, \vec{Sj} \quad (2\text{-}46)$$

Where J_{ij} the exchange constant between the ith and Ith spins. If the two electrons belong to the same atom then the exchange interaction is positive and the triplet state is favored with antisymmetric spatial state. This minimizes the Coulomb energy by keeping them apart, which is consistent with the Hund's rule. If the two electrons belong to different atoms bonds are formed. This allows an electron to move around both nuclei what saves kinetic energy.

The molecular orbitals formed can be spatially symmetric(bonding) or spatial antisymmetric(antibonding) **[Mishra, 2012]**.

2.4.2.2 Direct exchange (DE)

Direct exchange operates between moments, which are close enough to have enough overlap of their wave functions. It gives short, strong range coupling which decreases rapidly as the ions are separated. Due to the magnetic orbitals are often localized in case of rare-earth materials, direct exchange interaction is quite rare **[Mishra, 2012]**.

A simple way to understand direct exchange is to look at two atoms with one electron in each. According to Bethe and Slater, the electrons spend most of their time in between neighboring atoms when the interatomic distance is small. This gives rise to antiparallel alignment and therefore negative exchange (Antiferromagnetic), figure 2.15.

Figure 2.15: Antiparallel alignment for small interatomic distances.

If the atoms are far apart, the electrons spend their time away from each other to minimize the electron-electron repulsion. This gives rise to parallel alignment or positive exchange (ferromagnetic), figure 2.16.

Figure 2.16: Parallel alignment for large interatomic distances.

For direct exchange, j can be positive or negative depending on the balance between Coulomb and kinetic energies.

2.4.2.3 Indirect exchange (IE)

Indirect exchange interaction couples moments over relatively large distances. It is the dominant exchange interaction in metals and magnetic materials. Usually ionic solid like MnO and MnF_2 **[Mishra, 2012]**. Where there is little or no direct overlap between neighboring electrons. In rare-earth metals, whose magnetic electrons in the 4f shell, direct exchange is rather small and indirect-exchange via the conduction electrons gives rise to magnetic order in these materials.

2.4.2.3.1 Super exchange (SE)

Super exchange describes the interaction between moments on ions too far apart to be connected by direct exchange, but coupled over a relatively long distance through a non-magnetic material. Super exchange would lead to an antiferromagnetic system. Super exchange acquired its name because of the relatively large distance, occupied by normally diamagnetic ions or molecules. Super exchange is a result of the electrons having come from the same donor atom being coupled with the receiving ions spins.

For super exchange the electron are occupying the lattice sites that have a single energy level. Super exchange can be described by the Hubbard-model **[Wilbs, 2013]**. The total Hamiltonian is given by:

$$\hat{H}_{SE} = \hat{H}t + \hat{H}_U \quad (2\text{-}47)$$

$$\hat{H}_t = -t\sum_{<ij>,\sigma}(Ci\sigma^{+}Cj\sigma^{-} + Cj\sigma^{+}Ci\sigma^{-}) \quad (2\text{-}48)$$

$$\hat{H}_U = -U\sum_i(ni\uparrow\uparrow ni\downarrow) \quad (2\text{-}49)$$

So, $\hat{H}_{SE} = \frac{t^2}{U}\sum_{<ij>}(\vec{\sigma i}\,\vec{\sigma j} - \sum_\sigma ni\sigma\, nj\sigma)$ **[Doniach, 1987]**.

Where $\hat{H}t$ characterizes the kinetic energy if an electron with spin σ on lattice site i moves to lattice site j by hopping. $\hat{H}_U$ represents the Coulomb-Energy U needed for two electrons occupying the same lattice site **[Wilbs, 2013]**. The total super exchange energy is:

$$J^{SE} \sim \frac{t^2}{U} \quad \textbf{[Goya et al, 2005]} \quad (5\text{-}50)$$

For U << t the system is metallic, for U >> t the Coulomb-part dominates with exactly one electron located on every lattice site.

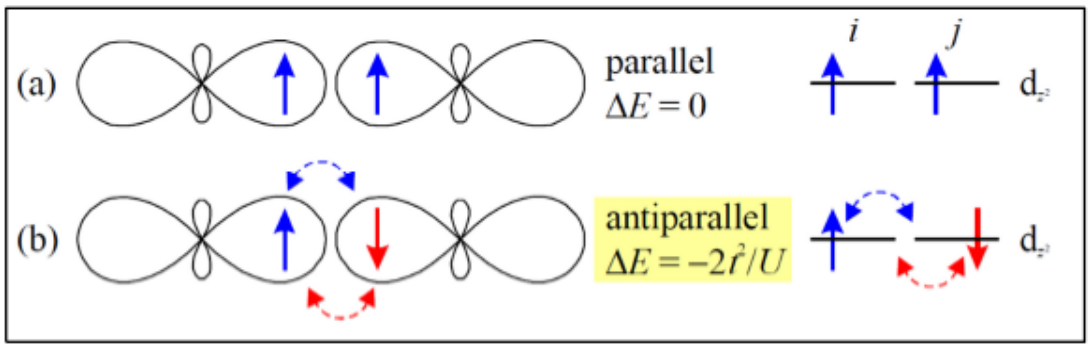

Figure 2.17: Single level super exchange: a) Parallel spins cannot hop due to Pauli Exclusion Principle so there is no energy gain Hence the spins arrange in an Antiferromagnetic order b) For antiparallel spins hopping is possible so the energy can be reduced due to delocalization. Image taken from [Opel, 2003].

2.4.2.3.2 Double exchange (DE)

Double exchange, the phenomenon where the magnetic ions are in mixed valence state then it is possible to have FM interaction amongst the ions **[Mishra, 2012]**. It offered a qualitative and descriptive understanding of the origin of ferromagnetism. It states that the conducting electrons will remember their spin orientations when wandering around. In transition metal oxides, those electrons come from the incomplete d-shell.

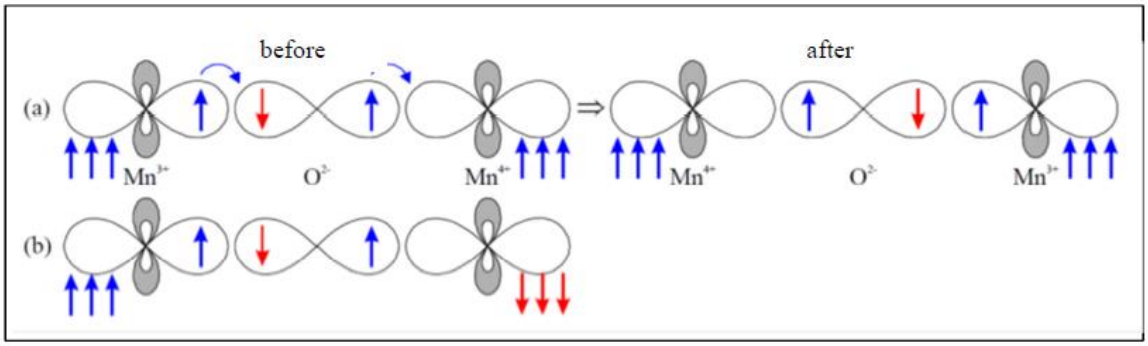

Figure 2.18: Double exchange: a) For parallel core spins double exchange is possible. b) For antiparallel core spins double exchange is not possible . Image taken from [Opel, 2003].

Suppose we have one Mn^{3+} and one Mn^{4+} bridged by an O^{2-} ion, the e_g electron on Mn^{3+} is contributing to the electric conductivity. The spin of this eg electron will first be parallel to the spins of core electrons on the t_{2g} orbitals. When this electron moves to the Mn^{4+} via the bridging O^{2-}, the total energy of the system would increase due to the Hund coupling if Mn^{4+} has a different spin orientation. Thus, high conductivity is expected when the neighboring Mn ions have their spins aligned in parallel. For parallel core spins the eg electron can travel across the diamagnetic oxygen ion to the Mn^{4+} ion without the need of excitation energy (Figure 2.18 a). For antiparallel spins, the electron is not able to move because of Hund's coupling energy, which has to be overcome (Figure 2.18 b) **[Wilbs, 2013]**.

2.4.2.3.3 Dzyaloshinsky-Moriya-exchange (DM)

Dzyaloshinsky-Moriya-exchange interaction(DM), also called anisotropic spin-spin interaction of symmetry is generally considered weak, as they depend on the spin-orbit couplings **[Gepas et al, 2002]**. The total magnetic exchange interaction between two neighboring magnetic spins Si and S_j can be written as:

$$\hat{H}_{DM} = D_{ij} . (Si \times Sj) \qquad (5\text{-}51)$$

Where, D_{ij} is the Dzyaloshinskii-Moriya vector. For an inversion symmetric crystal field referred to the center between the vector of the magnetic ions D is zero. Otherwise, D is parallel or perpendicular to the connection line of the ions. The interaction tries to arrange the spins right-angled to each other where the spins lie in a plane, which is perpendicular to D.

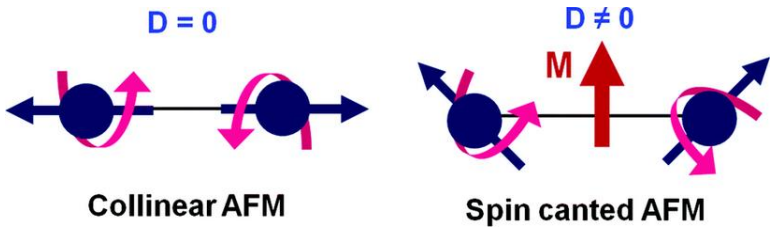

Figure 2.19: Dzyaloshinsky-Moriya-exchange (DM): For a crystal field that is not inversion symmetric the DM interaction tries to arrange the spins perpendicular to each other leading to a canted arrangement. Image taken from [Sakar, 2015].

This effect is often observed in antiferromagnetic and leads to a canted arrangement. Hence, a weak ferromagnetic moment, which is perpendicular to the spin axis of the antiferromagnet (Figure 2.19), can be observed **[Mishra, 2012] [Dzyaloshinsky, 1957] [Hu, 2012]**.

2.4.2.3.4 Rudermann-Kittle-Kasuya-Yoshida exchange (RKKY)

Rudermann-Kittle-Kasuya-Yoshida(RKKY) interaction, a kind of indirect exchange interaction. It is long range interaction. It is observed in metallic materials where the interaction between magnetic ions can be mediated by the conduction electrons. The conduction electrons can be polarized by the localized magnetic ion. The other localized magnetic ion coupled to the conduction electrons that polarized by the first localized magnetic ion. It is oscillatory in nature and the wave length of oscillation is $\frac{\pi}{KF}$. The coupling depends on the distance, it can be FM or AF, it is given by **[Mishra, 2012]**:

$$J_{RKKY}(r) \propto \frac{\cos(2KFr)}{r^3} \qquad (2\text{-}52)$$

Where, r is the distance and K_F is the radius of the Fermi sphere.

2.5 Self-Assembly

Self-assembly is the process of spontaneous arrangement, reversible transformation of the disordered building blocks (atoms, molecules, or nanoparticles) into an ordered array or regular structure. It is abundant in nature in all length scales (formation of weather system, galax-

ies, lipid bilayer and protein, etc.) **[Whitesides, Grzybousk, 2000] [Whitesides, Boncheva, 2002]**. Due to its flexibility and low costs, it is a very important techniques for the fabrication of Nano devices **[Mishra, 2012]**. Self-assembly provides a useful and general strategy for organizing simple nanostructures molecules or colloid particles (or other particles that are colloidal in size, such as viruses) into more ordered structures**[Whitesides, 2005]**. Self-assembly are caused by several interactions, which will be discussed below. It is one of the most interesting property of colloidal nanoparticles and was intensively studied over the last few years.

2.5.1 Van der Waals interaction (vdW)

Van der Waals force it is the most occurring interaction found everywhere in the nanoscale **[Mishra, 2012]**. It plays an important role in fields as diverse as supramolecular chemistry, structural biology, polymer science, nanotechnology, surface science, and condensed matter physics. Van der Waals forces include attractions and repulsions between atoms, molecules, and surface as well as other intermolecular forces, but they differ from other intermolecular forces that they are caused by correlations in the fluctuating polarization of nearby particles **[Abrikosov et al, 1963-1975]**. Van der Waals forces are driven by induced electrical interactions between two or more atoms or molecules that are very close to each other. vdW interaction is the weakest of attractions between molecules and can be written as:

$$U_{vdW}(r) = \frac{-C_{vdW}}{r^6} = -\frac{Cind+C_{orient}+Cdisp}{r^6} \quad (2\text{-}53)$$

Where r is the center to center distance between the atoms or molecules and-CvdW is a constant characterizing interaction species and the surrounding medium**[Israelachvili, 1994] [Bishop et al, 2009].** Its value depends on three parameters and can be separated into three processes **[Leite et al, 2012]**

1. dipole-dipole force, it is between a permanent dipole and a corresponding induced dipole (Debye force C_{ind}).
2. dipole-induced dipole force, it is between two permanent dipoles (Keesom force C_{orient}).
3. dispersion forces (charge fluctuation), between two instantaneously induced dipoles(London dispersion force C_{disp}).

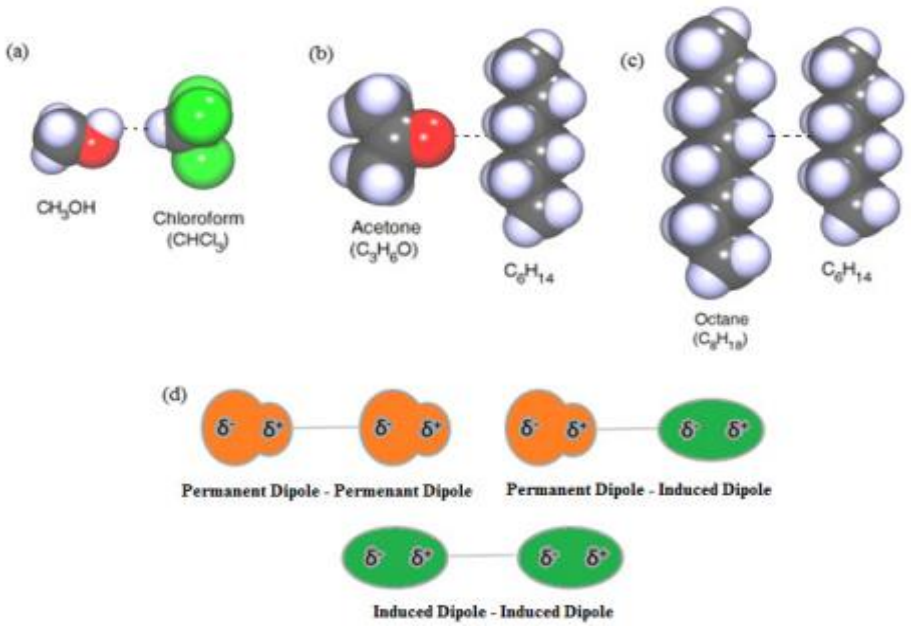

Figure 2.20: (a) Keesom forces. They exist only between polar molecules, (b) Debye force. It arises from the distortion of the charge cloud induced by a polar molecule nearby, (c) London forces, They result from electrostatic attraction between temporary dipoles and induced dipoles caused by movement of electrons; these are attraction forces that operate between all molecules and among isolated atoms in noble gases. (d) Interactions between molecules–temporary and permanent dipoles. Image taken from [Leite et al, 2012].

The first contribution is due to electrostatic interactions between charges dipoles, quadrupoles, and permanent multipoles. It is referred to as Keesom interactions. These force originates from the attraction between permanent dipoles and is temperature dependent. In addition, Keesom interaction is a very weak Van der Waals interaction.

The second contribution is the induction (also known as polarization) or Debye force, arising from interactions between rotating permanent dipoles and from the induced dipoles. These induced dipoles occur when one molecule with a permanent dipole repels another molecule's electrons. A molecule with permanent dipole can induce a dipole in a similar neighboring molecule and cause mutual attraction, as depicted in figure 2.20b. Debye forces cannot occur between atoms, also it is not a temperature dependent as Keesom interactions because the induced dipole is free to shift and rotate around the non-polar molecule **[Leite et al, 2012]**.

The third and dominant contribution is the dispersion or London force, it arises due to the non-zero instantaneous dipole moments of all atoms and molecules. Thus, London interactions are caused by random fluctuations in electron density in an electron cloud. The London

interaction is universal and is present in atom-atom interactions as well **[Leite et al, 2012]**. The constant C_{vdW} in equation 2-53 is given by

$$C_{vdW} = -\left[\frac{\mu 1^2 \mu 2^2}{3(4\pi\varepsilon 0\varepsilon)^2 KBT} + \frac{\mu 1^2 \alpha 2 + \mu 2^2}{(4\pi\varepsilon 0\varepsilon)^2}\right]_{V=0} + \left[\frac{3\alpha 2\alpha 1}{2(4\pi\varepsilon 0\varepsilon)^2}\frac{h\nu 1\nu 2}{\nu 1+\nu 2}\right]_{V>0} \quad (2\text{-}54)$$

$$U_{vdW}(r) = -\frac{1}{r^6}\left[\frac{\mu 1^2 \mu 2^2}{3(4\pi\varepsilon 0\varepsilon)^2 KBT} + \frac{\mu 1^2 \alpha 2 + \mu 2^2}{(4\pi\varepsilon 0\varepsilon)^2}\right]_{V=0} + -\frac{1}{r^6}\left[\frac{3\alpha 2\alpha 1}{2(4\pi\varepsilon 0\varepsilon)^2}\frac{h\nu 1\nu 2}{\nu 1+\nu 2}\right]_{V>0} \quad (2\text{-}55)$$

Where, α_1 and α_2 are the electronic polarizabilites of the molecules, μ_1 and μ_2 are the dipole moments, ε_0 is the vacuum permittivity ($8.854\times\ 10^{-12} c^2 J^{-1} m^{-1}$), K_B is the Boltzmann constant ($1.381\ \times\ 10^{-23} JK^{-1}$), T is the temperature, hv1 and hv2 are the first ionization potentials of the molecules (v1, v2 are ionization frequencies (Hz)) and h is the Planck constant ($6.626\ \times\ 10^{-34} Js$).

The first term (v=0) contains the Keesom and Debye energies, valid for interactions between polar molecules and named polar or entropic contribution **[Debye, 1921] [Keesom, 1921] [Keesom, 1920]**. The second term (v>0) is referred to as dispersion (London) contribution and acts between all molecules **[London, 1930]**.

2.5.2 Magnetic interactions

Controlling the self-assembly of nanoparticles requires the understanding of the relationship between the magnetic properties and other particle characteristics such as size or shape**[Bishop et al, 2009]**.

For magnetic nanoparticles smaller than critical size, single domain states are energetically favorable compared to multi domain state. In single particles, the spins can be summed up to one 'super spin' $\mu \sim 10^3 \mu_B$ **[Mishra, 2012]**.

One can assume that each nanoparticle behaves as a single magnetic dipole with dipole moment, $m = \mu_0 VM$, where μ_0 is the magnetic permeability, $V = \frac{4}{3}\pi r^3$ is the volume of the particle of radius a and M is the spatially homogeneous saturation magnetization. The dipole-dipole interaction energy is defined by

$$U_{dd\ stat} = \frac{\vec{m}1.\vec{m}2 - 3(\vec{m}1.\hat{r})(\vec{m}2.\hat{r})}{4\pi\mu 0 r^3} \quad (2\text{-}56)$$

Where $\hat{\mathbf{r}}=\frac{\vec{\mathbf{r}}}{\mathrm{r}}$, the unit vector along $\vec{\mathbf{r}}$. **[Bishop et al, 2009]**.

Due to the dipolar interaction, the directional and long range in nature nanoparticles tend to form chains or rings if it dominates **[Mishra, 2012]**.The magnetic dipole-dipole interactions were the sole forces responsible for particle assembly. In reality, magnetic interactions always compete with vdW force (and possibly with other types of forces) which become increasingly important with decreasing particle size**[Bishop et al, 2009]**.The magnetic moment or super spin in superparamagnetic nanoparticle fluctuate over time. This fluctuation will lead to a weaker dipolar interaction, hence the total dipole-dipole interaction is given by **[Israelachvili, 1994] [Bishop et al, 2009]**,

$$U_{dd} = U_{dd\ stat} + U_{dd\ SPM} \tag{2-57}$$

$$U_{dd\ SPM} = \frac{-1}{3KBT}\left(\frac{m1m2}{4\pi\mu 0 r^3}\right)^2$$

Where $U_{dd\ stat}$ is the static dipole-dipole interaction described in equation (2-36) above and in section 2.4.1 and $U_{dd\ SPM}$ is the dipole-dipole interaction due to thermal fluctuations.

2.5.3 Steric repulsion

Steric repulsion is one of entropic effects. The attractive forces between nanoparticles as vdW, dipolar, or surface forces, which leads to aggregate nanoparticles in solutions, is aiming the minimization of surface energy. This can be avoided by some kind of repulsive forces, like electrostatic repulsion or steric repulsion. Electrostatic repulsion force can be observed in aqueous or ionic solution by controlling the PH value. On the other hand, the steric repulsion is activated in organic solvents by coating the particles by some polymer, surfactant or ligand chains. One end of the polymer brushes surfactant or ligand chains is attached to the particle and the other end is left free. When this particle approaches another particle, the free ends of the polymer or ligand chains repel each other due to the steric effects . The polymer consists of monomers, which are usually arranged in random walk model to maximize the entropy and hence minimize the free energy. That means they try to become dense and short **[Mishra, 2012] [Bishop et al, 2009]**.

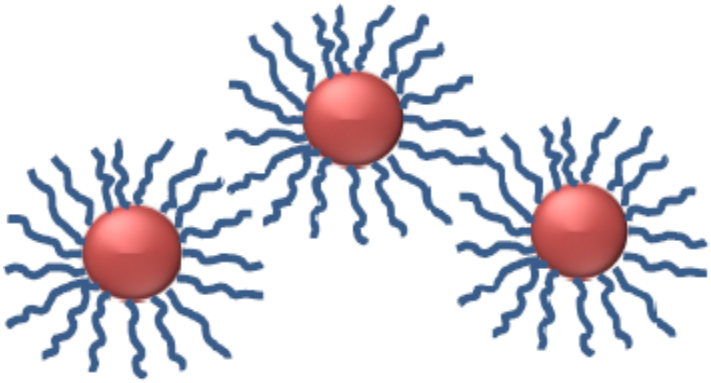

Figure 2.21: Steric repulsion: Polymers or ligand chains (blue) are attached on the surface of the particles (red) leading to a brush-like structure, which avoids agglomeration. Image taken from [Wilbs, 2013].

The theory of polymer brushes has been treated through various approaches including scaling theory, self-consistent field(SCF) theory, and Monte Carlo simulations **[Bishop et al, 2009]**. The free energy f (per unit area) is given as follows:

$$f(h) = \frac{\pi^2 KBT\Gamma h0^2}{6Nb^2}\left[\frac{1}{2}\left(\frac{h0}{h}\right) + \frac{1}{2}\left(\frac{h}{h0}\right)^2 - \frac{1}{10}\left(\frac{h}{h0}\right)^5\right] \quad (2\text{-}58)$$

The equilibrium length of the polymer brushes is given as:

$$h0 = N\left(\frac{12\Gamma b^2\omega}{\pi^2}\right)^{\frac{1}{3}} \quad (2\text{-}59)$$

Where, N is the degree of polymerization or equivalently the number of so called "Kuhn monomers" each with characteristic length b, ω the excluded volume parameter, which characterizes the strength of the repulsive interactions between chains, Γ is the surface density, h is the length of the chains and h_0 the equilibrium length. Equation(2-58) reveals that the free energy increases monotonically upon compression due to the increase in osmotic pressure within the brush. the nanoparticles get a surface like a brush (Figure 2.21) which avoids agglomeration **[Bishop et al, 2009]**.

2.5.4 Entropy

Entropy is a measure of the number of specific ways in which a thermodynamic system may be arranged. Even though it is regarded as the driving force of disorder, it can be responsible for nanoparticle assembly. It is a state function. The role of entropy, which can give rise to both attractive and repulsive interactions between components in dilute systems or provide a driving force for order in concentrated systems that provides a larger "free" volume to maximize the entropy.

2.5.5. Other forces

There are many other forces, short range, and long range order that play an important role in the ordering and assembling of nanoparticles. These forces will be explained briefly below.

2.5.5.1 Electrostatic forces

Electrostatic interaction arises between charged structures **[Mishra, 2012]**. It can be either attractive between like-charged particles or repulsive between oppositely charged particles. The electrostatic interaction is directional as in the case of particles with symmetric surface-distribution or permanent electric polarization. It is mostly observed in colloids or ionic particles. Furthermore , the length and the magnitude of these electrostatic interactions depend on several parameters: (1) The dielectric constant of the solvent, (2) The concentration and chemical nature. Electrostatic interactions are useful both for stabilizing particles in solution from agglomeration and for guiding their self-assembly into binary superstructures, due to its concentration, controllability through the solvents and chemical properties **[Bishop et al, 2009]**.

2.5.5.2 Capillary forces

The solvent between two adjacent particles exert a type of pressure on the two surfaces known as capillary force. It acts as an adhesive force. It has been used to form 1, 2-or, 3-dimensional nanoparticle assemblies **[Mishra, 2012]**. The capillary force is due to the pressure of cohesion and adhesion, which causes the liquid to work against gravity **[JRank, 2013]**. The total capillary force is:

$$F = 2\pi l\gamma L - \pi l^2 \Delta P \tag{2-60}$$

Where l is the azimuthal radius, γ_L is the surface tension of the liquid-vapor interface, and ΔP is the Laplace pressure given by:

$$\Delta P = \sigma\left(\frac{1}{r1} + \frac{1}{r2}\right) \tag{2-61}$$

Where, r_1 and r_2 refer to the principle radii of curvature and σ is the surface tension and can be calculated as:

$$\sigma = \int_{-\infty}^{+\infty} [P_N - P_T(z)]dz \tag{2-62}$$

P_N and P_T is the normal and tangential pressure, respectively. **[Butt, Kappl, 2010]**.

2.5.5.3 Convective force

Convective force or external convective force is a kind of force that affects the assemblies of nanoparticles. It is similar to external magnetic and electric fields. It also controls the assembly process in the bulk and at surfaces. They are aided by directional fluid flow patterns **[Mishra, 2012]**.

2.5.5.4 Friction or Lubrication forces

Friction is a resistance to sliding between two bodies in contact under a normal field. However, Lubrication is the process, or technique used to reduce wear of one or both surfaces in close contact, and moving relative to each other. Friction or Lubrication is related to the normal and convective force. In a highly concentrated solution, the particles experience friction between them or with the substrate **[Mishra, 2012]**.

2.5.5.5 Molecular surface forces

The term molecular surface forces include a variety of short-range attractive forces like covalent bonds, hydrogen bonding, dipolar interaction, ionic bond. These forces are used to build complex molecules, crystal and supramolecular architectures and for tuning the self-assembly of nanoparticles. The magnitude of these interactions is approximately equal to the number of individual bond multiplied by an effective bond-strength [60]. If a single bond is formed, the interaction strength, which affects the assembly process, is very small, while it is high in many bonds formation**[Mishra, 2012]**.

2.6 Directed Self-Assembly (DSA)

Directed Self-Assembly(DSA) is a bridge between two styles, top-down and bottom-up pattering. It refers to the integration of self-assembling materials with traditional manufacturing processes. The key concept of DSA is to take advantage of the self-assembling properties of materials to reach nanoscale dimensions and, at the same time, meet the constraints of manufacturing. In other words, DSA is an amazing technology and enables current manufacturing process capabilities to be enhanced and augmented, providing pathways for true Nano manufacturing at drastically reduced costs. The possible goals of DSA are: (1) Great long-range order in the self-assembled structure, and, (2) align structures to existing patterns on the substrate. DSA can be obtained by different approaches, which will be discussed below.

2.6.1 Approaches to DSA

2.6.1.1 Field-guided self-assembly

This approach to directed self-assembly helps to great long-range order, but not alignment. Various types of fields used to guide self-assembly as, electric and magnetic, flow gradients, temperature gradients(Zone annealing), mechanical shear stress.

2.6.1.2 Template-guided self-assembly

The second approach to DSA is Template-guided self-assembly, it can accomplish both DSA goals, which are reported before. Different templates used to guide DSA, Physical (topographical) template, Chemical template(Chemo epitaxy), Biological template(e.g. DNA).
The templates can be prepared by lithography and subsequent etching of the materials. The templates can also be prepared by self-assembly of di-block copolymers(DBC), nanoparticles or DNA **[Mishra, 2012]**.

2.7 Scattering methods applied to magnetic nanoparticles

Magnetic nanoparticles and assemblies can be investigated by various scattering techniques. The small-angle scattering method is advantageous for studying the nanoparticle's morphology, including size and size distribution, Also, small-angle scattering methods are used for studying particle interactions, ranging from disordered nanoparticle aggregates up to the crystalline order in nanoparticle mesocrystals, which results in a structure factor. The ordered assemblies of nanoparticles in two or three dimensions on a substrate were studied by grazing incidence geometry.

2.7.1 Small angle scattering(SAS)

Small angle scattering(SAS) is a powerful scattering technique based on divergence of collimated radiation far from the straight trajectory after it interacts with structures that are much larger than the wavelength of the radiation. Its name 'small angle' came due to its deflection angle is small(0.1-10°). SAS technique can give information about the shape, size and orientation of structures in a sample. SAS, also, used to investigate large-small structures from 10A° to thousands and even several ten thousands of Angstroms. The most important characteristic of the SAS technique is its potential to analyze the inner structure of disordered systems. SAS can refer to Small angle neutron scattering(SANS) and small angle X-ray scattering(SAXS). The small angle scattering technique relevant to this work is small angle X-ray scattering, it will be discussed below.

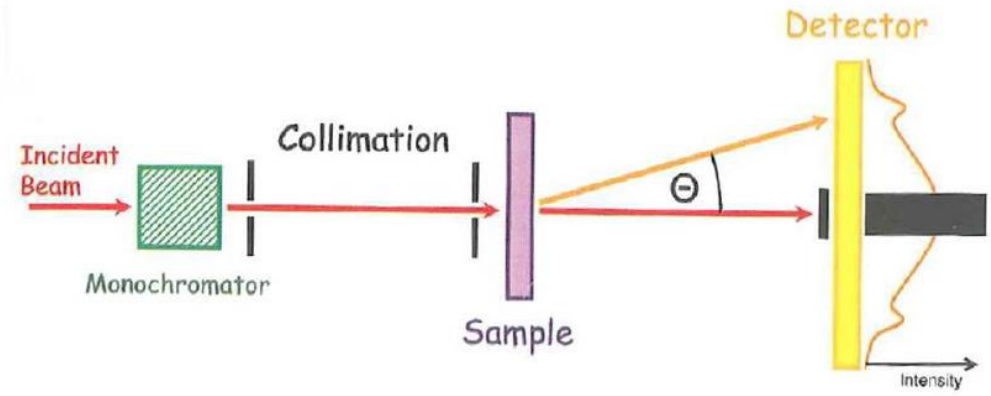

Figure 2.22: Schematic of a small-angle scattering instrument where the scattering of radiation to small angles by a sample. Image taken from [IFF Spring school, 2007].

2.7.1.1 Small angle X-ray scattering (SAXS)

Small angle X-ray scattering(SAXS) is an analytical method to determine the structure of particle system in terms of such parameters as average particle sizes, shapes, distribution, and surface to volume ratio. The materials can be solid, liquid or gaseous domains(so-called particles) of the same or another material in any combination. In addition, it is a fundamental method for structural analysis of condensed matter. SAXS is a universal technique applicable to a wide range of particle sizes, and therefore a major tool to rapidly and comprehensively characterize macromolecular and nanostructured systems. The elastic scattering of X-rays by a sample, is recorded at very low angles (typically 0.1-10°), and thereby capable of delivering structural information of macromolecules between 5 and 25 nm of repeat distances in partially ordered systems of up to 1500nm **[Glatter, Kratky, 1982]**.

The SAXS technique is accurate, non-destructive and usually requires a minimum of sample preparation. Application areas of this technique are very wide and include colloids of all types, metals, cement, oil, polymers, plastics, proteins, foods and pharmaceuticals and can be found in research as well as in quality control. In SAXS, X-rays produced by a source irradiate a sample. In most cases, the source IS an X-ray tube, and can be a synchrotron.

The main principles of SAXS were developed in the late 1930s by A. Guinier with his studies of metallic alloys. Already in the first monograph on SAXS by Guinier and Fournet (1955) it was demonstrated that the method yields not just information on the size and shapes of particles, but also the internal structure of disordered and partially ordered systems.

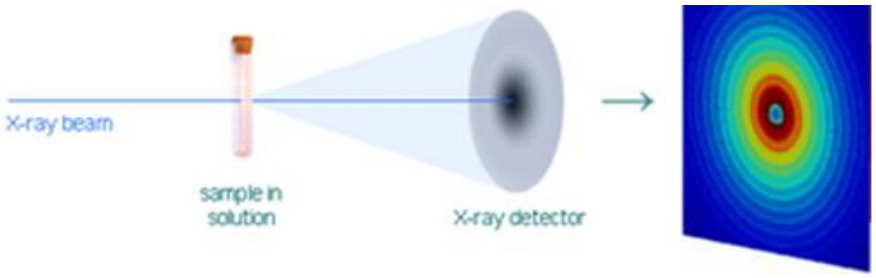

Figure 2.23: principle of Small angle X-ray scattering(SAXS) [Biosaxs, 2013].

In SAXS instrument a monochromatic beam of X-rays is transported to a sample and, some of the X-rays scatter, while most go through the sample without interacting with it. The X-rays that scatter form a two-dimensional scattering pattern, which contains information on the structure of the sample, then the scattered X-rays are detected at a detector, which is typically a 2-D flat X-ray detector located behind the sample perpendicular to the direction of the primary beam that initially hit the sample. A SAXS experiment is simple: a sample is illuminated by X-rays and the scattered radiation is registered by a detector, these scattered radiation form a scattered pattern as shown in figure 2.23.

2.7.1.2 Scattering cross section

When a beam strikes a target consisting of particles, some of photons pass directly through the target while others are deflected. The cross section, which is denoted σ, is a measure of the effectiveness of the interaction between beam and target, the larger the cross section, the more likely it is that the beam is deflected. A cross section depends on the type of target involved and usually depends on the energy of the beam. The cross section has the dimension of area or length^2. In general, the cross section is the effective area of the collision region.

Suppose there is a beam consisting of particles is scattered by a target has a potential $V(\vec{r})$ containing a particle and is detected by a detector situated at a distance $(\vec{r})$ from the target. The transition from the initial state $|i> (\overrightarrow{Ki}, Ei)$ to a final state $|f> (\overrightarrow{Kf}, Ef)$ is given by Fermi's golden rule as,

$$W = \frac{2\pi}{\hbar}|Mif|^2\rho(Ef) \tag{2-63}$$

Where $Mif = < f|H1|i >$ is the matrix element for the transition $\rho(Ef)$ is the density of states at energy Ef. The scattering cross section is given as,

$$\frac{d\sigma}{d\Omega} = \frac{W\Delta\Omega}{\Phi 0 \Delta\Omega} \tag{2-64}$$

Where ΔΩ is the solid angle subtended by the scatterer at the detector positioned at a distance $\vec{r}$. This is shown in figure 2.24. thus, the transition probability over the solid angle is written as,

$$W\Delta\Omega = \frac{2\pi}{\hbar}\int |Mif|^2 \ \rho(Ef)\delta(Ef - Ei)dEf \tag{2-65}$$

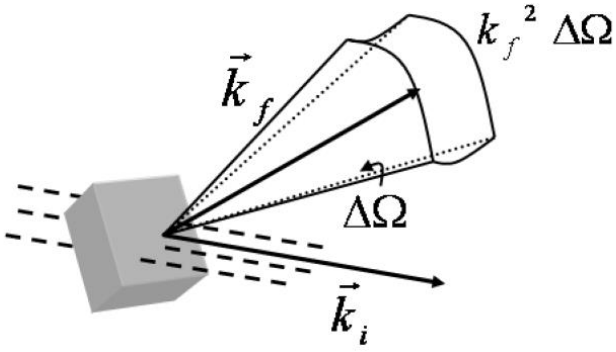

Figure 2.24: The solid angle subtended by the scattered beam at a detector [Nelsen, McMorrow, 2011].

The elastic scattering process is satisfied by introducing a delta function in the integral.

The density of states of the total system (X-ray and sample) enclosed in a volume V becomes after applying the periodic boundary conditions,

$$\rho(Ef) = \left(\frac{V}{8\pi^3}\right) Kf^2 \left(\frac{dKf}{dEf}\right)\Delta\Omega \tag{2-66}$$

Where, Kf is the momentum.

If we replace the momentum Kf by the energy Ef by using the following relation,

$$Ef = \hbar KfC \tag{2-67}$$

Thus,

$$Kf^2 \left(\frac{dKf}{dEf}\right) = \frac{Ef^2}{\hbar^3 C^3} \tag{2-68}$$

Substituting equations (2-64 to 2-66) and (2-68) in (2-64), the differential cross section is given by,

$$\frac{d\sigma}{d\Omega} = \left(\frac{V}{2\pi}\right)^2 \frac{1}{\hbar^4 C^4}\int |Mif|^2 \ \rho(Ef)\delta(Ef - Ei)dEf \tag{2-69}$$

The differential cross section equation can be expressed in terms of frequencies $\omega i = \left(\frac{Ei}{\hbar}\right)$ and $\omega f = \left(\frac{Ef}{\hbar}\right)$ as,

$$\frac{d\sigma}{d\Omega} = \left(\frac{V}{2\pi}\right)^2 \frac{1}{\hbar^2 C^4}\int |Mif|^2 \ \omega f^2\delta(\omega f - \omega i\ )d\omega f \tag{2-70}$$

For the case of X-ray scattering by a single electron with charge (e) and mass (m) the transition matrix element is,

$$\text{Mif} = \frac{e\hbar}{2m\,\varepsilon 0V}\frac{\widehat{\varepsilon\imath}.\widehat{\varepsilon f}}{\sqrt{\omega i\omega f}} < \psi i|e^{i(\omega i-\omega f)t}\, e^{i\left(\overrightarrow{Ki}-\overrightarrow{Kf}\right)\cdot\vec{r}}|\psi f > \quad (2\text{-}71)$$

Where, X-rays of energy $\hbar\omega i$, momentum $\hbar Ki$ and polarization of electric field εi are scattered into energy $\hbar\omega f$, momentum $\hbar Kf$ and polarization εf by the scatterer from initial state ψi to final state ψf. In the case of elastic scattering $\omega i = \omega f$ and electron stay in the ground state $|\psi i >$, so the transition matrix is given as,

$$\text{Mif} = \frac{e\hbar}{2m\,\varepsilon 0V}\frac{\widehat{\varepsilon\imath}.\widehat{\varepsilon f}}{\sqrt{\omega i\omega f}} < \psi i|\, e^{i\left(\overrightarrow{Ki}-\overrightarrow{Kf}\right)\cdot\vec{r}}|\psi f > \quad (2\text{-}72)$$

Therefore, the cross section for this case is given as,

$$\frac{d\sigma}{d\Omega} = \left(\frac{e^2}{2\pi\varepsilon 0mC^2}\right)^2 [\varepsilon i - \varepsilon f]^2|f(Q)|^2 \quad (2\text{-}73)$$

Equation (2-71) known as Thomson scattering cross section. Where $f\left(\vec{Q}\right)$ is the form tor, $f\left(\vec{Q}\right) = < \psi i|e^{iQ.\vec{r}}|\psi i >$ and $\vec{Q} = \overrightarrow{Kf} - \overrightarrow{Ki}$, is the scattering vector, the more important parameter in scattering experiments. **[Mishra, 2012] [Nelsen, McMorrow, 2011]**.

2.7.2 Nanoparticle assemblies on a surface: Scattering under grazing incidence small angle

Grazing-incidence small angle scattering(GISAS)is a scattering technique used to study nanostructures and thin films. In addition, this technique is used to investigate nanoparticle assemblies in two or three dimensions. The scattered probe is either X-rays, in this case called grazing-incidence small angle X-ray scattering(GISAXS) or neutrons, known in this case as grazing-incidence small angle neutron scattering(GISANS). GISAS does not require any specific sample preparation. The use of grazing-incidence geometry enhances the surface sensitivity. It includes several advantages:

- the scattering yields averaged statistical information over the illuminated sample surface.
- it is applicable to many environments such as ultra-high vacuum, different gas atmospheres and liquids,

- scattering can be performed in real time accessing kinetics phenomena, and using the variable probed depth as function of the incident angle, (4) scattering offers the opportunity to characterize buried lateral structures destruction-free as well **[Stamm, 2008]**.

Levine and Cohen **[Levine et al, 1989]** studied the dewetting of gold deposited on a glass surface. The technique was developed by Naudon **[Naudon, Brumberger, 1995]** and Co-workers studying metallic agglomerates on surfaces and in buried interfaces **[Hazra et al, 2000].**

The application of GISAS technique is the characterization of self-assembly and self-organization on the nanoscale in thin films. The systems studied by GISAS included quantum dot arrays **[Metzger et al, 1998**], growth instabilities formed during in-situ growth **[Renaud et al, 2003]**, self-organized nanostructures in thin films of block copolymers **[Smilgies et al, 2002]**, silica meso-phases **[Gibaud et al, 2003] [Chatterjee et al, 2012]** and nanoparticles **[Hazra et al, 2004] [Saunders et al, 2006]**. The scattering geometry for grazing incidence scattering is presented in figure 2.25.

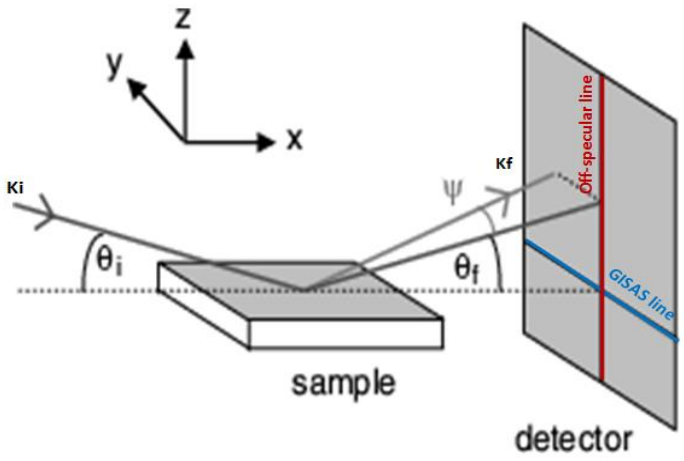

Figure 2.25: Grazing incidence small angle scattering geometry [Disch, 2010].

The sample coordinate system is defined with z perpendicular to the substrate. The incident beam enters the sample under a shallow small angle θ_i, and the scattered beam is determined by specifying two angles for the in plane component Ψ and the out of plane component θ_f. Different components of the scattering vector $\vec{Q}$ are given by **[Disch, 2010]**.

$$Qx = \frac{2\pi}{\lambda}(\cos(\theta f)\cos(\Psi) - \cos(\theta i)) \quad (2\text{-}74)$$

$$Qy = \frac{2\pi}{\lambda}(\cos(\theta f)\sin(\Psi)) \quad (2\text{-}75)$$

$$Qz = \frac{2\pi}{\lambda}(\sin(\theta f) + \sin(\theta i)) \quad (2\text{-}76)$$

Three different approaches of grazing incidence scattering that give different information will be discussed below: specular reflectivity, off-specular reflectivity, and grazing incidence small angle scattering (GISAS).

2.7.2.1 Specular reflectivity

Specular reflection phenomenon is a reflection of light or any other kind of wave from a surface, in which a light from a single incoming direction is reflected into a single outgoing direction. This phenomena can be described by the law of reflection, which states that the direction of incident ray, and the direction of reflected ray make the same angle with respect to the surface normal. The angle of incidence equals the angle of reflection as shown in figure 2.26 (i.e. a specular reflection is observed in this case). In the following equations (2-74), (2-75), (2-76), the scattering vector $\vec{Q}$ reduces just to $Qz = \frac{4\pi}{\lambda}\sin(\theta)$ without any x or y contributions. Specular reflectivity gives different information on the profile from a normal view, such as the layer thickness, roughness, or layer sequence **[Disch, 2010]**.

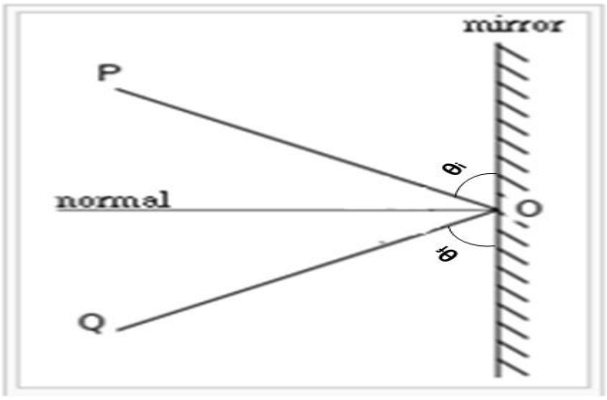

Figure 2.26: Diagram of specular reflection.

Total reflection occurs at incident angles below the critical angle, in this case the detected intensity remains constant. Nevertheless, at higher angles, the scattered intensity decreases with Q^{-4} **[Disch, 2010]**. The critical angle of total reflection is defined via Snell's law:

$$\frac{\cos(\theta i)}{\cos(\theta t)} = \frac{Kt}{Ki} = n1 \quad (2\text{-}77)$$

Kt and Ki, are the transmitted and incident wave vectors**[Disch, 2010]**.

2.7.2.2. Off-specular scattering

Off-specular scattering is measured in dependence of the incident angle. Off-specular scattering means $\theta i \neq \theta f$ and $\Psi = 0$, according to equations (2-74), (2-75), (2-76), the scattering vector just has only contributions in x and z direction, without y-contribution:

$$Qx = \frac{2\pi}{\lambda}(\cos(\theta f) - \cos(\theta i)) \quad (2\text{-}78)$$

$$Qz = -\frac{2\pi}{\lambda}(\sin(\theta f) + \sin(\theta i)) \quad (2\text{-}79)$$

The x-contribution for scattering vector is much smaller than the z-contribution when the incident and scattered angles are small. In a typical off-specular measurement, θi is scanned in dependence of θf or vice versa. Off-specular scattering can give depth-resolved information on lateral structures **[Disch, 2010]**.

2.7.2.3 Grazing Incidence Small - Angle X-ray Scattering(GISAXS)

In order to determine nanostructure along both the normal and parallel directions in a thin film, the use of grazing incidence X-ray technique together with the small-angle scattering techniques, namely grazing incidence small-angle X-ray scattering (GISAXS) is required **[Ito, 2009].** Grazing-incidence small-angle X-ray scattering is a kind of grazing-incidence small-angle scattering, and it is turned out to be a powerful advanced scattering technique for the investigation of nanostructured polymer films, like Atomic Force Microscopy(AFM). GISAXS also has a much larger statistical significance compared to AFM. It is used extensively to study the shape, morphology and arrangement of nanoparticles and mesoscopic objects. In addition, it provides a statistical average of lateral electron density profiles over a large area, this is not possible with electron microscopes **[Mishra, 2012]**.

GISAXS is a versatile tool for characterizing nanoscale density correlations or the shape of nanoscopic objects at surfaces, buried interfaces, or thin films. GISAXS combines features from small angle X-ray scattering and diffuse X-ray reflectivity and can be considered as the little brother of grazing incidence diffraction. It explores the whole scattering from the surface in all directions, typically utilizing an area detector. The GISAXS gains access to a wide range of lateral and vertical structure. In particular, it is sensitive to the morphology and preferential alignments of nanoscale objects at the surface or inside the thin films.

GISAXS has many applications, such as, long range ordering of block copolymers for dense data storage, composite membranes for artificial photosynthesis, inorganic nanocomposites for electrochromic windows, butteries and fuel cells, lithographic patterning, self-assembly of nanoparticles in block copolymer thin films, nanocomposites for solar cells, virus nano-fiber tissue engineering materials, and block copolymer self-assembly. GISAXS data can be collected very rapidly using a two-dimensional (2D) detector. Since intensities measured along Qy and the Qz directions, can be recorded simultaneously by a 2D detector, GISAXS has the advantage of easy characterization of anisotropic nanostructures and for a dynamical study of phase transition in thin films. However, GISAXS with a 2D detector has a disadvantage of detecting air scattering along the path besides the nanostructures. In order to minimize air scattering, a vacuum or helium path is used **[Ito, 2009].**

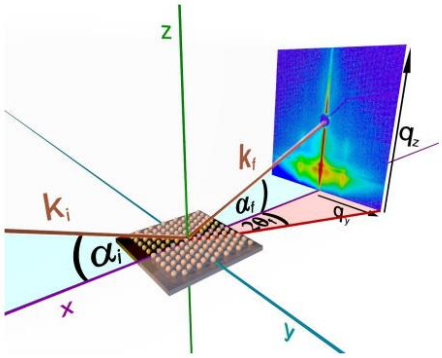

Figure 2.27: Grazing-incidence small-angle X-ray geometry. Image taken from [Meyer, 2011].

The Geometry of GISAXS experiment is illustrated in figure 2.27. A monochromatic X-ray beam with the wave vector Ki strikes a surface with a very small incident angle αi with respect to the surface. Where, z-axis is the normal to the surface plane, the x-axis is the direction along the surface parallel to the beam and y-axis perpendicular to the beam. The X-rays are scattered along K_f in the direction (2θf , αf).

Chapter 3 Instruments

3.1 Scanning Electron Microscope (SEM)

With a scanning electron microscope it is possible to provide a direct space image of the sample with a resolution in the nanometer range, due to the very narrow electron beam. The image is produced by scanning the sample of interest with a focused beam of electrons. Since their development in the early 1950s', scanning electron microscopes have developed new areas of study in the medical and physical science communities. The SEM has allowed researchers to examine a much bigger variety of specimens.

The scanning electron microscope has many advantages over traditional microscopes. It has a large field depth, which allows more focusing many specimen at once. The SEM also has much higher resolution, with closely spaced specimens magnified at higher orders. The scanning electron microscope is one of the most useful instruments in research today.

A beam of electrons is produced at the top of the microscope by an electron gun. The electron beam follows a vertical path through, which is held in a vacuum. The beam travels through electromagnetic fields and lenses, which focus the beam down toward the sample. Once the beam hits the sample, electrons and X-rays are ejected from the sample (figure3.1), due to inelastic collision.

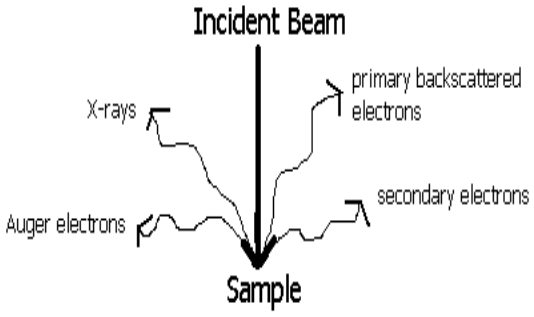

Figure 3.1: beam hits the sample in the SEM, electrons and X-rays are ejected from the sample.

Detectors collect these X-rays, backscattered electrons, and secondary electrons (SE) and convert them into a readout signal on a screen. This produces the final image.

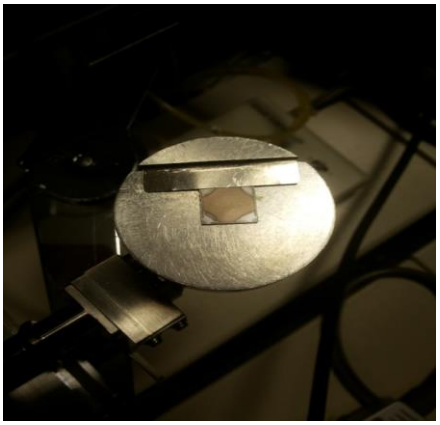

Figure 3.2: a small chamber in the where the sample is placed.

Special preparation must be done to the sample, because the SEM operates in vacuum conditions. This means samples must be died because the water would vaporize in the vacuum.

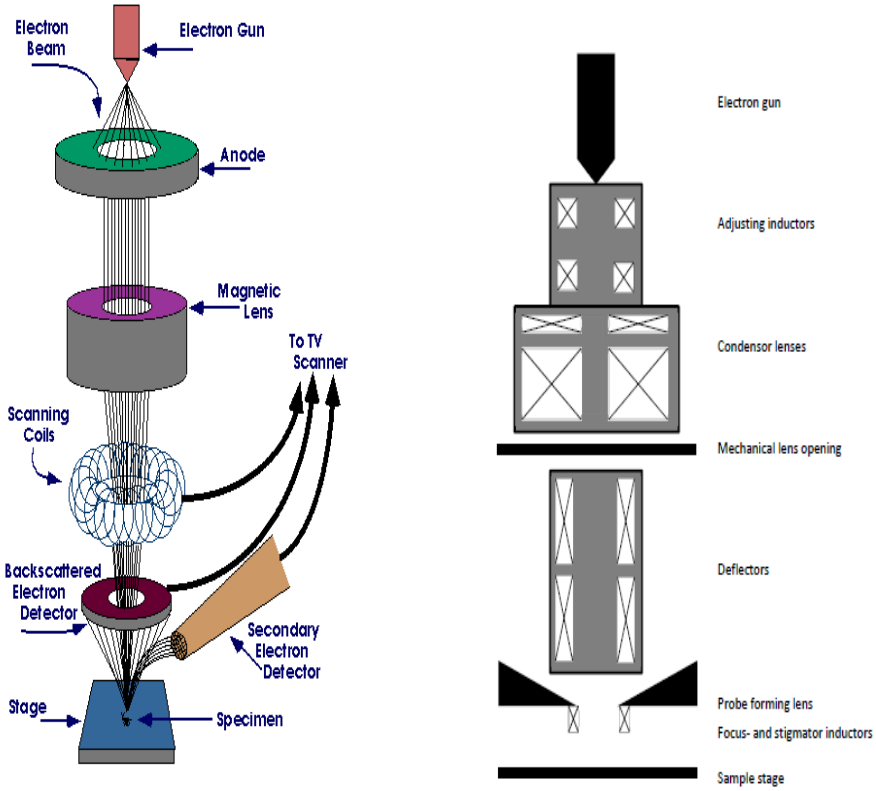

a) **b)**

Figure 3.3: a) diagram of scanning electron microscope. Image taken from [Scanning Electron Microscope, 2003] b)principal set-up of an electron optical column: Between the electron gun and the sample holder several electro-optical lenses are mounted to focus the electron beam and set the magnification. Image taken from [Wilbs, 2013].

Metals are conductive and need no preparation. Non-metals need to be made conductive by covering with a thin layer of a conductive material, or by using a sputter coater that uses an electric field and argon gas. The sample is placed in a small chamber (figure3.2) in vacuum. A typical SEM setup is shown in figure 3.3.a. It consists of an

1. An electron optical column is shown in figure 3.3-b: an electron source, magnetic lenses to de-magnify the beam, magnetic coils to control and modify the beam, apertures to define the beam, and prevent electron spray, etc.
2. A vacuum system: a chamber that keeps vacuum, pumps to produce it, valves to control it, and gauges to monitor it.
3. A signal detection and display: detectors that collect the signal, and electronics, which produce an image from it.

3.2. Gallium Anode Low-Angle X-ray diffractometer (GALAXI)

GALAXI is a high resolution diffractometer for GISAXS. The structures investigated by the GALAXI are in order of $\mathbf{D} = \frac{\mathbf{2\pi}}{\mathbf{Q}}$ =2….100 nm. Where, D is the diameter and Q is a wave vector. GALAXI uses the Bruker AXS Metaljet X-ray source **[GALAXI, 2002].** The sample can be adjusted in the beam with 2 translational and 2 rotational degrees of freedom. The detector distance can be adjusted between ca. 800 mm and 3500 mm to adapt the angular range and resolution to the requirements of the experiment. The beam path is evacuated from the source up to the detector, and the samples are located in the vacuum area.

GALAXI (Figure 3.4 and 3.5) is used for the investigation of: The structure of self-organized nanoparticles assemblies, size distribution of nanoparticles in solution, porosity in coating layers, the structure of liquid crystals.

Different measurements like SAXS and surface-near SAXS measurements were carried out at high brilliance laboratory Gallium Anode Low Angle X-ray Instrument GALAXI at Forschungszentrum Jülich GmbH (Germany). The instrument was based on the former B1 beamline of the DORIS synchrotron at HASYLAB (Deutsches Elektronen Synchrotron-DESY, Hamburg, Germany) and now equipped with a Bruker AXS Metal Jet X-ray source providing highly intense ($10^9 s^{-1}$) X-rays with a wavelength of 1.34 Å.

For SAXS measurements of the nanoparticles, a dilute aqueous dispersion of the particles was sealed in different size of quartz capillary, and the measured data was averaged circular-

ly, simulated by using the SasView software **[SasView, 2012],** and corrected for solvent scattering for evaluation.

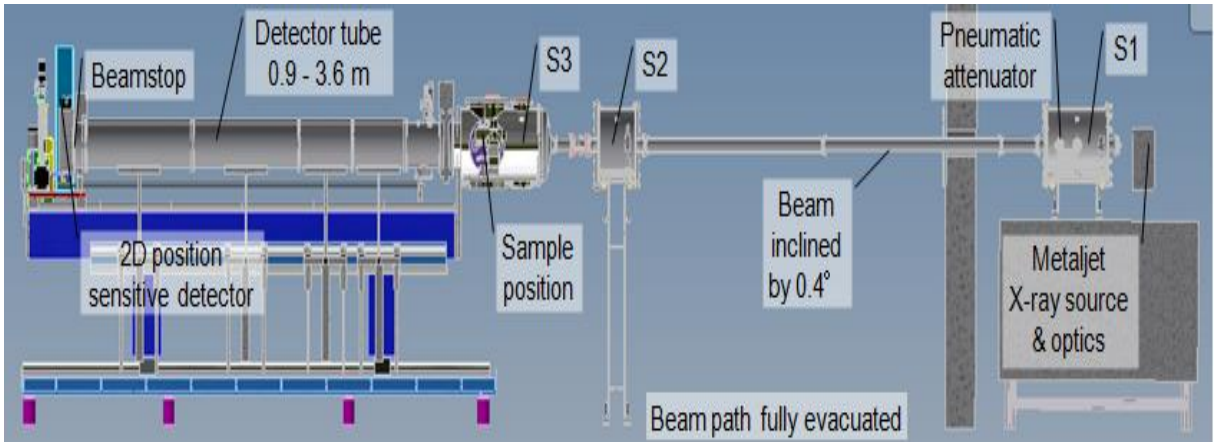

Figure 3.4: GALAXI diffractometer set up. Image taken from [Rücker et al, 2012].

The data obtained is compared to simulations based on the particle morphology obtained from SEM characterization. Surface-near SAXS measurements by nanoparticle assemblies deposited on silicon substrates were carried out with the sample aligned horizontally in the direct beam with incident angles of 0.3°–0.5° were chosen .

Figure 3.5: GALAXI diffractometer with sample chamber and detector.

Chapter 4 Results and Discussion

4.1 Samples

Iron oxide nanoparticles were selected in this study. They have interesting and great magnetic properties. Many chemical methods can be used to synthesize magnetic nanoparticles to yield iron oxide nanoparticles with a narrow size distribution. They include micro emulsions, sol-gel synthesis, sono-chemical reactions, hydrothermal reactions, hydrolysis and thermolysis of precursors, flow injection syntheses, and electro spray syntheses **[Wu et al, 2008]**.

We used spherical iron oxide nanoparticles with a diameter of 20 nm and manufactured by Ocean Nanotech LLC. They were dispersed in toluene and synthesized by thermolysis of precursors and coated with oleic acid.

Iron oxide nanoparticles are frequently dispersed in a long-chain substance of hexadecane. The common example is oleic acid molecule (CH3 (CH2)7CH=CH (CH2)7CO2H), amphiphile consisting of a hydrophilic head group (-COOH) and a hydrophobic unbranced hydrocarbon tail (-C17H33) with one double bond **[Hazra et al, 2004]** in the middle, forming a kink. Oleic acid prevents or decreases the agglomeration of nanoparticles and increases the stability that gives rise to the mono-dispersity **[Mishra et al, 2008]**.

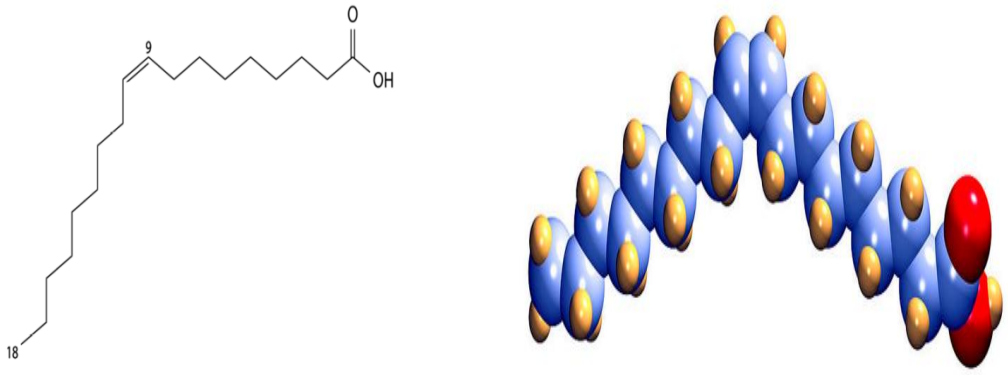

Figure 4.1: a) Oleic acid structure b) Geometric representation of the oleic acid molecule. Carbon, hydrogen, and oxygen atoms are represented as balls in blue, yellow, and red, respectively. Images taken from [Wikipedia, 2015].

Different depositions methods were used to transfer the iron oxide colloid on pre-structured and none restructured silicon wafers. Monolayer, sub-monolayer and ordered arrays of iron oxide nanoparticles were formed and the oleic acid was removed by different techniques.

4.2 Deposition routes

The iron oxide colloids are deposited on a solid substrate by two different deposition methods as shown in figure 4.2: the drop-casting and spin-coating methods. The solid substrates, are patterned silicon wafers with rectangular channels on the surface. The channels have a pitch size of 300 nm, and depth of 100 nm as shown in figure 4.3. The wafers used have a natural oxide layer and were cut into 1×1 cm^2 and cleaned in a two-stage process:

a) **b)**

Figure 4.2: Schematic of deposition routes: a) Drop-casting: A drop is deposited on the sample and left to allow the solvent spread and dry. b) Spin coating: A small amount of the colloid is deposited at the center of wafer center and set into spinning. The colloid spreads over the surface forming a mono sub or multi layers.

The first step is to clean silicon wafers, by placing them inside a beaker filled with an organic solvent called ethyl acetate. Then put the beaker in an ultrasonic bath for 15 minutes to remove all dirt from the surface. The wafers are taken out from the beaker, and put in another beaker filled with ethanol and put again in an ultrasonic path for another 15 minutes to clean the wafers from remains of ethyl acetate. Wafers are stored in ethanol and dried with dry nitrogen gas before the colloid deposition. The nanoparticles tend to arrange in ordered arrays or assemble in different ways depending on the particle size and shape, and type of interactions (i.e. Van der Waals, Magnetic, Steric repulsion or capillary forces as d scribed in chapter 2.4) **[Mishra, 2012]**. The wafers specs are shown below Table 4.1

Table 4.1: Pre-structured substrate (patterned substrate)

Material	Diameter	Orientation	Thickness	Polishing	QTY	Price/pc
Si	2”	(111)	2.75 µm	1 side epi polish	9 pcs	700€ /pc

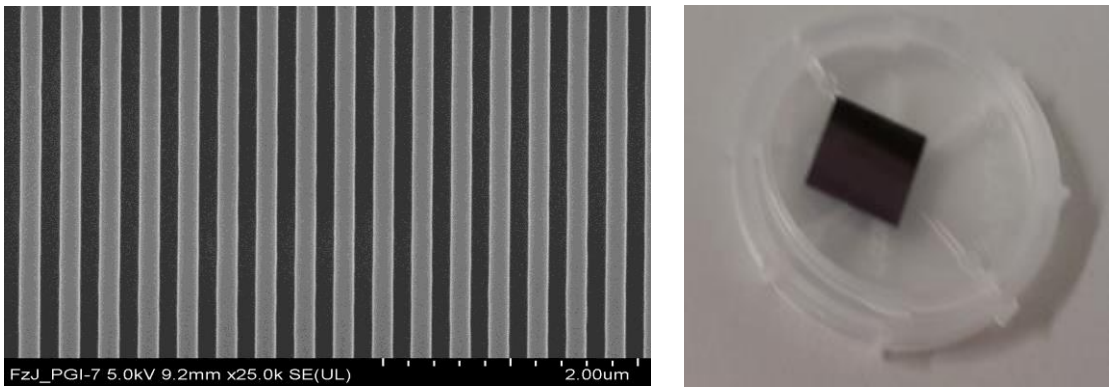

Figure 4.3: left) SEM image of patterned silicon substrate. The periodicity of the stripes is about 300 nm and the depth is 100 nm. right) The commercial patterned silicon substrate.

4.2.1 Drop-casting

The solution drops are put on the surface with relatively fast solvent evaporation, The thickness of the layers is proportional to the solution concentration. This method has several advantages: it is simple with no waste of material. However, it cannot extend to large area coverage, and the thickness is hard to control, in addition to poor uniformity.

A small amount of solution of nanoparticles were applied to a $1 \times 1\ cm^2$ wafers (pre-structured and non-pre-structured) using a micropipette. Evaporation time was about 24 h.

For the none pre-structured wafers as shown in figure 4.4a most of the smooth surface was covered with well-ordered areas with hexagonal arrangement visible. Multilayers of nanoparticles were also observed with high concentrations (figure 4.4b). In figure, 4.4c shows a transition between mono and multilayers. In the low concentration areas, monolayers with hexagonal order were observed (figure 4.4d). In addition, the amount of nanoparticles on the edges was higher compared to the central region.

Whereas, when deposited nanoparticles by the same method on patterned silicon wafers. Approximately ordered arrays of nanoparticles is observable. Where these arrays contains a multilayer or sub-monolayer of nanoparticles and these nanoparticles have a hexagonal order as in figure 4.5.

The process can be understood by combining several modes: a large interaction between the nanoparticles and the substrate leading to Frank-Van-Der-Merwe like growth forming in a smooth surface **[Bigioni, 2006]**. The morphology of drop-casting deposition route of nanoparticles is controlled by evaporation kinetics and particle interaction with liquid-air interface. In addition, a two-dimensional solution of nanoparticles at the liquid-air interface is dynamically produced by rapid early-stage evaporation.

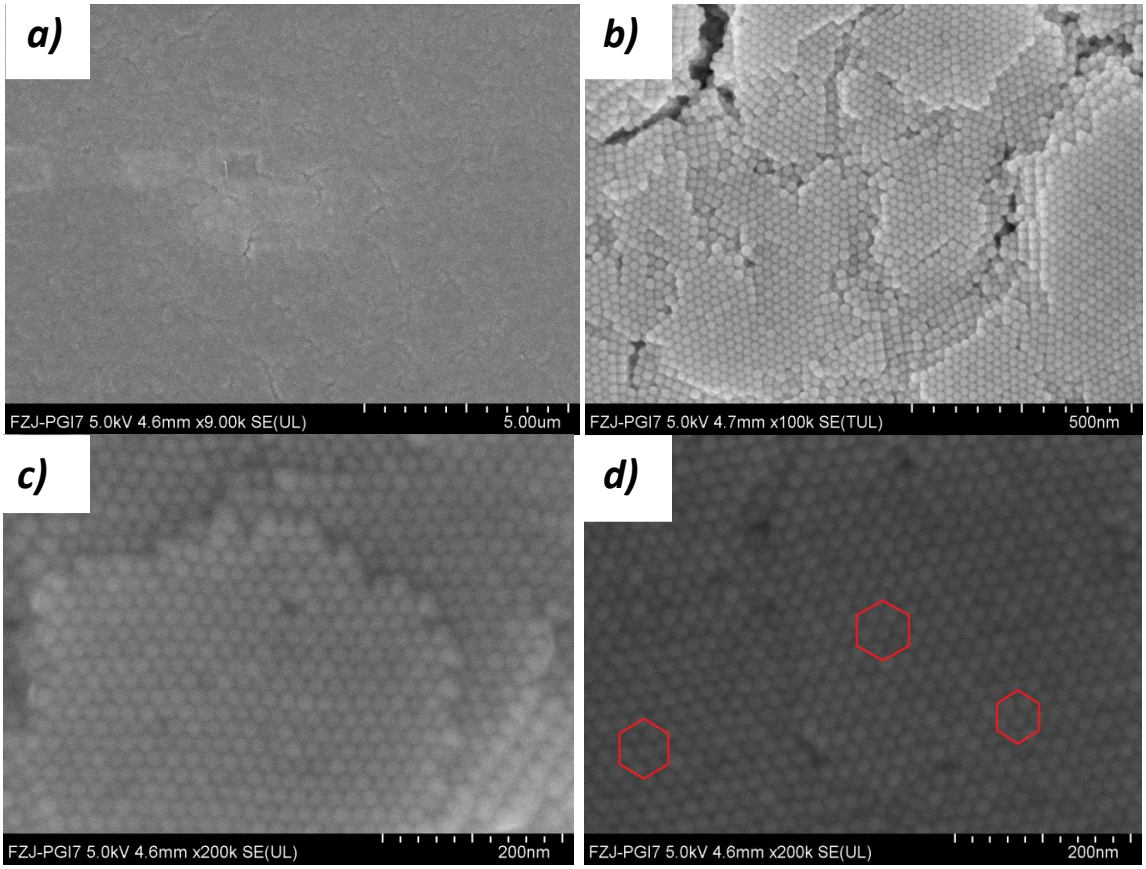

Figure 4.4: SEM images of iron oxide nanoparticles deposited on a silicon wafer by drop casting taken in the middle of the sample. a) Close-up of a smooth surface: several well-ordered areas with hexagonal arrangement are visible. b) Multilayer. c) Transition between mono and multilayered. d) A monolayer with hexagonal order.

This leads that the nanoparticles islands nucleate and grow. In addition, the islands stick to the interface. When a drop of a solution of nanoparticles dries on a solid surface, it leaves behind coffee-stain like rings of material with lace-like patterns or clumps of particles in the interior. This phenomenon is known as coffee-ring effect. It is manifested in systems with diverse constituents, ranging from large colloids, to nanoparticles and individual molecules **[Yunker et al, 2011] [Beegan et al, 1997]**. The contact line of the drying drop is pinned dur-

ing the evaporation process so the liquid evaporating from the edge must be replenished by liquid from the interior. The outward flow can carry virtually all the dispersed nanoparticles to the edge, resulting in a thicker nanoparticles layer compared to the center **[Scriven, 1988]**.

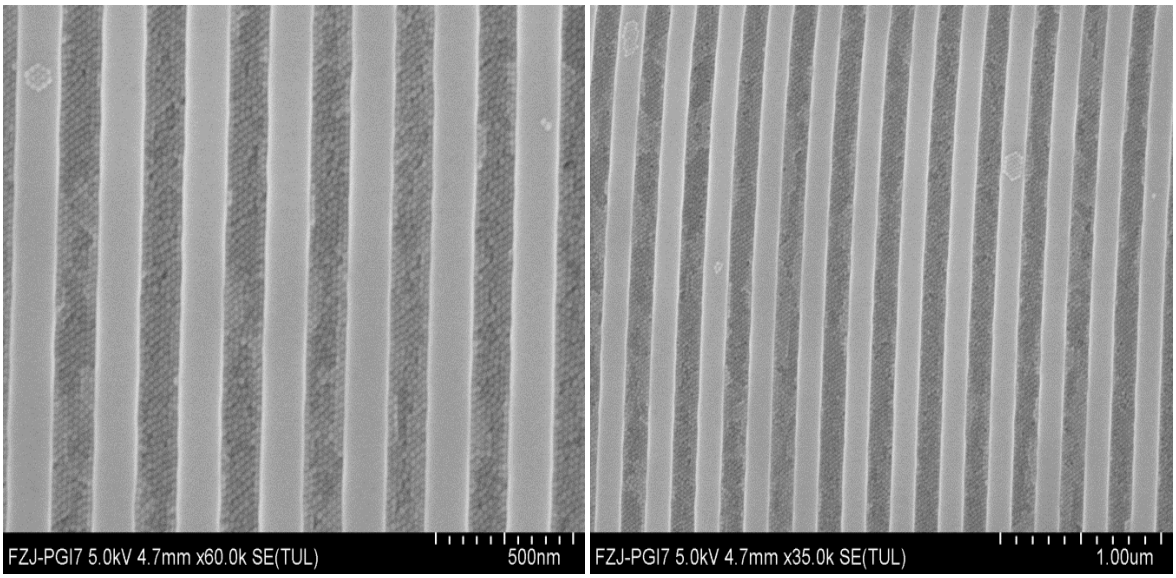

Figure 4.5: SEM images of iron oxide nanoparticles deposited on patterned silicon by drop-casting method with hexagonal order.

4.2.2 Spin coating

Spin coating is a typical procedure that involves depositing a colloid on a substrate. Usually a small amount is applied on the center of the substrate, which is either spinning or not spinning at all. The machine used for spin coating is called spin coater, or spinner. After the deposition the substrate is rotated at different speeds to spread the colloid across the wafer by centrifugal force. The spinning continues while the fluid moves off the edges of the substrate, until the desired thickness of the layer is achieved. The thickness of the layers depends on several factors: the spin speed, time, and concentration of the colloid **[Hanaor et al, 2011]**. Spin-coating method has many advantages: good uniformity, reproducibility and good control on thickness. Additionally to its advantage, it has disadvantages: waste of material, no large area and the layer dried fast. Spin coating is widely used in microfabrication of oxide layers using sol-gel precursors, where it can be used to create uniform thin films with nanoscale thickness **[Colina, Acker, 2000]**.

Spin coating was first used to apply coatings of paint and pitch seventy years ago. The first spin coating device was developed in 1958 by Emslie et.al. This model has been used as a basis for future complicated models.

Spin-coating process takes the following steps: first, $1 \times 1\ cm^2$silicon wafer (pre-structured and non-prestructured wafers) was put on the spin coater. Then a small amount of colloid solution with nanoparticles was deposited onto the wafers. After that accelerate the wafers at different velocities with different for variable times. During spinning, the solution is evaporates leaving the nanoparticles forming their various configurations.

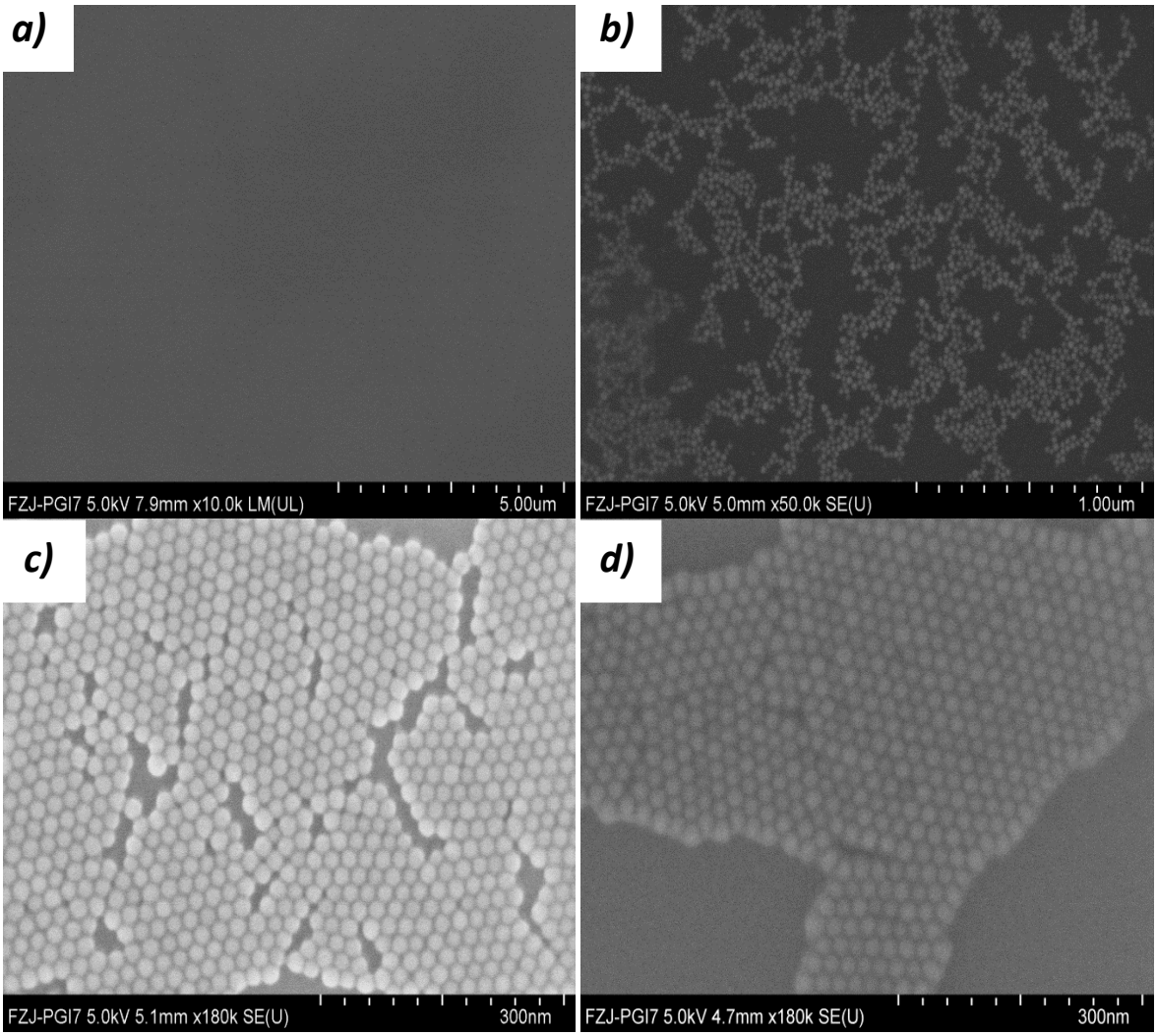

Figure 4.6: SEM images of iron oxide nanoparticles deposited on a silicon wafer by spin coating. Images were taken from the middle of the sample. a) Smooth surface. b) Smooth surface with a disordered layer on top. c) Close-up: sub-monolayer with speed 50 rpm for 8s and hexagonal order. d) Close up: Sub-monolayer with speed 30 rpm for 8s and with hexagonal order.

The results of depositing nanoparticles on none pre-structured silicon wafers are shown in figure 4.6. In figure 4.6a, the surface is homogeneous and smooth. A partial second layer on top of the first forms islands (figure 4.6b). Figure 4.6c-d shows sub-monolayers with hexagonal order,

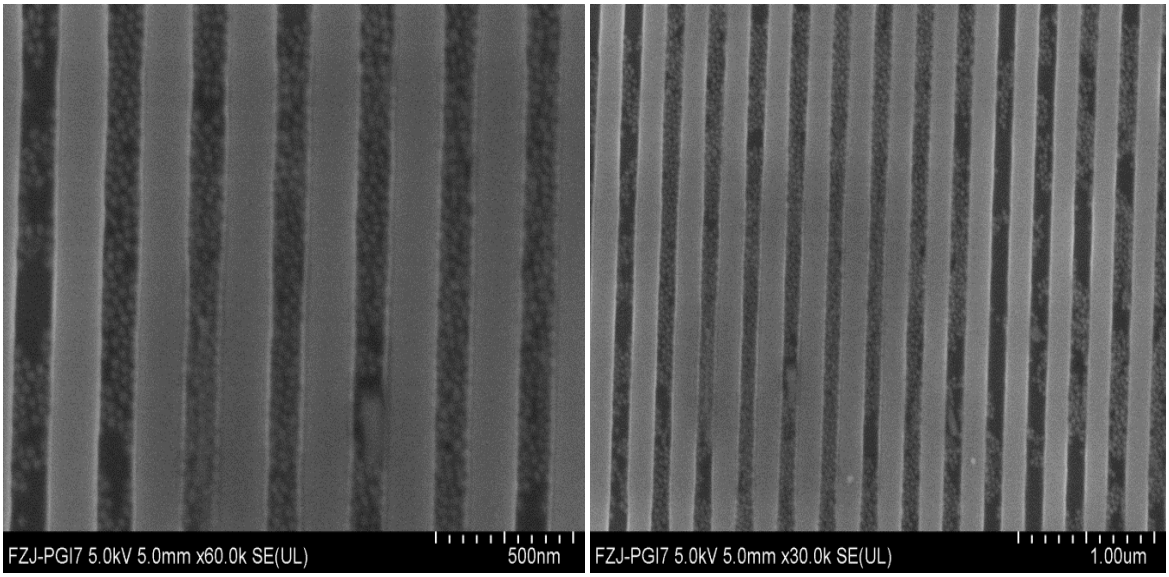

Figure 4.7: SEM images of iron oxide nanoparticles deposited on patterned silicon by spin coating method with speed 20 rpm for 20s.

The result of depositing the nanoparticles on a pre-structured silicon wafers is depicted in figure 4.7a. A close-up shows some partially ordered arrays. They are not fully ordered due to variations in speed of rotation, time and the concentration of the colloid. At certain angular speeds thin dispenser layers are formed. This thickness and homogeneity of the layer depends on the wettability of the dispenser on the substrate **[Goya et al, 2005]**. A smooth and homogeneous surface with a high degree of self-assembly can be reached. The solvent evaporation, speeds up the process and due to the high vapor pressure of toluene, the layers get very thin. The nanoparticles ordering is due to capillary forces **[Huber, 2005]**. Spin-coating was used in preparing all samples used for magnetic measurements.

4.3 Dilution

The colloid was diluted with toluene at different proportions and deposited by different methods as described in section 4.2. For a 1:10 ratio, monolayer and sub-monolayer of na-

noparticles emerged (figure 4.8). A sub-monolayer with a rotational speed 30 rpm and rotational time 8s(figure 4.8 a-b) is more dense than the sub-monolayer with more rotational speed (50 rpm) and with the same rotational time(figure 4.8 c-d). A monolayer of nanoparticles observable when using a smaller rotational speed (20 rpm) and with higher rotational time (20s) (figure 4.8 e-f). The arrangements of nanoparticles due to nanoparticles interaction, such as a strong dipolar interaction between nanoparticles, capillary forces…etc.

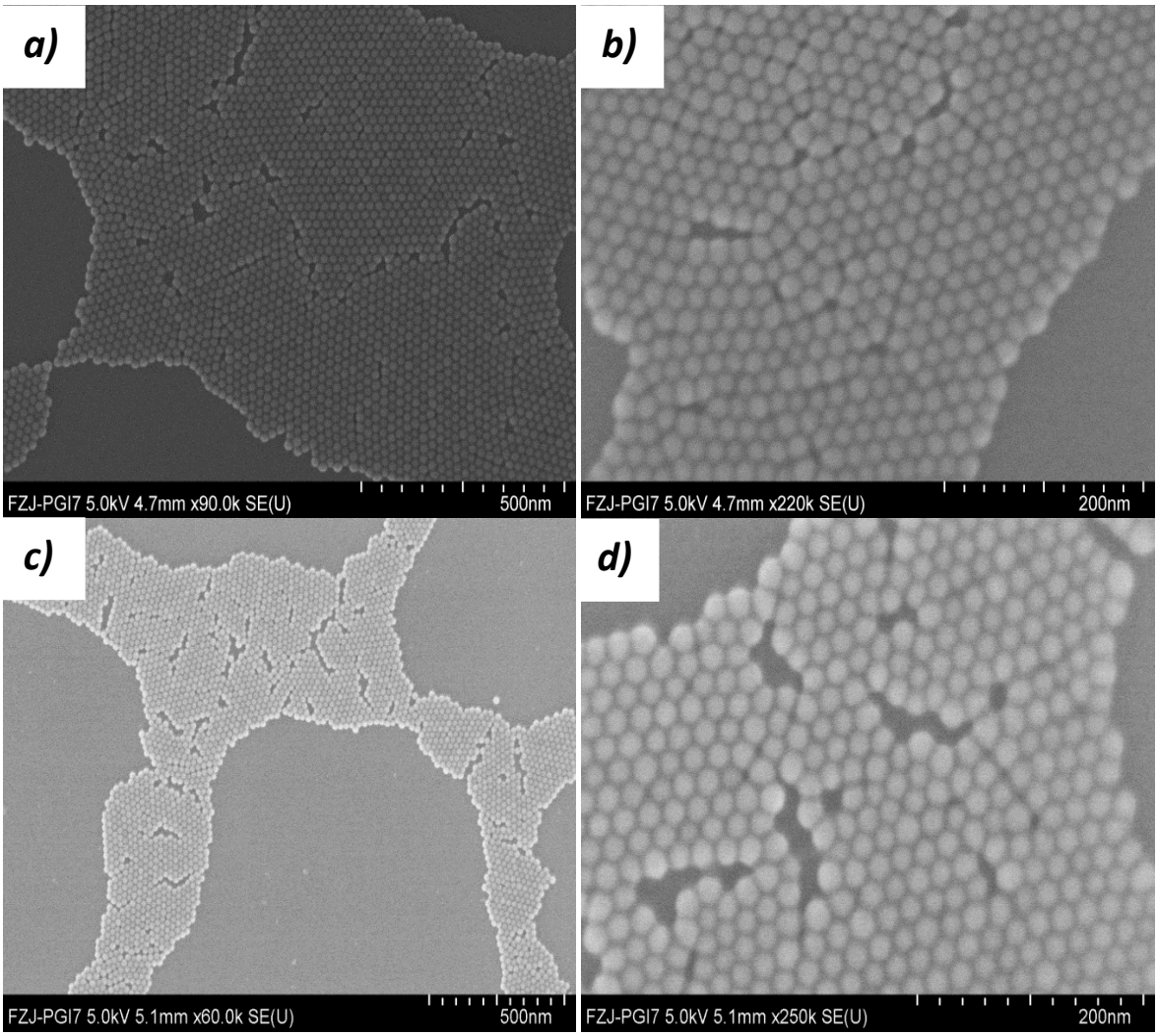

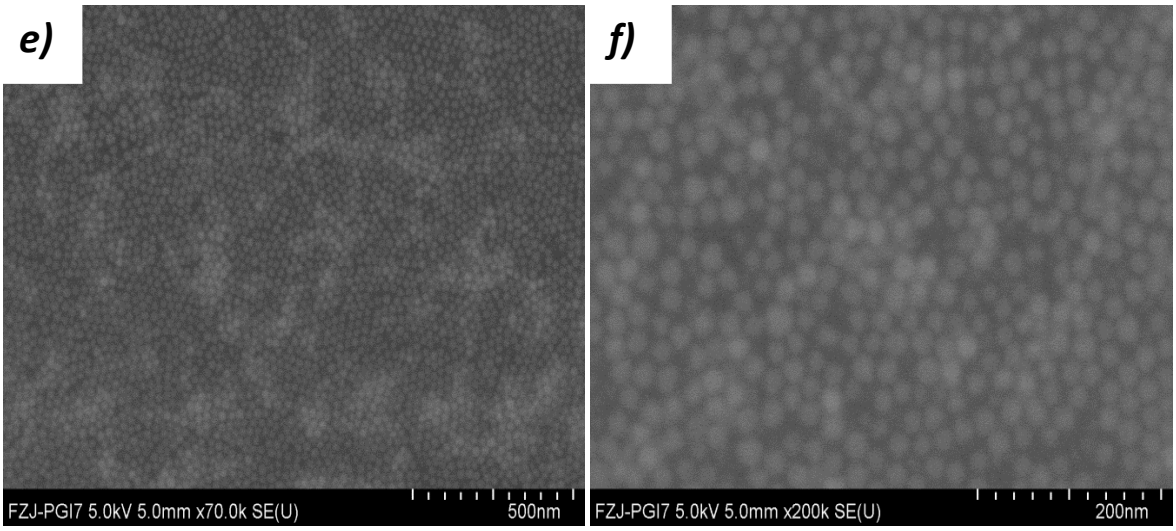

Figure 4.8: SEM images of iron oxide nanoparticles deposited on a silicon wafer by spin coating diluted with toluene at a ratio of 1:10. The pictures were taken in the middle of the sample. a-b) Close up Well-ordered sub monolayer with speed 30 rpm for 8s. c-d) Sub monolayer with speed 50 rpm for 8s. e-f)Monolayer with speed 20 rpm for 20s.

4.4 Oleic Acid Removal

4.4.1 Plasma processing

One method to remove the oleic acid shell is plasma etching. It involves a high-speed stream of glow discharge (plasma) of an appropriate gas mixture shot (in pulses) at the sample. The plasma source can be either charged (ions) or neutral (atoms and radicals). The substrates are immersed in a reactive gas (plasma). The layer is removed by chemical reactions. During the process, the plasma generates a volatile etch products at room temperature, and these products are carried away in the gas stream. A TePla 300 plasma processor was used with an oxygen flow of 200ml/min and a power of 300W **[Abrikosov et al, 1963-1975]**. The colloid was diluted with toluene in 1:10 ratio and deposited on the wafers. Afterwards the samples were treated with the oxygen plasma for 5 min at a pressure of approximately 0.7 mbar. As figure 4.9 shows the treated samples did not change much after 5 min (figure 4.9 c-d) compared to the untreated ones (figure 4.9 a-b). The nanoparticles in the treated samples became more visible and have a spherical shape. When removing the oleic acid shell the Van der Waals interaction dominates.

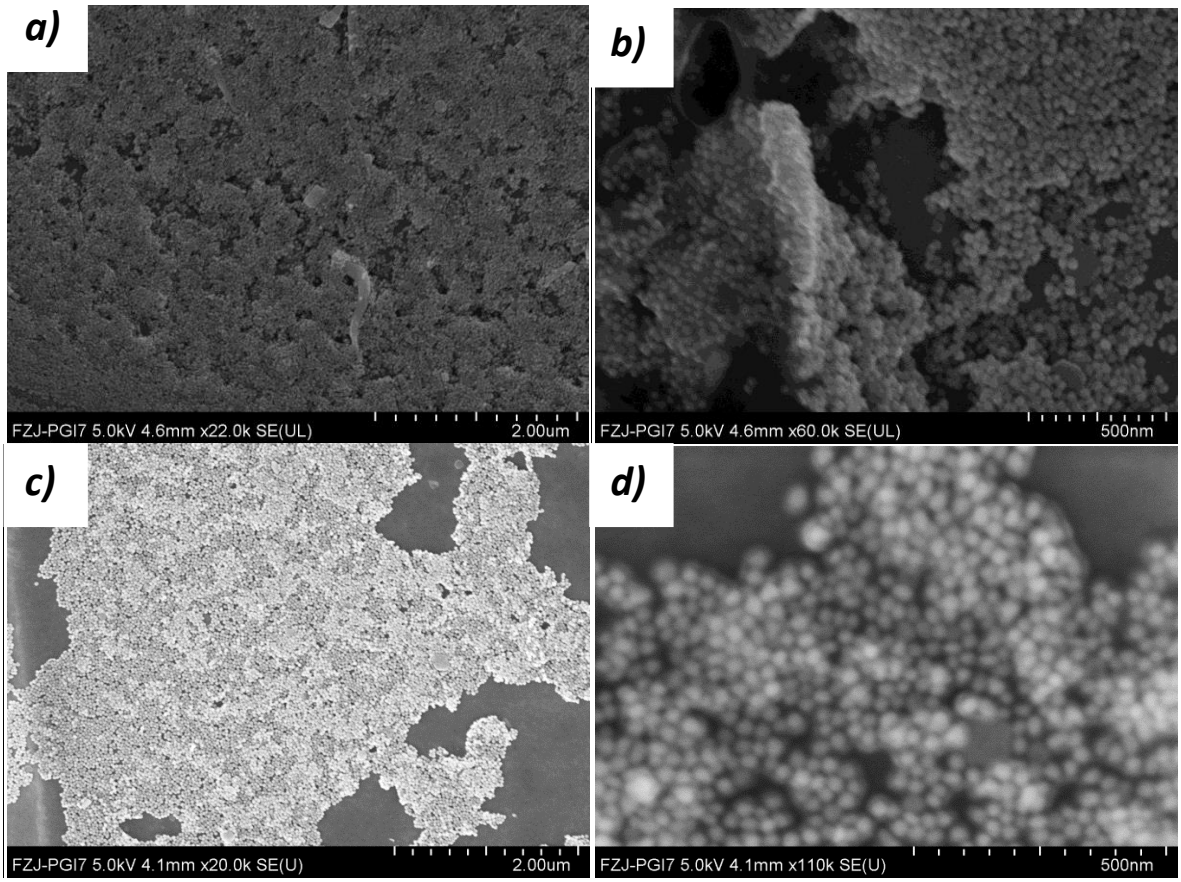

Figure 4.9: SEM images of iron oxide nanoparticles diluted with toluene in a proportion of 1:10 and deposited on a silicon wafer by spin coating. The pictures were taken in the middle of the sample. a-b) Without plasma treatment. C-d) 5 min oxygen plasma treatment.

4.5 Structure

4.5.1 SEM

Scanning Electron Microscopy (SEM) images were obtained using a Zeiss Neon 40 microscope operated at 5 kV. A drop of dilute nanoparticle dispersion was placed on a silicon substrate and evaporated for determination of the particle morphology and size distribution.

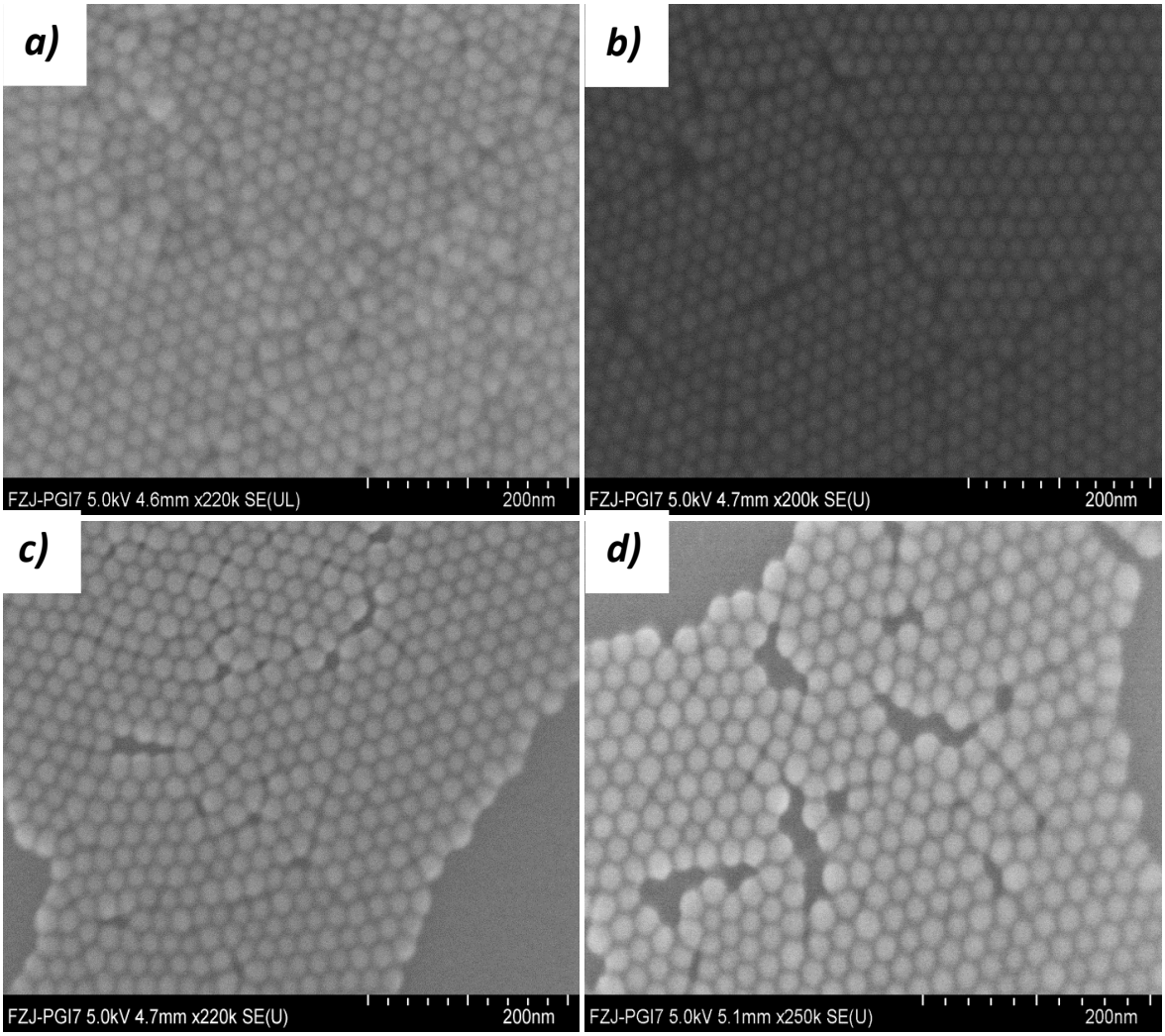

Figure 4.10: SEM images of iron oxide nanoparticles diluted with toluene in a proportion of 1:10 and deposited on a silicon wafer. The pictures were taken in the middle of the sample. a) drop casting (DC), b-c) Spin coating 30 rpm (SC-30), d) Spin coating 50 rpm (SC-50).

Particle size histograms were obtained (figure 4.11) by manual measurement of diameter, length, and aspect ratio of 160 particles. The mean size and size distribution were obtained by fitting and the size of nanoparticles was measured in different SEM images, by using "GIMP" software. This was done for four different images (figure 4.10), i) a-DC, ii) b-SC 30rpm, iii) c-SC 30 rpm, iv) d-SC 50 rpm. The results of this images are shown in Table 4.1. Curiously, the average between the different images is significantly different. This might indicate an error in the adjustment of the SEM, but could be caused by bad statistics (there are 160 data points for each image). Plotting the data in a histogram clearly reveals a bimodal distribution (Figure 4.11). The result of the diameter (dNP) and size distribution σ of nano-

particles after LogNormal fitting was presented in Table 4.1. The size and size distribution have to be determined by SAXS technique, which is much more accurate.

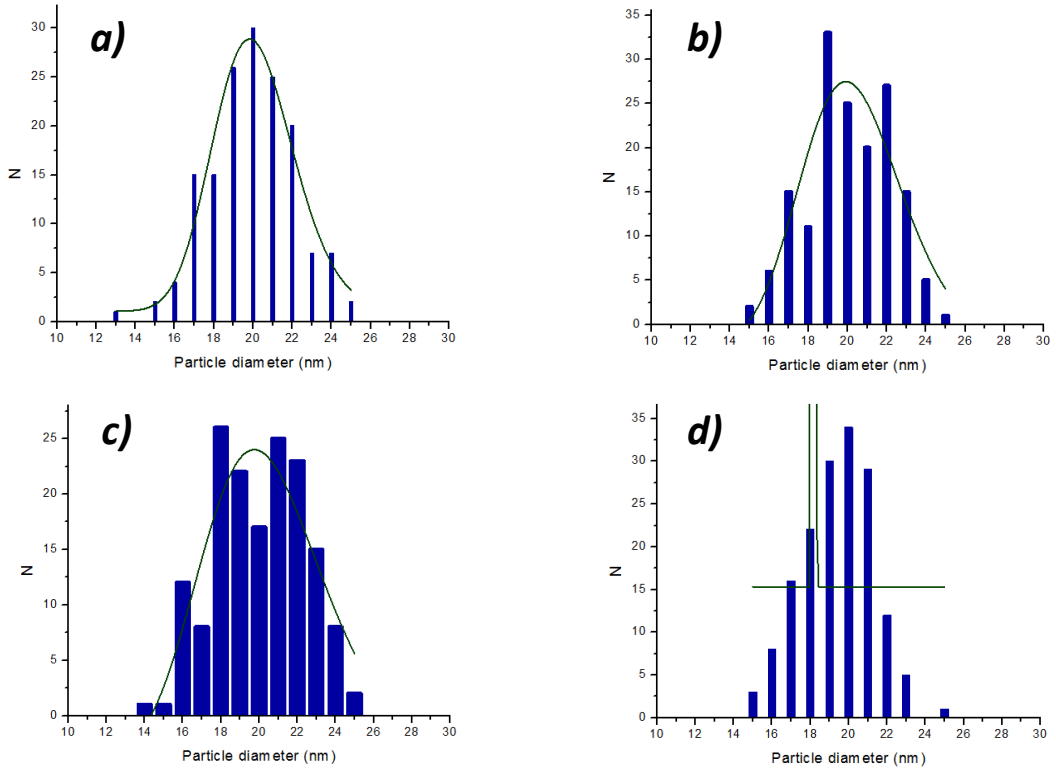

Figure 4.11: The distribution of the measured NP diameters for the four analyzed SEM image. a) drop casting (DC), b-c) Spin coating 30 rpm (SC-30), d) Spin coating 50 rpm (SC-50).

Image	Image scale (nm/px)	dNP (nm)	σ(%)
a-DC	0.43	20.0± 0.2	0.5
b-SC-30	0.23	20.2±0.4	0.6
c-SC-30	0.22	20.2± 0.5	0.7
d-SC-50	0.38	18.2	0.014

Table 4.2: The measured NP size and size distribution in the four analyzed SEM images.

4.5.2 SAXS: Size and size distribution

For SAXS measurements, the nanoparticles dispersions were filled into Hilgenberg quartz capillaries with inner diameter of 1.5 mm and a wall thickness of 0.01 mm. The capillaries were closed with PMMA stoppers using Loctite 408 glue and a sphere of silicon above the slot of the capillaries.

SAXS measurements were performed with a fixed incoming wave-length of $Ca_{K\alpha}$ with $\lambda =$ 1.3414 $\AA^{\circ}$ and a fixed sample to detector distance of 3546 cm, with a beam size of 0.7 in all

directions, yielding a maximal accessible Q range of 0.004 to 0.2 $A^{\circ -1}$. SAXS provides a precise determination of the nanoparticle size and size distribution.

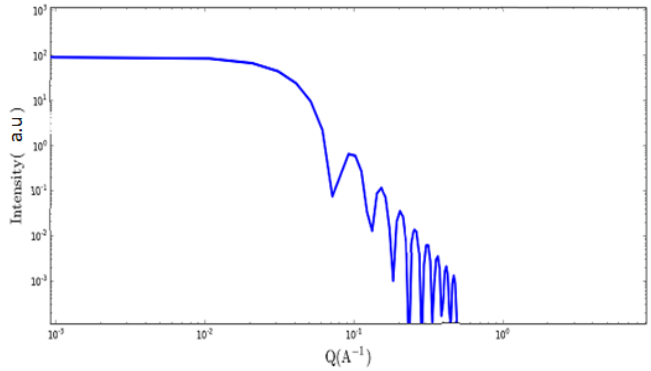

Figure 4.12: Spherical form factor used to fitting the SAXS data to calculate the size and size distribution of the nanoparticles.

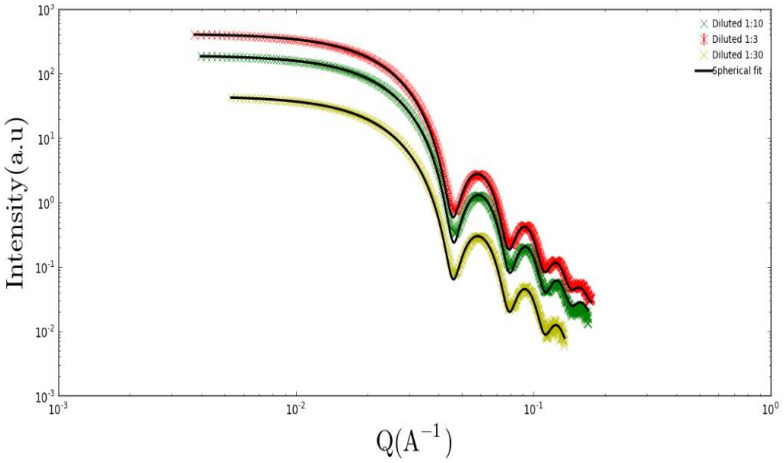

Figure 4.13: Small-Angle X-ray scattering by iron oxide nanoparticles dispersions in toluene of different concentration. Intensities have been scaled for display refinements of spherical form factor are presented by black solid lines. The most curves arrange of $0.04 \leq q \leq 0.2$

Figure 4.13 presents the reduced and normalized SAXS data to absolute units by iron oxide nanoparticles. Not all of the presented SAXS curves exhibit a structure factor due to particle agglomeration. The particle size should be independent of the concentration, and matching with a spherical form factor (figure 4.12) leads to an approximate particle radius r and size distribution σ, which are listed in table 4.2. It is clear from figure 4.13 that for the same Q value the sample that has more nanoparticles concentration has a higher intensity values. The distribution has only influence on the minima depth , which is indicative of a reasonably narrow size distribution. This is in good agreement with earlier results based on scanning electron microscopy technique.

Sample	σ (%)	$r_{NP}(A^{\circ})$
Diluted 1:3	6%	97.231±0.0445
Diluted 1:10	5.5%	96.688±0.49941
Diluted 1:30	6%	97 ±0.42955

Table 4.3 : The results for the size distribution σ and the NP radius rNP

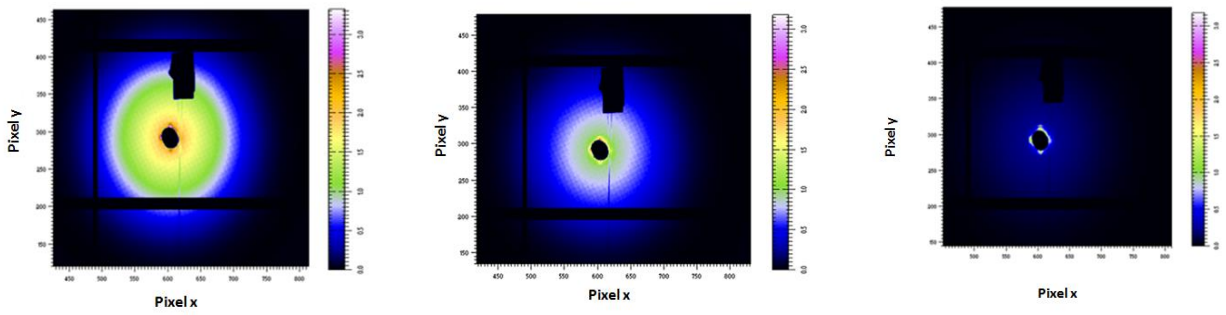

a) 1:3 **b) 1:10** **c) 1:30.**

Figure 4.14: Detector image measured on samples of different concentrations.

4.6 GISAXS

Ordered arrays of nanoparticles are useful for several applications in nanoparticle-based devices. The formation of arrays of magnetic nanoparticles depends on interaction between the particles like van der Waals, sterical repulsion and magnetic dipole-dipole interaction which were discussed in section 2.4. The final configuration depends also on the type and thickness of the surface layer. In this work, we report on the ordering of 2-D arrays of iron oxide nanoparticles deposited on pre-structured silicon substrates. For monolayers, the SEM observations were followed by GISAXS to analyze the large area ordering of nanoparticles.

The GISAXS measurements were carried out at FZ Jülich using GALAXI instrument with a mono-chromized X-ray beam(0.7×0.7 mm), with wavelength of 1.3414 A°, and the first chamber of the collimation stage containing the slit system and attenuator, with slits distance of 4m. The sample detector distance was set to 3537 mm. The diffusely scattered intensity from the iron-oxide nanoparticles was measured by a position sensitive detector of 172 pixels. From the scans, the reciprocal space maps were obtained. Monolayer samples were prepared by depositing iron oxide onto pre-structured silicon substrates.

To compare the intensity between pre and none pre-structured silicon wafers we made a slice (figure 4.21) with incident angle $\alpha i = 0.2^{\circ}$ through the specular reflects with width 10 pixels. It is clear from figure 4.21 that the position of peaks give approximately $\approx 0.33\ \mathrm{nm}^{-1}$ for both of substrates, which corresponds to the period between stripes and the distance between the nanoparticles $\mathrm{L} = \frac{2\pi}{\Delta q} \approx 19\ \mathrm{nm}$.

From the intensity ratios we can get the degree of order. There is a hexagonal ordering on the surface and along the depth. The intensity of pre-structured approximately has the same intensity of non-pre-structured. That means the channels did not have any effect on the ordering of nanoparticles, and there no correlations can be established.

Figure 4.15 shows the 2D GISAXS pattern measured at different incident angles and constant ξ angle, which define the plane rotation of the sample, obtained for the pre-structured silicon wafers, while figure 4.16 shows the 2D GISAXS pattern for the pre-structured silicon wafers measured at constant incident angle $\alpha i = 0.2^{\circ}$ and different ξ angles. The GISAXS patterns in both figure contains some diffraction spots.

Taking into account the diffraction spots due to the presence of the two x-rays beam, i.e. the transmitted and reflected beams the ring crosses the specular reflection and the primary beam corresponds to the scattering from Si gratings with rectangular shape. The reflected part contains off-specular scattering peak of the first order from the lateral correlation. The transmitted part also contains some information.

Figure 4.17 shows GISAXS patterns obtained for an 20 nm iron oxide nanoparticles deposited on a pre-structured wafers for different incident angles and fixed ξ angle. The Nanoparticles were drop-casted onto the pre-structured wafers.

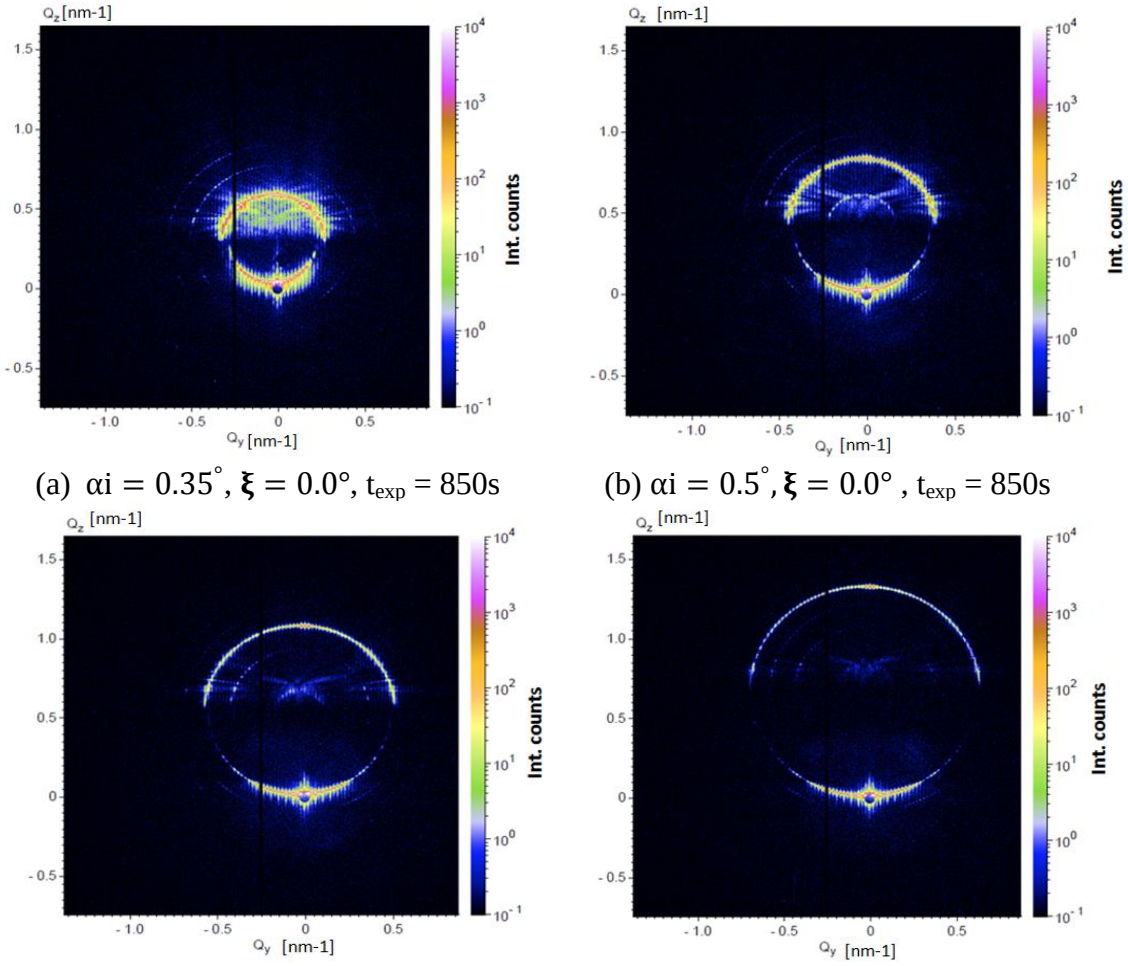

(a) $\alpha i = 0.35^{\circ}, \xi = 0.0°, t_{exp} = 850s$ (b) $\alpha i = 0.5^{\circ}, \xi = 0.0°, t_{exp} = 850s$

(c) $\alpha i = 0.65^{\circ}, \xi = 0.0°, t_{exp} = 850s$ (d) $\alpha i = 0.8^{\circ}, \xi = 0.0°, t_{exp} = 850s$

Figure 4.15: GISAXS patterns measured at different incident angles αi and constant ξ angle, which define the plane rotation of the sample for a pre-structured Si wafer without nanoparticles. $\delta = 0.05$. The gratings period is 300nm and the depth is 100nm. The ring, which crosses the specular reflection and the primary beam, corresponds to the scattering from Si gratings.

At $\alpha i = 0.0°$, the intensity is poor. At $\alpha i = 0.2°$ the penetration depth of the beam significantly increases and the beam intensity increases and the diffracted beam grows also. At $\alpha i = 0.65°$ another peak appears (Yonda peak). By increasing the incident angle we split the two scattering process due to the transmitted and reflected beams. The reflected part becomes intensity decreased and for higher incident angles, it got weaker.

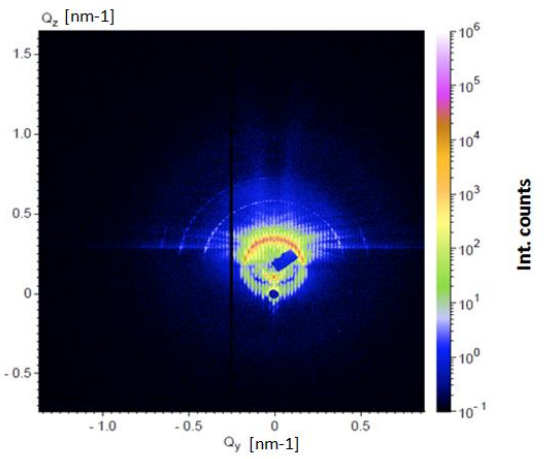

(a) $\alpha i = 0.2°,\ \xi = 0.01°, t_{exp} = 500s$

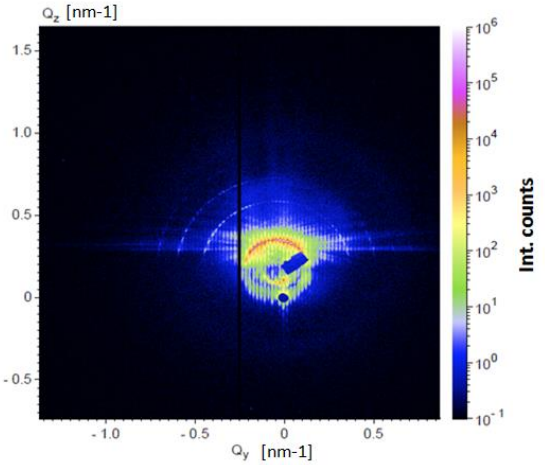

(b) $\alpha i = 0.2°,\ \xi = 0.06°, t_{exp} = 500s$

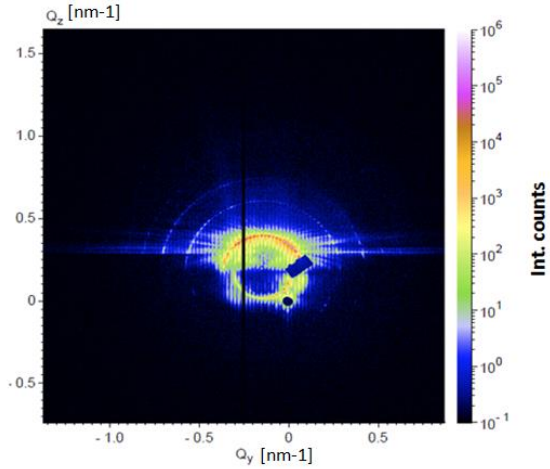

(c) $\alpha i = 0.2°,\ \xi = 0.18°, t_{exp} = 500s$

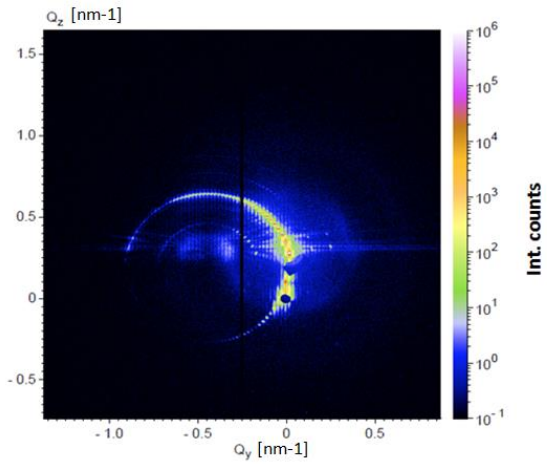

(d) $\alpha i = 0.2°,\ \xi = 0.50°, t_{exp} = 500s$

Figure 4.16: (a, b, c, d) GISAXS pattern of a pre-structured Si wafer without nanoparticles, measured at fixed incident angle $\alpha i = 0.2°$ and variable ξ angles. $\delta = 0.0$. Exposure time is500s. The gratings period is 300nm and depth is 100nm. The ring, which crosses the specular reflection and the primary beam, corresponds to the scattering from Si gratings.

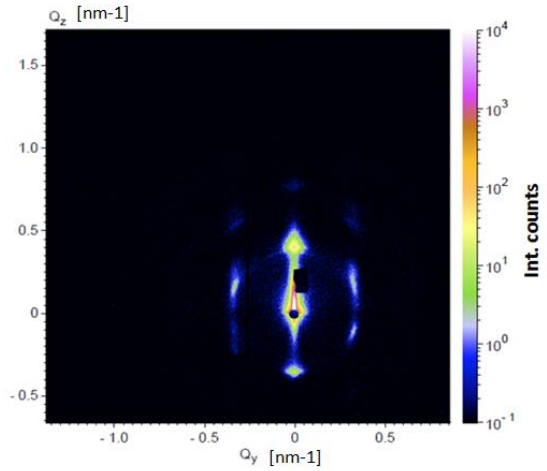

(a) $\alpha i = 0.0°,\ \xi = 0.0^{\circ}\ \ t_{exp} = 1030s$

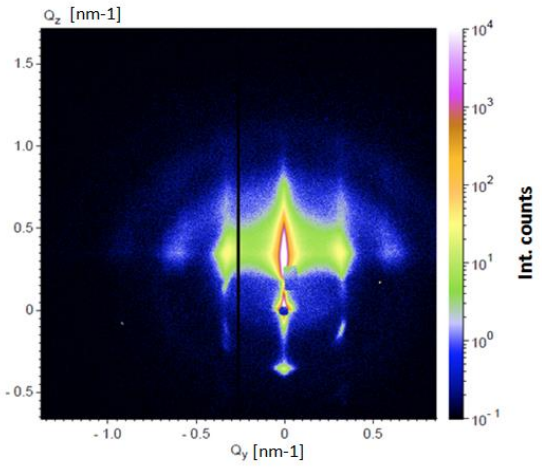

(b) $\alpha i = 0.2°\ ,\ \xi = 0.0^{\circ}\ \ t_{exp} = 1030s$

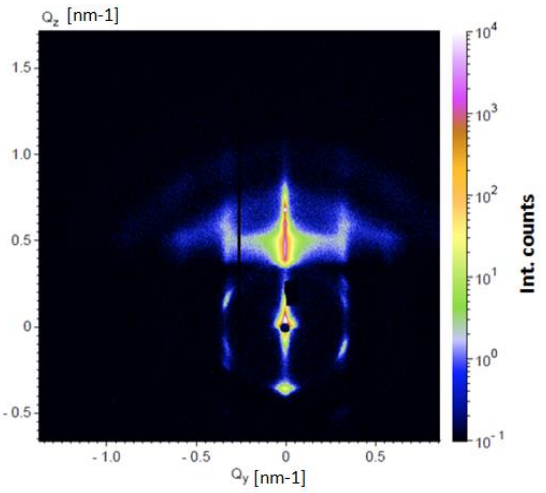

(c) $\alpha i = 0.4°\ , \xi = 0.0^{\circ}, t_{exp} = 1030s$

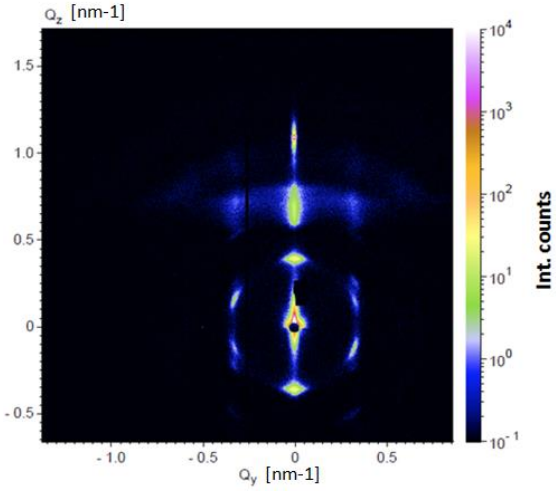

(d) $\alpha i = 0.65°\ , \xi = 0.0^{\circ}, t_{exp} = 1030s$

Figure 4.17: GISAXS patterns measured at different incident angles and constant ξ angle, which define the plane rotation of the sample for a 20 nm iron oxide deposited on a non- pre-structured Si wafer. $\delta = 0.05$. The gratings period is 300 nm. Time of each exposure is 1030s.

Figure 4.18 shows GISAXS patterns for a 20 nm iron oxide nanoparticles deposited on a pre-structured silicon wafers at different incident angles and constant ξ angle. Where the incoming beam was parallel to the stripes of the silicon wafers. Figure 4.19 shows GISAXS patterns for the same sample of figure 4.18, with the incoming beam perpendicular to the channels of the wafers. At $\alpha i = 0.0°$, the scattering process occurred due to the reflected beam only in contrast to the parallel case. At $\alpha i = 0.15°$ and $\alpha i = 0.4°$, the incoming beam for the parallel case was higher than the incoming beam intensity for perpendicular case. For

$\alpha i = 0.5°$ the diffracted spots showed that incoming beam parallel case is clearer (approximately ring) than the spots of the incoming beam perpendicular case.

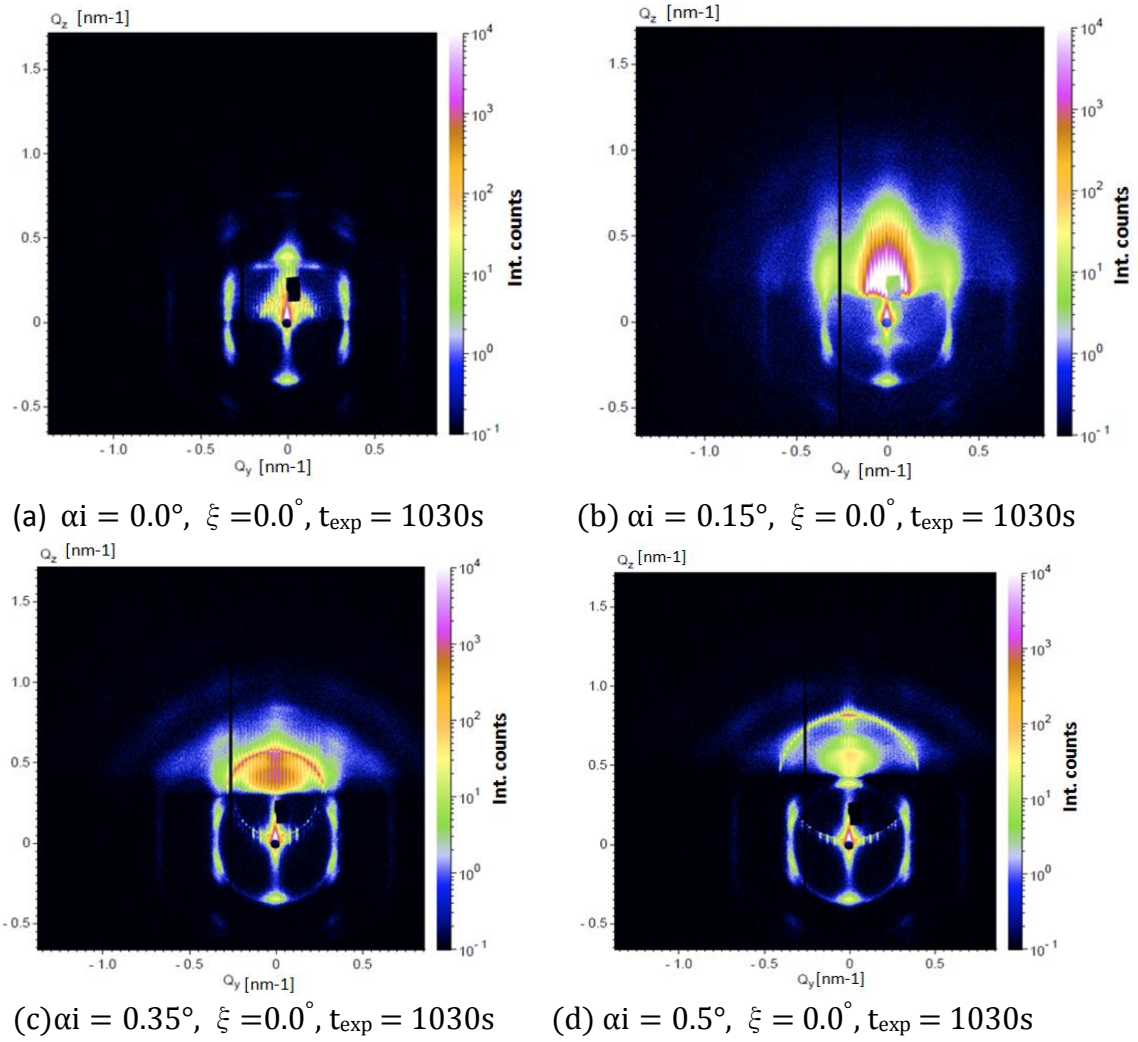

(a) $\alpha i = 0.0°,\ \xi = 0.0^{\circ}, t_{exp} = 1030s$ (b) $\alpha i = 0.15°,\ \xi = 0.0^{\circ}, t_{exp} = 1030s$

(c) $\alpha i = 0.35°,\ \xi = 0.0^{\circ}, t_{exp} = 1030s$ (d) $\alpha i = 0.5°,\ \xi = 0.0^{\circ}, t_{exp} = 1030s$

Figure 4.18: (a, b, c, d)GISAXS patterns for an 20 nm iron oxide nanoparticles deposited on a pre-structured Si wafer ,measured at different incident angles and constant ξ angle which define the in-plane rotation of the sample. time of each exposure is 1030s. $\delta = 0.05$. The incoming beam parallel to the stripes.

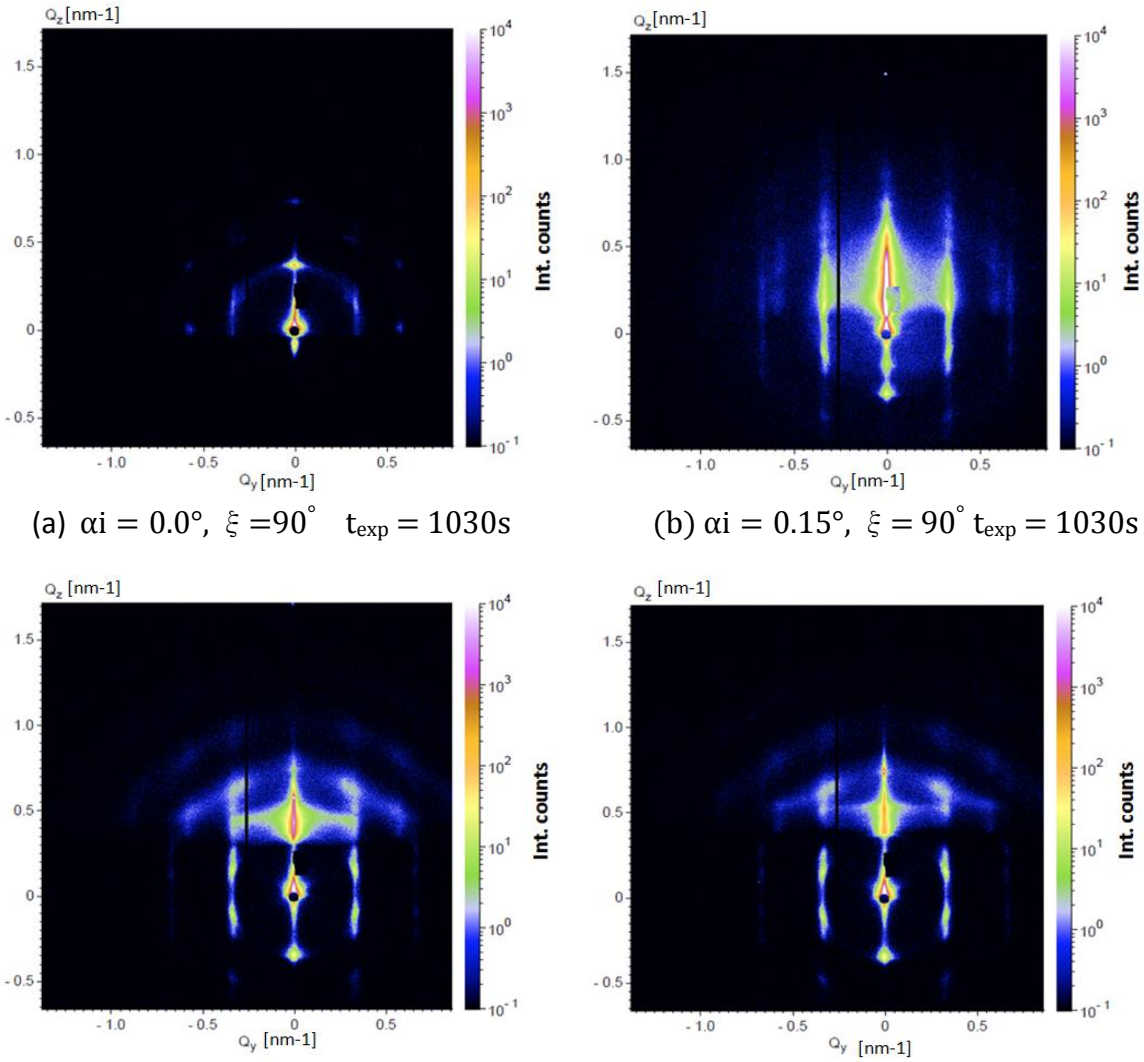

(a) $\alpha i = 0.0°$, $\xi = 90^{\circ}$ $t_{exp} = 1030s$ (b) $\alpha i = 0.15°$, $\xi = 90^{\circ}$ $t_{exp} = 1030s$

(c) $\alpha i = 0.4°$, $\xi = 90^{\circ}$, $t_{exp} = 1030s$ (d) $\alpha i = 0.5°$, $\xi = 90^{\circ}$ $t_{exp} = 1030s$

Figure 4.19 : (a, b, c, d)GISAXS patterns for an 20 nm iron oxide nanoparticles deposited on a pre-structured Si wafer ,measured at different incident angle*s* and constant $\xi = 90^{\circ}$ angle which define the in-plane rotation of the sample. time of each exposure is 206s. $\delta = 0.05$. The incoming beam perpendicular to the stripes.

Figure 4.20 shows patterns for 20 nm iron oxide drop-casted on a pre-structured silicon wafers. Measurement were made at $\alpha i = 0.3°$ incident angle, and the sample was slightly rotated in the plane. Exposure time was 1030 s and the ring corresponding to Si gratings significantly moves for small ξ . The rotation takes place around the z-axis of the sample.

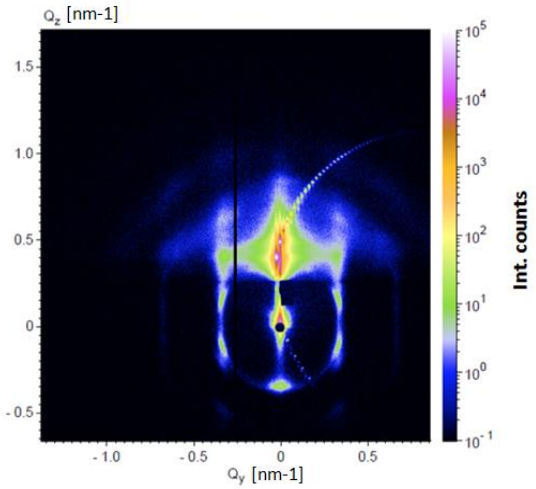

(a) $\alpha i = 0.3°,\ \xi = -1.05°,\ t_{exp} = 1030s$

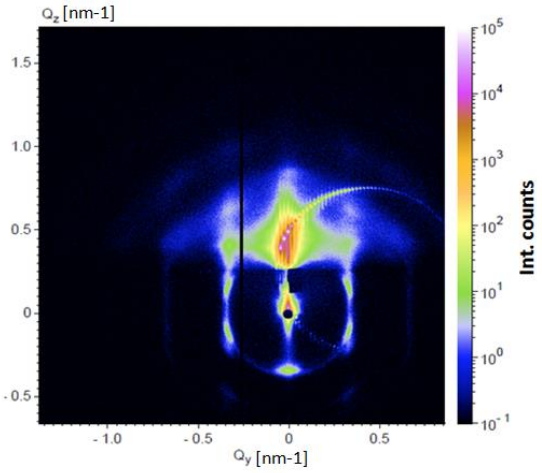

(b) $\alpha i = 0.3°,\ \xi = -0.55°, t_{exp} = 1030s$

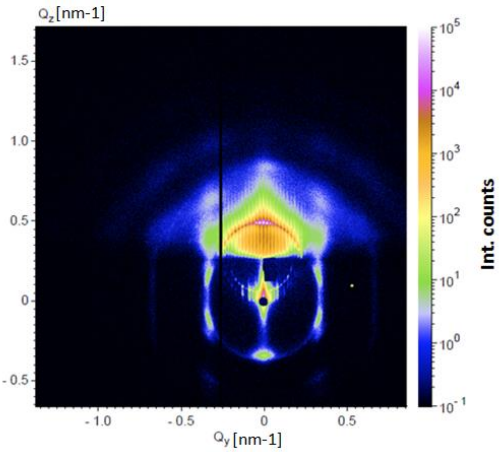

(c) $\alpha i = 0.3°,\ \xi = 0.0°, texp = 1030\ s$

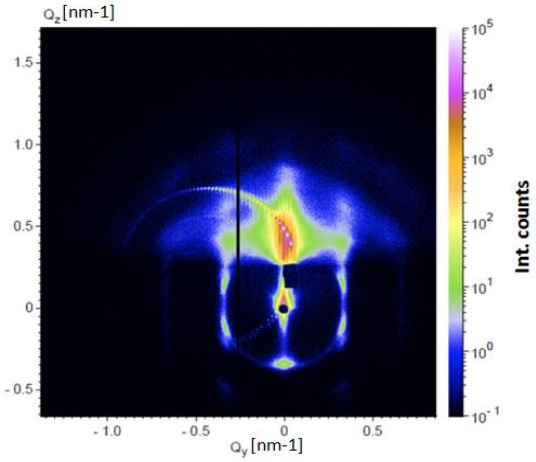

(d) $\alpha i = 0.3°,\ \xi = -0.5°, t_{exp} = 1030s$

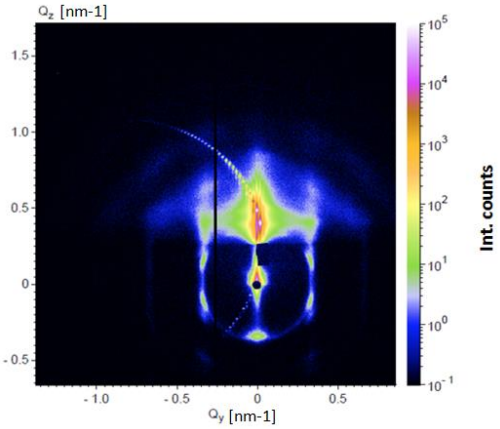

(e) $\alpha i = 0.3°,\ \xi = 0.95°, t_{exp} = 1030s$

Figure 4.20 : (a, b, c, d) GISAXS pattern of an 20 nm iron oxide nanoparticles deposited on a pre-structured Si wafer, measured at constant incident angles $\alpha i = 0.3°$ and different ξ angles. $\delta = 0.05$. Time of each exposure is 1030s. The period of the gratings is 300nm and depth is 100nm. The ring, which crosses the specular reflection and the primary beam, corresponds to the scattering from Si gratings. The spots correspond to the ordering of nanoparticles.

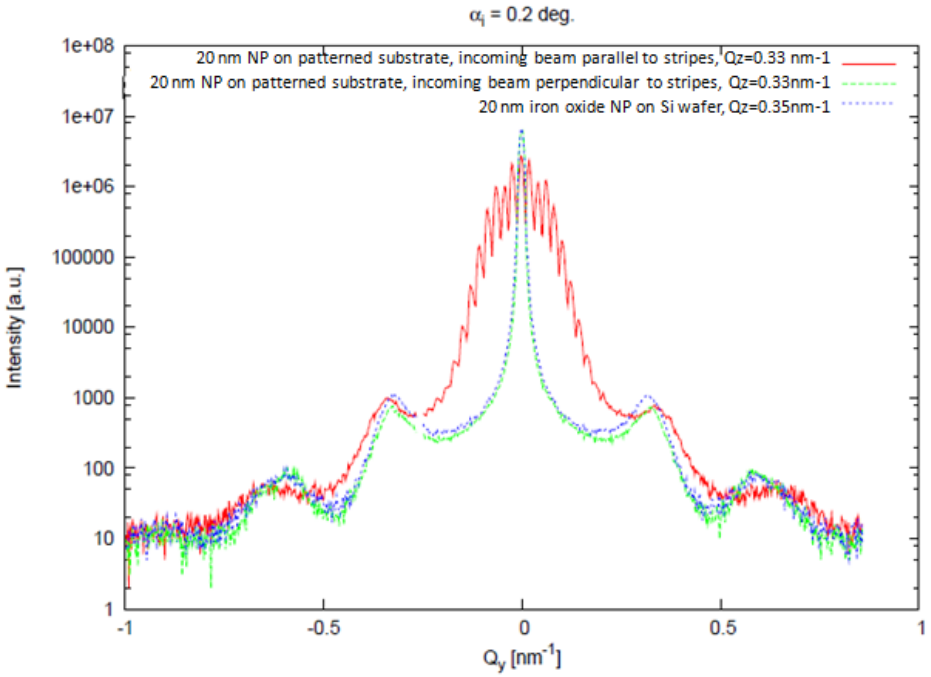

Figure 4.21: The slice from the GISAXS pattern (αi = 0.2˚). Position of peaks give Δq = 0.33 nm^{-1} which correspond to the period between stripes and the distance between the nanoparticles L= 2π/Δq =19 nm.

4.7 Self-Assembly of nanoparticles guided by faceted surface*

Although assemblies of nanoparticles with long-range order can lead to a new family of materials with tunable collective properties for a wide range of applications including Nano electronics, plasmon-enhanced solar cell, plasmonic wave guides, photonic crystals and memory storage, it is still a big challenge to produce long ranged ordered arrays of nanoparticles. Topographic surface patterns can be used to guide the self-assembly of nanoparticles. In addition, a reconstruction of a single crystalline wafers with nanoscopic surface facets (Sapphire) to guide the self-assembly of nanoparticles can be used. This is attractive because the large single-crystalline wafers of sapphire with well-defined orientation are commercially available.

Sapphire

Sapphire is an oxide mineral, consisting of Aluminum and an oxide with the chemical formula (α-Al_2O_3). It has a hexagonal close packed crystal structure with lattice parameters (a=4.785A˚, C=12.991A˚) as shown in figure 4.22/ It and belong to the R-3C space group.

The four planes of Sapphire are: i) C-plane (0001), ii) M-plane (1010), iii) A-plane (1120), iv) R-plane (1102) (figure 4.22-a).

Material:	**Al2O3**
Orientation:	**(1010)K**
Size:	**dia. 2 inch**
Thickness:	**430 µm**
Polishing:	**1 side epi pol.**
Quantity:	**5 pcs.**
Price:	**78,00 €/pc.**

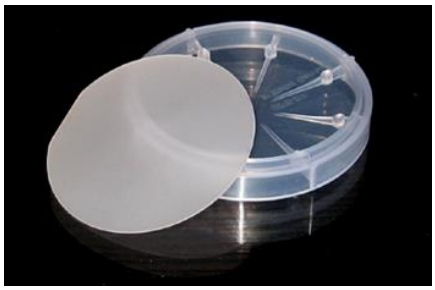

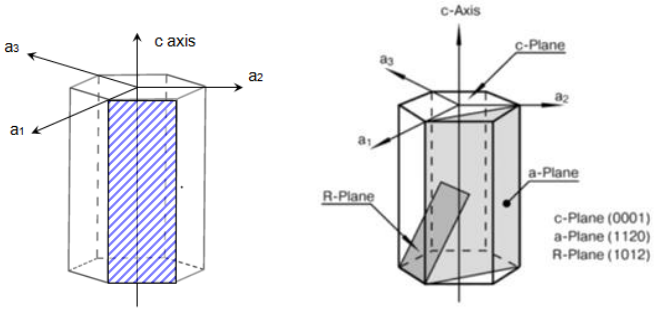

a)

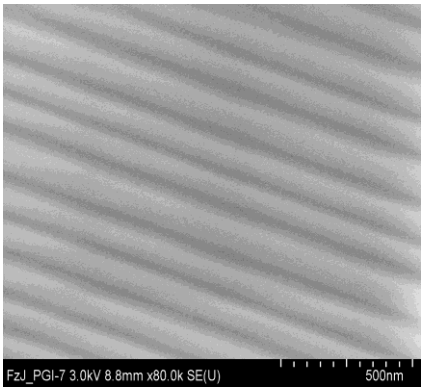

b)

Figure 4.22: a) Crystal structures and the planes of sapphire, b) SEM image of sapphire.

Fabrication of patterned sapphire substrate

The facets were produced at the lab by thermally annealing the single crystal surface of sapphire, cut a- long the M-plane (1010). The flat surfaces of M-plane sapphire can reconstruct into facets with (1101) and (1102) crystal planes as shown in figure 4.23.

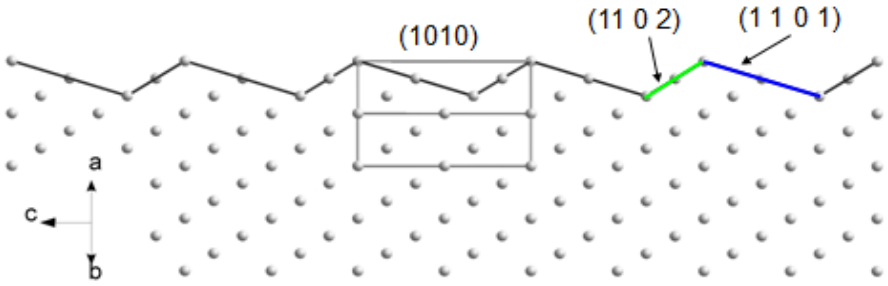

Figure 4.23: Surface reconstruction of sapphire upon annealing.

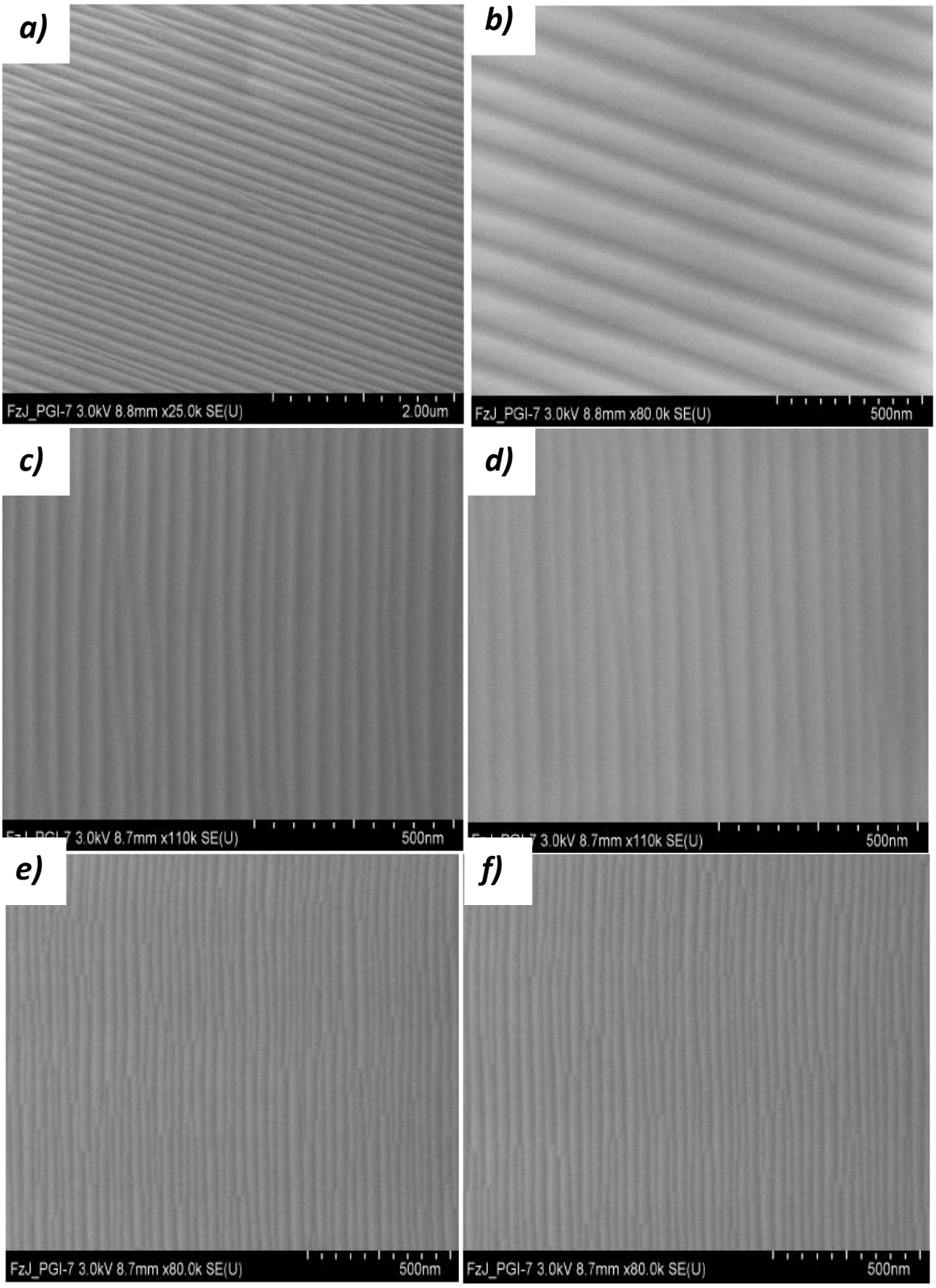

Figure 4.24: SEM image for Sapphire substrate after heat-treatment. a-b) on 1500°C for 24 h . c-d) on 1400°C for 24 h. e-f)on 1300°C for 24 h.

Sawtooth pattern can be generated on the surface. The M-plane sapphire surfaces were heated to temperatures from 1300 C° to 1500 C° and annealed for 24 hour with pitch of saw tooth that was varied from 24 to 160 nm and the amplitudes ranged from 3 to 20 nm. Figure 4.24 shows the SEM images of sapphire substrates that were heat-treated at different temperatures. The number of the channels was highest when the sapphire substrates were treated at the lowest possible temperature (figure 4.24 c-f), and the number decreased when the sapphire was heat treated at larger temperatures. This is shown in figure 4.24 a-b.

Sample

The nanoparticles chosen for this part were iron (Fe) cubic shaped with a diameters of about 30 nm (figure 4.25). They were dispersed in Hexane and coated with oleic acid.

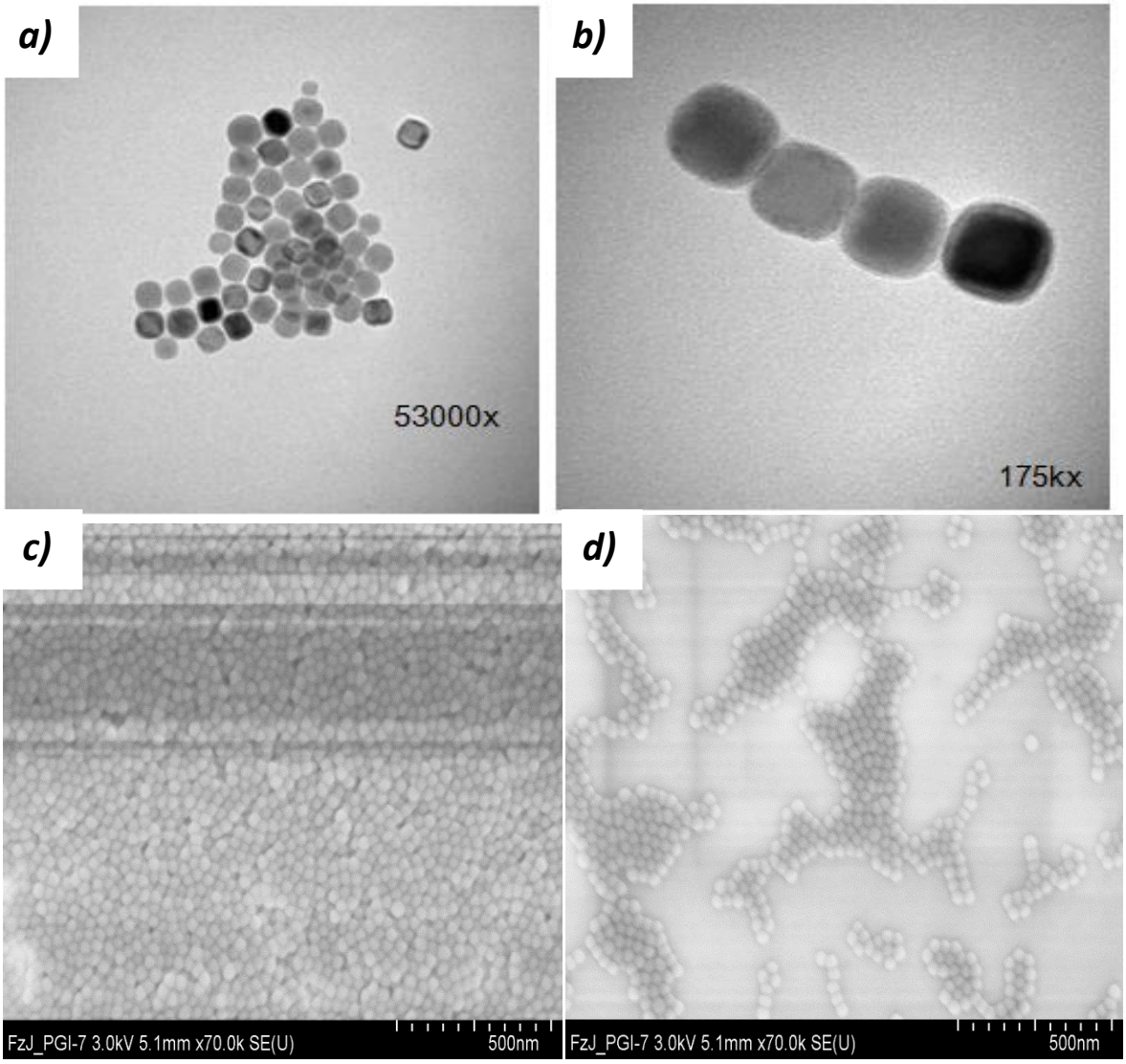

Figure 4.25: a-b) TEM image of iron nanoparticles, c-d) SEM image of iron nanoparticles.

Finely powdered iron has long been known to be pyrophoric, which is a major reason that iron nanoparticles have not been more fully studied to date **[Hanaor et al, 2011]**. Iron nanoparticles are highly reactive because of their large surface area. They can be synthesized by the reduction of Fe(II) or Fe (III) salt with sodium borohydride in an aqueous medium.

$$Fe(H_2O)6^{+3} + 3BH_4 + 3H_2O \rightarrow Fe^{\circ} + 3B(OH)3 + 10.5H_2$$

SAXS by iron nanoparticles

For SAXS measurements, the iron nanoparticles in Hexane solvent (C_6H_{14}) were filled into Hilgenberg quartz capillary with inner diameter 1.5 mm and a well thickness of 0.01 mm. The capillary was closed with PMMA stopper using Loctite 408 glue and a sphere of silicon above the slot of the capillary. SAXS measurements were performed with a fixed incoming wavelength of CuKα with wavelength λ = 1.3414 A°. Data reduction and fitting was performed by using the SasView **[SasView, 2012]**.

Figure 4.26 present the reduced and normalized SAXS data in absolute units by iron nanoparticles. The data matching with a spherical form factor leads to an approximate particle radius r and size distribution σ as listed below.

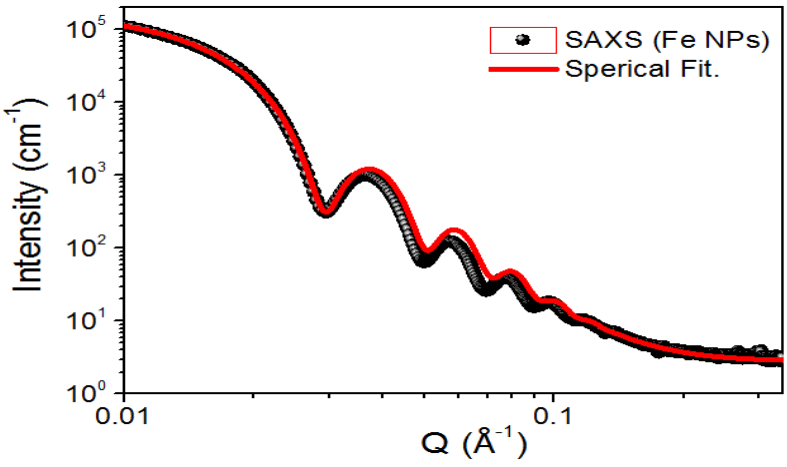

Figure 4.26: SAXS by Fe nanoparticles and characterization of NP without substrate.

SEM results*

The iron nanoparticles were deposited on a home patterned sapphire substrate using spin-coating method; and the pull substrate out from solvent slowly. Results of the deposition of iron nanoparticles by a pull a patterned substrate, showed reasonably ordered arrays (figure 4.27 a). The spin coating at a spinning speed 30rpm for 5s, did not show ordering as clear.

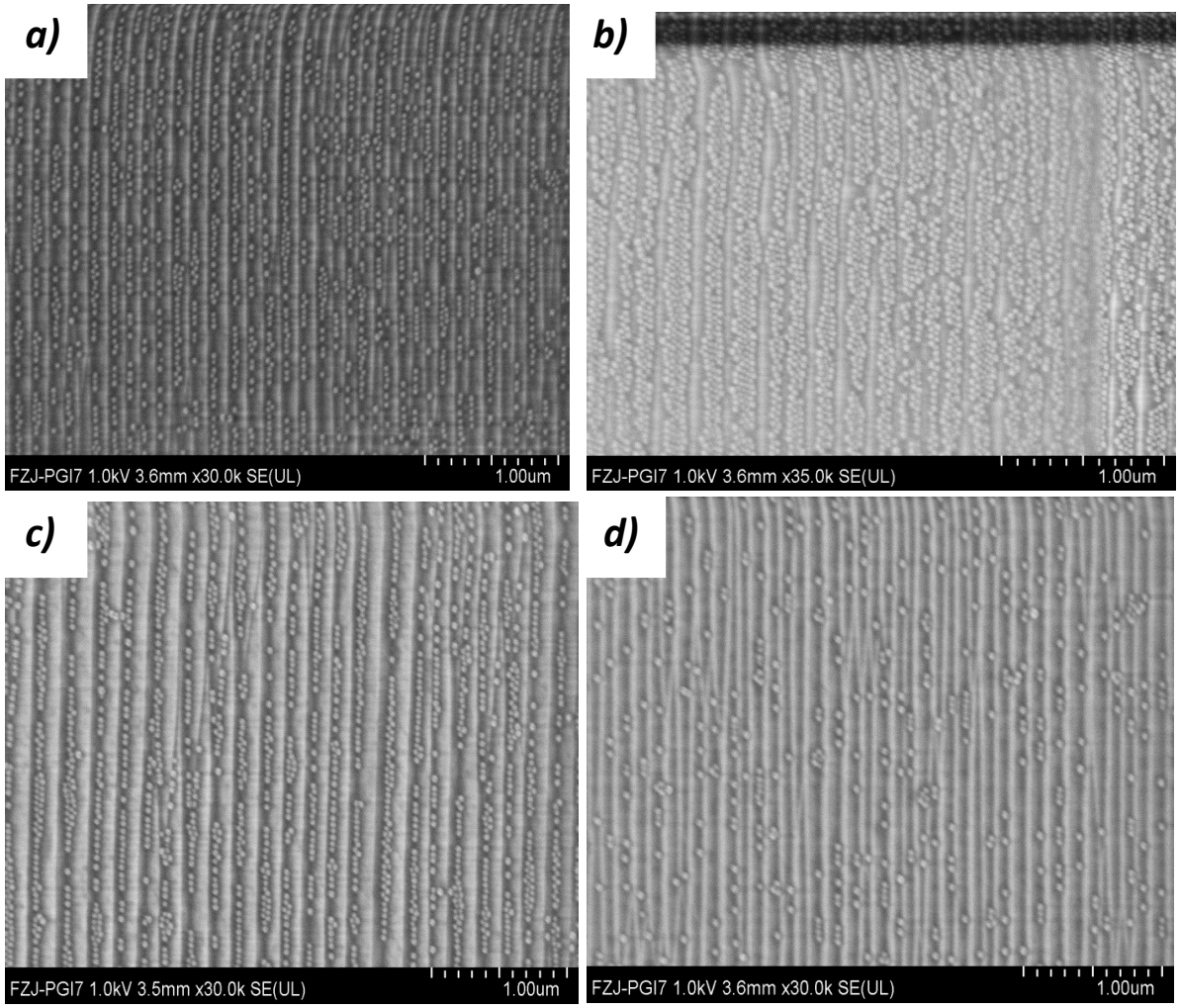

Figure 4.27: SEM image of Fe nanoparticles on patterned sapphire substrate. a) Fe nanoparticles in Hexane pull out slow. b) Fe nanoparticles in Hexane spin coating 30rps 5s. c) Fe nanoparticles in Hexane 1:2 diluted spin coating 30rps 5s. d) Iron nanoparticles in Hexane diluted 1:3 spin coating 30rpm for 5s.

*This part of work was conducted in cooperation with the principal investigator of this part Dr. Yinguo Xiao from the scientific staff at JCNS-2, PGI-4: scattering Methods.

Chapter 5 Summary & Outlook

Both the assembly and ordering of nanoparticles were studied in this work. Commercially an available iron oxide nanoparticles, supplied by Ocean Nanotech LLC, with diameter of approximately 20 nm and spherical shape were studied. These nanoparticles were delivered with an oleic acid shell and dispersed in toluene.

Iron oxide was transferred onto silicon wafers (pre-structured, none pre-structured) by two methods: drop casting and spin coating. The order of nanoparticles using drop casting on pre-structured substrates showed better results compared to the spin coating method. Alternatively, the spin coating on non-pre-structured substrates provided a smooth, sub homogeneous surface, and the film thickness was easily controllable by spinning speed and duration.

The iron oxide was diluted with toluene in different proportions. The best results were achieved for the 1:10 ratio. Therefore that sample was used for all subsequent samples.

To allow the nanoparticles to interact the oleic acid shell had to be removed by oxygen plasma. The samples were treated for 5 min at a pressure of approximately 0.7 mbar. The samples were characterized by high-resolution scanning electron microscopy (SEM), small angle X-ray scattering (SAXS), and grazing incidence small angle X-ray scattering (GISAXS).

The size and size distribution were investigated by the SEM. The local order on the sample surface was confirmed to be 2d structure. Using SAXS, the 3d structure was determined , also, size and size distribution were investigated, and it is consistent with the SEM data. By using GISAXS measurements, there are no correlations between stripes and ordering nanoparticles.

Iron nanoparticles, with diameter of approximately 30 nm, cubic shape, and dispersed in Hexane were deposited in the patterned sapphire with a lattice constant (a=4.785 **A**$^{\circ}$). The sapphire was cut into pieces with size 6×8 mm, and heated to a very high temperature from 1300 to 1500 **c**$^{\circ}$ for 24 h. the best stripes when heated to 1300**c**$^{\circ}$. Size and size distribution

determined for iron nanoparticles by SAXS measurement. Different deposition routes were used to deposit iron nanoparticles in patterned sapphire: spin coating and pull a patterned sapphire out from solvent slowly. The later gives approximately best ordered arrays of nanoparticles.

In the near future, the assisted self-assembly of magnetic nanoparticles in order to obtain highly ordered arrangements investigated with GALAXI instrument will be characterized by scanning electron microscopy and small x-ray scattering under grazing incidence, and then investigate their magnetic properties and interactions will be studied with a SQUID or MOKE magnetometer and eventually with polarized neutron scattering using MARIA or KWS reflectometer at MLZ in Munich. In addition, this study covers topics preparation of lithography Nano templates to obtain the pre-structured substrate using self-organized di-block copolymers to scattering methods for investigation of prepared sample.

Bibliography

[Abrikosov et al, 1963-1975]. A. A. Abrikosov, L.P. Gorkov, and I.E. Dzyaloshinsky. *Methods of Quantum Field Theory in Statistical Physics.* Dover Publications. ISBN 0-486-63228-8. (1963–1975). Chapter 6 Electromagnetic Radiation in an Absorbing Medium.

[Askeland et al, 2010]. D. R. Askeland, P. P. Fulay and W. J. Wright. *The Science & Engineering of Materials*, USA: Cenage Learning Inc, (2010).

[Balamurugan et al, 2012]. B . Balamurugan, D . J. Sellmyer, G . C . Hadjipanayis, and R. Skomski. Scripta Mater. 67 542.(2012).

[Becker, 2009]. G. Becker. *Introduction to nanotechnology*, Germany: Lecture notes (Universität of Duisburg-Essen), of (2009).

[Beegan et al, 1997]. R. D. Beegan, O. Bakajin, T. F. Dupont, G. Huber, S. R. Nagel and T. A. Witten. *Capillary flow as the cause of ring stains from dried liquid drops*, Nature, vol. 389, pp. 827-829, (1997).

[Bigioni, 2006]. T. P. Bigioni, X. M. Lin, T. T. Nguyen, E. I. Corwin, T. A. Witten and H. M. Jaeger. *Kinetically driven self assembly of highly ordered nanoparticle monolayers*, Nature Materials, vol. 5, pp. 265-270, (2006).

[Binasch, 1989]. G. Binasch, P. Grunberg, F. Saurenbach and W. Zinn. *Enhanced magneto resistance in layered magnetic structures with antiferromagnetic interlayer exchange*, Physical Review B, vol. 39, pp. 4828-4830, (1989).

[Biosaxs, 2013]. [Online; accessed 20-Oct-2015]. RUL :*http://biosaxs.com/technique.html.*

[Bishop et al, 2009]. K. J. M. Bishop, C. E. Wilmer, S. Soh and B. A. Grzybowski. *Nanoscale Forces and Their Uses in Self-Assembly*, small, vol. 5, pp. 1600-1630, (2009).

[Blundell, 2007]. S . Blundell. *Magnetism in condensed matter* . Oxford university press , (2007).

[Butt, Kappl, 2010]. H. J. Butt and M. Kappl. *Surface and Interfacial Forces*, Germany: Wiley, (2010).

[Ce et al, 2014]. Y . Ce, H . Y . Long, and G . Song. *Nanomagnetism: principles, nanostructures, and diomedical applications*. Chin. phys. B , vol.23, No.5(2014)057505. Pub. 15 April (2014).

[Chatterjee et al, 2012]. P. Chatterjee, S. Hazra and H. Amenitsch: *Substrate and drying effect in shape and ordering of micelles inside CTAB-silica mesostructured films*, Soft Matter 8, 2956, (2012).

[Coey, 2001]. J. M. D. Coey. *Magnetism in future, Journal of Magnetism and Magnetic Materials*, Vols. 226-230, pp. 2107-2112, (2001).

[Colina, Acker, 2000].H. Colina and P. Acker, Drying cracks: *Kinematics and scale laws, Materials and Structures*, pp. 101-107, (2000).

[Cornell, Schwertmann, 2003]. R. M. Cornell and U. Schwertmann. *The Iron Oxides: Structure, Properties, Reactions, Occurences and Uses*, Germany: Wiley, (2003).

[Cudennec, Lecerf, 2005]. Y. Cudennec and A. Lecerf. *Topotactic transformations of goethite and lepidocrocite into hematite and Maghemite*, Solid State Sciences, vol. 7, pp. 520-529, (2005).

[Debye, 1921]. P. Debye. *Molecular forces and their electrical interpretation*. Physical Journal (1921), 22, 302-308.

[Disch, 2010]. S. Disch , Structural *The spin structure of magnetic nanoparticles*

and in magnetic nanostructures, Germany: PhD Thesis (RWTH Aachen University), (2010).

[Dipolar interaction, 2015]. [Online; accessed 15-Oct-2015]. RUL: *http://userpage.chemie.fu-berlin.de/~tolstoy/chapter3.pdf.*

[Doniach, 1987]. S. Doniach, P. J. Hirschfeld, M. Inui, A. E. Ruckenstein. *Novel Superconductivity*. Pages. 395-399. Springer US. (1987).

[Dormann, 1997]. J . L . Dormann, D. Fiorani, and E.Tronc. Adv. Chem. Phys. 98 283.(1997).

[Dronskowski, 2001]. R. Dronskowski. *The little maghemite story: A classic functional material*, Adv. Funct. Mater. 11, 27, (2001). [Online; accessed 15-Oct-2015].RUL: *http://onlinelibrary.wiley.com/doi/10.1002/chin.200125209/abstract.*

[Dunlop, Özdemir, 1997]. D . J . Dunlop and Ö . Özdemir . *Rock magnetism* (chapter 3). (1997).

[Dzyaloshinsky, 1957]. Dzyaloshinsky. *A thermodynamic theory of "weak" ferromagnetism of*

antiferromagnetics, Journal of Physics and Chemistry of Solids, vol. 4, pp. 241-255, (1957).

[Fowler, 1997]. M. Fowler. *Historical Beginnings of theories of electricity and magnetism*. Retrieved 2008-04-02. (1997).

[Friak et al, 2007]. M. Friak, A. Schindlmayr und M. Scheffler. *Ab initio study of the half-metal to metal transition in strained magnetite*, New Journal for Physics, Bd. 9, (2007).

[Gale Group, 2000]. *Magnetism*. [Online; accessed 29-Nov-2015]. Gale Group. RUL: *http://www.ucl.ac.uk/EarthSci/people/lidunka/GEOL2014/Geophysics9%20-Magnetism/Useful%20papers/Magnetism.htm*. Farmington Hills , Mish, (2000).

[GALAXI, 2002]. *GALAXI.* **[**Online; accessed 18-ONov-2015](2002). RUL: ***https://www.bruker.com.***

[Gepas et al, 2002]. O . Gepas , T . Sakai, and T. Ziman, *Dynamics, selection rules and Dzyaloshinsky-Moriya interactions in strongly frustrated magnet*, progress of theoretical physics supplement , No. 145, (2002).

[Gibaud et al, 2003]. A. Gibaud, D. Grosso, B. Smarsly, A. Baptiste, J. F. Bardeau, F. Babonneau, D. A. Doshi, Z. Chen, C. Jeffrey Brinker, and C. Sanchez: *Evaporation-Controlled Self-Assembly of Silica Surfactant Mesophases*, J. Phys. Chem. B 107, 6114-6118 ,(2003).

[Gilbert, 1600]. W. Gilbert. *De Magnete*, UK, (1600).

[Glatter, Kratky, 1982]. O. Glatter,O. Kratky. *Small Angle X-ray Scattering*. Academic Press. ISBN 0-12-286280-5., eds. (1982).

[Goll, 2004]. D . Goll, A . E . Berkowitz, and H . N . Bertram .(2004) Phys. Rev. B 18 184432.

[Goya et al, 2005]. G . F Goya, M . Veith, R . Rapalavicuite, H . Shen and S . Mathur. *Thermal hysteresis of spin reorientation at Morin transition in alkoxide derived hematite nanoparticles*, Appl . Phys . 1523 - 1526 ,(2005).

[Gubin, 2009]. S. P. Gubin (Ed.). *Magnetic Nanoparticles*, Germany: WILEY-VCH, (2009).

[Guimarães, 2009]. A . P. Guimarães. *Principles of Nanomagnetism*, (Berlin: Springer-Verlag), (2009).

[Hanaor et al, 2011]. D . A .H . Hanaor, G .Triani, and C . C . Sorrell. *Morphology and photocatalytic activity of highly oriented mixed phase titanium dioxide thin films.Surface and coatings technology* 205 (12): 3658–3664, (2011).

[Harrison, Borkowski, 2002]. R. J. Harrison, D . Borkowski. *Direct imaging of nanoscale magnetic interactions in minerals* . RE; Putnis. Proceedings of the National Academy of Sciences 99 (26): 16556–16561, (2002).

[Hazra et al, 2004]. S. Hazra, A. Gibaud and C. Sella: *Tunable absorption of Au-Al2O3 nanocermet thin films and its morphology*, Appl. Phys. Lett. 85, 395, (2004).

[Huber, 2005]. D . Huber. *Synthesis, properties, and application of iron nanoparticles*. Nanostructures and advanced materials chemistry dept. Sandia national laboratories, small. (2005) May, 1(5): 482-501.

[Hu, 2012]. C. D. Hu. *The Dzyaloshinskii-Moriya interaction in metals*, Journal of Physics: Condensed Matter, vol. 24, (2012).

[IFF Spring school, 2007]. 38th IFF Spring School 2007. *Probing the Nanoworld*, Forschungszentrum Jülich: (2007).

[Israelachvili, 1994]. J . Israelachvili . *Intermolecular and surface forces* (2nd edition). Academic press , London , (1994).

[Ito, 2009]. Y. Ito, *Grazing-incidence small-angle X-ray scattering technique for nanostructure determination of surfaces and interface of thin films*. Rigaku journal, (2009). [Online; accessed 25-Oct-2015]. RUL: ***http://www.rigaku.com/downloads/journal/RJ25-1/RJ25-1_1-6.pdf.***

[JRank, 2013]. *Capillary Action – Liquid, Water, Force, and Surface*– JRank Articles. Science.jrank.org. Retrieved (2013).

[Keesom, 1921]. W . Keesom . *Van der Waals attractive force*. Phys. Z (1921), 22, 129-141.

[Keesom, 1920]. W. Keesom . *The quadrupole moments of the oxygen and nitrogen molecules*. Proc. K. Ned. Akad. Wet in (1920), 23, 939-942.

[Kim et al, 2000]. J . Kim, K . Barmak, M.D .Graef, L . H. Lewis, and D. C. Crew.J. Appl. Phys. 87 6140.(2000).

[Kittel, 1991]. C . Killel. *Introduction to Solid State Physics*, 8th Edition. Wiley. p. 304, (1991).

[Kneller, Hawig, 1991]. E . F .Kneller, and R . Hawig .IEEE T. Magn. 27 3588.(1991).

[Knobel, 2008]. M . Knobel, W . C .Nunes, L . M .Socolovsky, E . D . Biasi, J . M .Vargas, and

J . C . Denardin. J. Nanosci. Nanotechno. 8 2836. (2008).

[Kugel et al, 1978]. G. E. Kugel, B. Hennion and C. Carabatos. *Low-energy magnetic excitations in wustite (Fe1- x O),* Physical Review B, vol. 18, pp. 1317-1321, (1978).

[Leite et al, 2012]. F . Leite, L. Bueno, C. C. Da Róz, A. L. Ziemath, and E. C. Oliveira, O. N. *Theoretical Models for Surface Forces and Adhesion and Their Measurement Using Atomic Force Microscopy*. International Journal of Molecular Sciences 13 (12): 12773.(2012).

[Levine et al, 1989]. J. R. Levine, J. B. Cohen, Y. W. Chung and P. Georgopoulos: *Grazing-incidence small-angle X-ray scattering: new tool for studying thin film growth* , J. Appl. Cryst. 22, 528-532,(1989).

[London, 1930]. F .London. *Properties and Applications of Molecular Forces*. Journal of Physical Chemistry (B) in (1930), 11, 222-251.

[Lu, Meng, 2010]. H. M. Lu and X. K. Meng. *Morin Temperature and Neel Temperature of Hematite Nanocrystals*, Journal of Physical Chemistry C, vol. 114, pp. 21291-21295, (2010).

[McCammon, Liu, 1984]. C. A. McCammon and L. Liu. *The Effects of Pressure and Temperature on nonstoichiometric Wustite, FexO: The Iron-rich Phase Boundary*, Physics and Chemistry of Minerals, vol. 10, pp. 106-113, (1984).

[Meiklejohn, Bean, 1956]. W . H .Meiklejohn, and C.P. Bean .Phys. Rev. 102 1413.(1956).

[Metzger et al, 1998]. T. H. Metzger, I. Kegel, R. Paniago, A. Lorke, J. Peisl, J. Schulze, I. Eisele, P. Schittenhelm, and G. Abstreiter: *Shape, size, strain and correlations in quantum dot systems studied by grazing incidence X-ray scattering methods, Thin Solid Films* 336,1-8, (1998).

[Mindat, 2015]. [Online; accessed 15-Oct-2015]. RUL: *http://www.mindat.org/min-2533.html.*

[Mishra, 2012]. D. Mishra. *Structural and magnetic characterization of self-assembled magnetic nanoparticles*, Germany: PhD Thesis (Universität Bochum), (2012).

[Mishra et al, 2008]. D. Mishra, D. Greving, G. A. B. Confalonieri, J. Perlich, B. P. Z. H. Toperverg and O. Petracic. *Growth modes of nanoparticle superlattice thin films.*arXiv:1307.4693.(2008).

[Meyer, 2011]. A . Meyer *GISAXS*.(2011).[Online; accessed 20-Oct-2015]. RUL: ***http://www.gisaxs.de.***

[Mohallem et al, 2012]. N . D . S . Mohallem , J. B. Silva , G. L . T. Nascimento and V . L . Guimarães. *Study of multi functional nanocomposites formed by cobalt Ferrite Dispersed in a silica matrix prepared by sol . gel process*, (2012).

[Morrish, 1994]. A. H. Morrish. *Canted antiferromagnetism: hematite*, USA: World Scientific Publishing Co. Pte. Ltd, (1994).

[NANO, 2014]. Nano.Gov, National Nanotechnology Initiative. [Online; accessed 29-Oct-2015]

RUL: *http:// www.nano.gov / nanotech -101 / what / definition* ,(2014).

[Naudon, Brumberger, 1995]. A. Naudon and H. Brumberger (ed.): *Modern Aspects of Small-Angle Scattering*, (Kluwer Academic Publishers, Amsterdam, (1995), p. 191.

[Nelsen, McMorrow, 2011]. J . Als-Nelsen and D . McMorrow. *Elements if modern x-ray physics*, 2nd ed. John Wiely sons Ltd., London, (2011).

[Nogues et al, 2000]. J . Nogues, L. Morello, C . Leighton, M . R . Ibarra, and I . K . Schuller. Phys. Rev. B 61 R6455.(2000).

[Nogues, Schuller, 1999]. J. Nogues, and I. K. Schuller. J. Magn. Magn. Mater. 192 203.(1999).

[Opel, 2003]. M. Opel. *Magnetismus*, Germany: Vorlesungsmanuskript (TU Munchen), (2003).

[Pankhurst et al, 2003].Q. A. Pankhurst, J. Connolly, S. K. Jones and J. Dobson. *Applications of magnetic nanoparticles in biomedicine*, J. Phys. D: Appl. Phys. 36, R167, (2003).

[Petracic, 2010]. O. Petracic. *Superparamagnetic nanoparticle ensembles*, Super lattices and Microstructures, vol. 47, pp. 569-578, (2010).

[Renaud et al, 2003]. G. Renaud, R. Lazzari, C. Revenant, A. Barbier, M. Noblet, O. Ulrich, F. Leroy, J. Jupille, Y. Borensztein, C. R. Henry, J.P. Deville, F. Scheurer, J. Mane-Mane, and O. Fruchart: *Real-Time Monitoring of Growing Nanoparticles*, Science 300, 1416, (2003).

[Rücker et al, 2012]. *World's best laboratory X-ray diffractometer for GISAXS*. Poster. U. Rücker, E. Kentzinger, M. Hölzle, F. Gossen, K. Bussmann, Th. Brückel, Th. Leipold, H. Feilbach, R. Möller, M. Wagener, H. Kleines ,JCNS-2 – Scattering Methods, JCNS/PGI-TA – Technical Design Department , andZEA-2 – Electronic Systems.(2012).

[Sakar, 2015]. M. Sakar, S. Balakumar, P. Saravanan and S. Bharathkumar . *Compliments of confinements: substitution and dimension induced magnetic origin and band-bending mediated photocatalytic enhancements in Bi1−xDyxFeO3 particulate and fiber nanostructures*. Paper.(2015).

[SasView, 2012]. *SasView*.[Online; accessed 25-Nov-2015](2003). RUL: ***http://www.sasview.org.***

[Saunders et al, 2006]. A. E. Saunders, A. Ghezelbash, D.M. Smilgies, M. B. Sigman Jr., and B. A. Korgel: *Columnar Self-Assembly of Colloidal Nanodisks*, Nano Letters 6, 2959-2963, (2006).

[Scanning Electron Microscope, 2003]. *Scanning electron microscope*. [Online; accessed 1-Nov-2015](2003). RUL: ***https://www.purdue.edu.***

[Scriven, 1988]. L. E . Scriven. *Physics and applications of dip coating and spin coating*. MRS proceedings.(1988).

[Smilgies et al, 2002]. D.M. Smilgies, P. Busch, D. Posselt, and C. M. Papadakis: *Characterization of Polymer Thin Films with Small-Angle X-ray Scattering under Grazing Incidence (GISAXS),* Synchrotron Radiation News, Issue 15(5), p. 35-42, (2002).

[Stamm, 2008]. M . Stamm(ed) . *In: Polymer surfaces and interfaces* . chapter DOI: 10.1007/978-3-540-73864-0-2 , Springer (2008).

[Tannhauser, 1961]. D . S . Tannhauser. *Conductivity of iron oxides*, journal of physics and chemistry of soilds , vol. 23 , pages 25-34 , Received (1961).

[Teixeira et al, 2012]. A. P. C. Teixeira, J. C. Tristao, M. H. Araujo, L. C. A. Oliveira, F. C. C. Moura, J. D. Ardisson, C. C. Amorim and R. M. Lago. *Iron: a Versatile Element to Produce Materi-*

als for Environmental Applications, Journal of Brazilian Chemistry, vol. 23, no. 9, pp. 1579-1593, (2012).

[Whitesides, Grzybousk, 2000]. G . M. Whitesides and B . Grzybousk. *Self-assembly at all scales*. Sciences 295:2418 , (2000).

[Whitesides, Boncheva, 2002]. G . M. Whitesides and M . Boncheva. Beyond molecules. *Self-assembly of mesoscopic and macroscopic components* . PNAS , 99:4769 , (2002).

[Whitesides, 2005]. G . M . Whitesides , J . K . Kriebel, and B. T. Mayers. *Self-assembly and Nanostructured materials* , department of chemistry and chemical biology , Harvard university , Cambridge MA 02138.(2005).

[Wilbs, 2013]. G . Wilbs. *Magnetic properties of self-assembled nanomaterials*, Germany : Master thesis(Universität Duisburg), (2013).

[Wikipedia, 2015]. *Oleic acid.* [Online; accessed 21-Oct-2015].

RUL: https://en.wikipedia.org/wiki/Oleic_acid.

[Wu et al, 2008]. W. Wu, Q. He and C. Jiang. *Magnetic Iron Oxide Nanoparticles: Synthesis and Surface Functionalization Strategies*, Nanoscale Resolution Letters, vol. 3, pp. 397-415, (2008).

[Yang et al, 2011]. C . Yang, J . J .Wu, and Y . L . Hou. (2011) Chem. Commun. 47 5130.

[Yin et al, 2007]. M. Yin, Z. Chen, B. Deegan and S. O'Brien. *Wustite nanocrystals: Synthesis, structure and superlattice formation*, Journal of Materials Research, vol. 22, pp. 1987-1995, (2007).

[Yunker et al, 2011]. P. Y. Yunker, T. Still, M. A. Lohr and A. G. Yodh. *Suppression of the coffee-ring effect by shape-dependent capillary interactions*, Nature, vol. 476, pp. 308-3011, (2011).

[Zheng et al, 2004]. R . K . Zheng, G . H . Wen, K . K . Fung, and X . X . Zhang. Phys. Rev. B 69214431.(2004).

نظام تجمع جزيئات النانو بهياكل ثنائية وثلاثية الأبعاد أو مصفوفات شريطية

اعداد : أسماء الحروب

إشراف : الدكتور سلمان محمد سلمان

والدكتور ثوماس بروكل

الملخص

تم في هذا البحث دراسة موسعة لنظام تجمع جزيئات النانو بهياكل ثنائية وثلاثية الأبعاد أو مصفوفات شريطية. وقد استخدمت في هذا البحث جزيئات كروية من أكسيد الحديد المغناطيسية (Fe_2o_3) المصنعة من قبل Ocean Nanotech LLC بقطر يساوي 20 نانوميتر وذات شكل كروي مغموسة في المركب العضوي التولوين.

في البدء وضعت جزيئات أكسيد الحديد المغناطيسية على رقائق السيلكون بطريقتين : الأولى تدعى التلبيس المغزلي (Spin coating) بوضع جزيئات النانو على رقائق السيلكون ومن ثم وضع الرقائق على جهاز التلبيس المغزلي Spin–coater لفترة زمنية وبسرعة معينة لتوزيع جزيئات النانو على سطح الرقائق والحصول على طبقات أحادية أو متعددة. والطريقة الثانية تدعى التنقيط (Drop–casting) بوضع الجزيئات على سطح رقائق السيلكون وتركها تتوزع بالانتشار الطبيعي لفترة زمنية معينة.

وتمت دراسة رقائق السيلكون باستخدام مجهر المسح الإلكتروني وجهاز أنود الغاليوم منخفض الأشعة السينية (غالكسي) بقياس حجم وتوزيع جزيئات النانو من خلال حيود الأشعة السينية بزاوية صغيرة (SAXS) وباستخدام برنامج (SasView). وتم حساب حجم وتوزيع جزيئات النانو باستخدام برنامج (GIMP) والحصول على هياكل ثنائية الأبعاد.

ولمعرفة نظام توزيع جزيئات النانو على شكل مصفوفات طولية تم استخدام الأشعة السينية على رقائق السيلكون المنقوشة بزاوية صغيرةّ ~ 0.2° ولم يظهر ارتباط بين ترتيب الجزيئات النانوية مع التوزيع المصفوفي.

وفي البحث أيضا تم إنتاج رقائق أكسيد الألمنيوم المنقوشة (Sapphire) بالمعالجة الحرارية ودراسة تجمع جزيئات النانو للحديد ونظام توزيعها كشرائط طولية باستخدام نفس التقنيات في حالة رقائق السيلكون المنقوشة.

نوصي بدراسة نماذج أخرى شبيهة من خلال مشاركات بنفس المركز.